Extraction of Lagrangian Ground Displacements and Subsurface Seismic Stress Changes for Rational Earthquake Disaster Mitigation

[合理的な地震減災に向けての地盤のラグランジアン変位、および地盤内応力場変化の抽出]

by

Zaheer Abbas Kazmi

カズ゛ミ ザ゛ヒール アッパ゛ス

A dissertation Submitted for
the Partial Fulfillment of
Requirements for the Degree of Doctor of Engineering
at
Department of Civil Engineering
University of Tokyo

Tokyo, Japan

June, 2013

Abstract

Earthquakes are catastrophic events instigating a variety of devastations by the strong ground shaking and/or internal deformations of the earth's crust. Although they draw less immediate attention, ground deformations often induce more serious devastations and long lasting geotechnical problems. Estimation of damage caused by an earthquake and to have a deep insight into the source mechanism primarily demands for the strong ground motion records. However, seismic records are either missing or very sparsely available, especially in the developing and third world countries. Therefore an alternate and more practical approach to define mechanisms for different types of damages, induced by seismic events, is a pressing need of the society for effective rehabilitation works, disaster mitigation, land conservation and specifications/guidelines for new constructions.

With the development of the space geodesy technology such as Laser Imaging Detection and Ranging Technology (LIDAR) and Interferometric Synthetic Aperture Radar (InSAR), acquisition of images of landforms and the changes in elevation with high (sub-milliimeteric) precision has become possible. However, normal interferograms detect displacements only in the Eulerian description, in which the description of motion is made in terms of the spatial coordinates which does not follow the motion of soil particles. When InSAR images are taken from different satellite flight directions, the 3-D displacement field of the terrain can be determined but it can still not distinguish the shallower ground displacements from the deeper crustal deformations. A method has been proposed and refined to extract three dimensional Lagrangian ground displacements from the available set of pre- and post-seismic digital elevation models with the underlying assumption that tectonic displacements have a gentle spatial variability. The method is capable of mapping out shallower and localized ground displacements (landslides, manmade changes etc.) from the total ground displacements. Reliability and practicality of the numerical approach was evaluated by its implication to one of the very well recorded and documented seismic event, the Mid-Niigata Prefecture Earthquake. The outcomes were found very well consistent with the field measurements of benchmarks and triangulation points. Furthermore, the pattern of Lagrangian ground displacements is in strong agreement with earthquake induced devastations.

Following the theory of elastic dislocation, linear geodetic source inversion analysis is carried out, with the available Lagrangian ground displacements, to reveal the source

mechanism of the earthquake and spatial distribution of slips on fault rupture planes for Mid-Niigata Prefecture Earthquake and 2005 Kashmir Earthquake. Discontinuities across the rupture planes embedded in laterally homogeneous stratified half-space are extended to obtain internal deformability and seismic stresses/strains in the interior of earth's crust through forward modeling. The second principal invariant of deviatoric stress tensor, J_2, is considered as work-a-round indicator of the rock's vulnerability to failure in the absence of reliable rock failure criterion and spatial coverage of soil/rock properties. Various tunneled sections for Joetsu line of Japan bullet train network (called Joetsu Shinkansen) passing through the epicentral area of Mid-Niigata Prefecture Earthquake were seriously damaged. Both the first invariant of Cauchy stress tensor, I_1, and the second principal invariant of the stress deviator tensor, J_2, are calculated at a regular interval along the longitudinal axes of selected tunnels such that the examined points would also include the damaged sections. Remarkably, all the damaged tunnel sections were found against the peak values of $\sqrt{J_2}$. A yield surface is defined as the boundary between clusters of points for damaged and undamaged tunnel sections in the scatter diagram of I_1 and $\sqrt{J_2}$.

Thousands of landslides were triggered both by Mid-Niigata and Kashmir Earthquakes. All the triggered landslides by both of the aforementioned earthquakes are found concentrated within the area of large seismic stresses/deformability. Furthermore, the landslides which existed before Mid-Niigata Prefecture Earthquake have also shown a strong concordant behavior with the co-seismic stresses which suggests that a similar stress pattern might have been repeating in the past. Therefore, the obtained yield surface can be used to examine the margin of safety of both existing and new tunnels for a given scenario earthquake in the target region as well as for delineating potentially hazardous area for landslides.

List of Publications

a) Peer-reviewed Journal/Book Chapters

1. **Z. A. Kazmi**, K. Konagai, H. Sekiguchi and T. Fujita (2013); "Extracting Earthquake Induced Lagrangian Ground Displacements and their Implication for Source Inversion Analysis"; *Soil Dynamics and Earthquake Engineering.* Vol. 48, pp. 98-108

2. **Z. A. Kazmi**, K. Konagai, H. Kyokawa and C. Tetik (2012); "Surface Rupture of the Normal Seismic Faults and Slope Failures appeared in April 11th, 2011 Fukushima Prefecture Hamadoori Earthquake"; *JSCE Journal of Earthquake Engineering,* Vol. 68 No. 4, pp. I_1285 – I_1292**.**

3. K. Konagai, **Z. A. Kazmi** and Yu Zhao (2012), Extracting Earthquake Induced Coherent Soil Mass Movements. *Chapter 14, Earthquake Research and Analysis-New Frontiers in Seismology,* ISBN 978-953-307-840-3, InTech, DOI: 10.5772/30822.

4. Kiyota T, Konagai K, Sattar A, **Kazmi Z.A.**, Okuno D, Ikeda T (2011); "Breaching failure of a huge landslide dam formed by 2005 Kashmir Earthquake"; *Soils and Foundations* Vol. 51 No. 6 pp. 1181-1192.

5. **Z. A. Kazmi**, K. Konagai and T. Ikeda (2013); "Field Measurements and Numerical Simulation of Debris Flows from Dolomite Slops Destabilized during the 2005 Kashmir Earthquake, Pakistan"; *Journal of Earthquake Engineering,* (Under Review)

6. K. Konagai and **Z. A. Kazmi** (2013); "Co-seismic stress changes and damage to tunnels in the October 23, 2004 Mid-Niigata-Prefecture Earthquake"; *Soil Dynamics and Earthquake Engineering*, (Under Review)

b) International Conferences and Symposia

1. **Z. A. Kazmi** and K. Konagai (2013); "Contribution of Internal Deformations of Earth's Crust in Triggering Earthquake Induced Disasters"; *Bulletin of Earthquake Resistant Structure Research Center*, No. 46, pp. 43-52

2. **Z. A. Kazmi**, M. Irfan and T. Ahmed (2013): "Seismic vulnerability evaluation of non-engineered structures in Pakistan --A statistical approach based on cumulative opinion of professionals--", *Proceedings, 10th International Conference on Urban Earthquake Engineering, 1-2 March 2013, Tokyo, Japan.* pp. 1795-1801

3. **Z. A. Kazmi**, and K. Konagai (2012): "Surface Tectonic Displacement and Slip Distribution of 2004 Mid-Niigata Prefecture Earthquake"; *Proceedings of JAEE First International Symposium on Earthquake Engineering, Tokyo, Japan.*, pp. 11-20

4. **Z. A. Kazmi**, and K. Konagai (2012): "Three Dimensional Co-seismic Surface

Tectonic Displacement of 2004 Mid-Niigata Prefecture"; *Proceedings of the 32nd Conference on Earthquake Engineering, JSCE, 2012, Tokyo, Japan.* Paper No. 01-255

5. **Z. A. Kazmi**, K. Konagai and T. Ikeda (2012): "Physical and Numerical Study of Debris Flow from Dolomite Slopes Exposed in 2005 Kashmir Earthquake, Pakistan"; *Proceedings of the 15th World Conference on Earthquake Engineering, Lisbon, Portugal.*

6. **Z. A. Kazmi**, K. Konagai, C. Tetik, J. Bray and A. Streig (2012): "Fault rupture and associated Geo-hazards of Fukushima-Prefecture Hamadoori Earthquake"; *Proceedings of the International Symposium on Engineering Lessons Learned from the 2011 Great East Japan Earthquake, Tokyo, Japan.* pp. 289-296

7. H. Kyokawa, K. Konagai, T. Kiyota and **Z. A. Kazmi** (2012): "LiDAR Measurement of the Breached Earth-fill Dam in the March 11th Great East Japan Earthquake"; *Proceedings of the International Symposium on Engineering Lessons Learned from the 2011 Great East Japan Earthquake, Tokyo, Japan.* pp. 973-980

8. **Z. A. Kazmi**, K. Konagai and T. Ikeda (2012): "Physical and Numerical Study of Debris Flow from Dolomite Slopes Exposed in 2005 Kashmir Earthquake, Pakistan"; *Proceedings of the 15th World Conference on Earthquake Engineering, Lisbon, Portugal*.

9. **Z. A. Kazmi**, T. Ahmed, U. Saleem and M. Irfan (2012): "Evaluation of design and construction practices – A lesson learnt from Kashmir Earthquake"; *Proceedings of the International Symposium on Engineering Lessons Learned from the 2011 Great East Japan Earthquake, Tokyo, Japan*. pp. 1846-1857

10. **Z. A. Kazmi**, K. Konagai, T. Ikeda and A. Sattar (2010): "Calibrating Debris Flow Numerical Simulation Parameters for Proper Disaster Mitigation Strategy -Case Study of Debris Flow in Muzaffarabad-"; *Proceedings of the 13th Japan Earthquake Engineering Symposium."* pp. 2072, 2079.

Table of Contents

Acknowledgement

At first I would like to express my sincere gratitude to Professor Kazuo Konagai for the honor of accepting me to his research group first as a Master's student and then as doctoral student at the department of civil engineering of the University of Tokyo. By giving me this chance, my skills in both the field, through many reconnaissance trips in Japan and Pakistan, and in research, were developed effectively. As an advisor he always provided me with his precious time for fruitful discussions on many topics concerning my research and through his advising I acquired invaluable knowledge on the highly developed field of earthquake engineering in Japan.

I am also grateful to Associate Professor Takashi Kiyota firstly as committee member and then as advisor during the last six months of my doctoral studies, after retirement of Professor Konagai. He has also devoted his time for my understanding and polishing my abilities. I am obliged to all my other committee members, Profesor Junichi Koseiki, Associate Professor Wataru Takeuchi, Professor Haruko Sekiguch, for very enlightening discussion and bunch of important advices on the procedure, outputs and practical implications of my research. Their questions and suggestions have opened new ways for my future research endeavors.

I am indebted to Ms. Tomomi Sannomiya, Ms. Hiroko Takasaki, Mr. Toshihiko Katagiri and my tutor, Mr. Takeshi Arita, for taking care of so many administrative issues and helping with many Japanese documents to make my life easier in Japan.

I am also grateful to the personnel of the civil engineering administrative office as well as the Civil Engineering Department's Foreign Students Officers who always helped cheerfully for administrative as well as daily life matters.

I would like to thank all former and current members of our laboratory Dr. Ahsan, Mr. Asakura, Ms. Roxanne, Mr. Han, Mr. Yokoyama, Mr. Go, Mr. Mera and all others for their everyday interaction, friendly discussions, opinion exchanging and ideas sharing. Their presence in the form of good friends around me made my life easier even in the situations of heavy work load.

Of course, nothing of the aforementioned would have happened if it hadn't been for the financial support from the Japanese Government (MEXT). For that I am deeply grateful.

Last but not least, my mother and all other family members in Pakistan who have always been there for me and supporting me in every way so that I could be comfortable away from them. Good and sincere wishes of my father who is no more in this world have never let me down at any stage. My gratitude to you cannot be expressed in words.

I am also thankful to my wife who has always been so patient to hear difficulties in my research and supported me in every way to accomplish the goals of this thesis. I would also like to thank my three weeks old son for bring happiness to me at the time when I had nothing else but work load.

Chapter 1

1 Introduction

1.1   RESEARCH MOTIVATION

The earth is a dynamic structure giving rise to various internal and external seismic events, which create a variety of hazards in the built environment. During an earthquake, stresses in the interior of the earth adjacent to the activated fault are redistributed leading to permanent deformation. We can't deny from the fact that crustal deformations and shallow coherent and discrete mass movements are equally or often more devastating than intense ground shaking. Large strains built up in soils and rocks along a dislocated fault can trigger post-earthquake disasters such as landslides and debris flows, which can last long causing serious problems for rehabilitations and land conservations. Geomorphological changes during an earthquake can be measured by comparing pre- and post-seismic geodetic observations.

With the development of the space geodesy technology such as Laser Imaging Detection and Ranging Technology (LIDAR) and Interferometric Synthetic Aperture Radar (InSAR), acquisition of images of landforms and the changes in elevation with high sub-milliimetric precision has become possible. However the methods allow us to detect displacements only in the Eulerian description, in which the description of motion is made in terms of the spatial coordinates which does not follow the motion of soil particles. When InSAR images are taken from different satellite flight directions, the 3-D displacement field of the terrain can be determined but it can still not distinguish the shallower ground displacements from the deeper crustal deformations. All it demands us to rationally understand and monitor terrain dynamics without limitations of data availability and to extract more precisely shallower soil mass movements.

Estimation of damage caused by an earthquake primarily demands strong ground motion records. Although there has been a significant development to record strong ground motions in the last few decades, seismograms have been often missing or very sparsely available, especially in developing countries. With a very few exception, Figure 1.1 depicts a very clear correlation between the distribution of seismic stations and nominal per capita GDP across the world, highlighting that a larger part of the world still has either no seismic

stations or very sparsely distributed. Sometimes due to the state security or other unknown policies, even the recorded waveform records are not disclosed to scientific society, creating impediment to access fine-tuned source mechanism, its temporal and spatial extent and consequently the rehabilitation and land conservation works. Two most recent examples of both of the above mentioned cases could be the 2005 Kashmir Earthquake and 2008 Wenchuan Earthquake of China, respectively. For the 2005 Kashmir Earthquake, only two or three waveform records were available at a very far distance from the source region; while for the 2008 Wenchuan Earthquake, there were many recorded waveform but not disclosed for at least first one year.
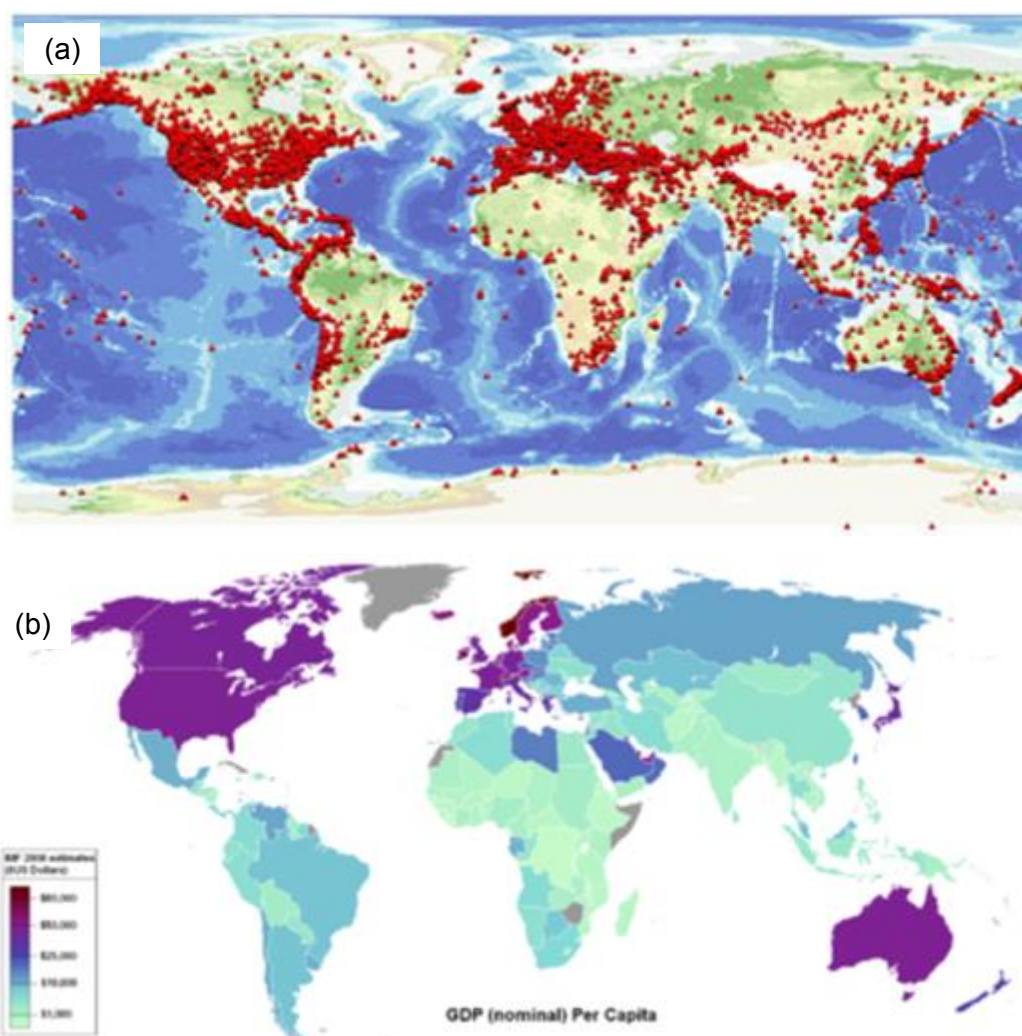

Figure 1.1: (a) World map of seismic stations (Bathymetry and topography: US Department of Commerce, National Oceanic and Atmospheric Administration, National Geophysical Data Center, 2006. 2-minute Gridded Global Relief Data) and (b) GDP nominal per capita world map (International Monetary Fund (IMF) figures for year 2006)

Inversion of recorded seismograms to obtain fault mechanism and spatial and temporal rupture history of an earthquake is a common approach and imperative need of seismology. In the unavailability of the seismogram records, geodetic data inversion sought to be of wider application. Although inversion of static ground surface displacements is as old as the introduction of elastic dislocation theory in seismology, presence of very precise and high resolution ground displacement data around the source region, with shallower soil movements filtered out, more refined and precise fault slip distribution can be made evident.

Most of the moderate to large historical earthquakes are accompanied by numerous landslides disasters and damage to surface and underground infrastructure facilities and life lines (e.g. damage to deeply buried railway and road tunnels, gas and water supply lines, drainage wells, surface communication links etc.). Detailed knowledge of their damage mechanisms is the fundamental requirement for developing rational strategies and design and construction specifications for rehabilitation/reconstruction of the existing facilities and for new construction. The fine picture of the earthquake source mechanism, even in the absence of waveform record, is used as input to get deformations and seismic stresses in the interior of earth which can help to reach root causes of such devastations.

1.2   PROBLEM OVERVIEW

2004 Mid-Niigata Prefecture Earthquake of magnitude 6.8 jolted central Japan on October 23, 2004. Hitting one of seismically most active country equipped with many advanced instruments and technology to record the data, Mid-Niigata Prefecture Earthquake proved to be one of the very well recorded and documented seismic events in the history. The earthquake reportedly triggered and/or reactivated thousands of landslides and the total economic loss due to their direct and indirect impact was estimated at 8 billion US dollars. In addition to the direct impacts of the landslides, alike our observation in historical earthquakes hitting active folding regions, an intensification of the mass movement phenomena (progressive and continual movement of the disturbed soil masses) was observed during the snow melting and rainy seasons. A similar extent and behavior of earthquake induced landslides was observed during the 2005 Kashmir Earthquake.

Another most serious devastation during the Mid-Niigata Prefecture Earthquake was damage to underground infrastructure facilities, especially railway tunnels. Damage to deep tunnels for Juetsu line for Japan bullet train (Shinkansen) has clouded the notion that tunnels embedded in deeper strata are much safer during serious shakings. To carry out rehabilitation work and to avoid such devastation or at least to minimize their effect on the

society and resulting losses, knowledge of the failure mechanisms and their controlling parameters is essential. Different researchers adopted different approaches for understanding these devastations but were scarce at one stage or other. To thoroughly understand the damage mechanism of afore mentioned devastations, especially for the earthquakes with no sophisticated seismograph records to estimate earthquake induced damages, a comprehensive knowledge of the terrain dynamics, earthquake source mechanism and internal deformability of earth's crust is prerequisite.

1.3   RESEARCH OBJECTIVES AND METHODOLOGY

Although many attempts have been made to retrieve co- and post-seismic crustal deformations in a fast, frequent and precise way, all approaches were limited in either tracing history dependent movement of soil particles or in distinguishing deeper or shallower ground displacements. An improvement is made to an existing model to more realistically extract Lagrangian ground displacements and to filter out shallower soil movements from total crustal deformations. The method is capable of tracing out landslides and other manmade changes.

Based on theory of elastic dislocation, approaches to obtain earthquake source mechanism from the pre-calculated surface components of deeper parts of crustal deformations and to obtain internal deformability of laterally homogeneous layered earth structure have been developed and evaluated for Mid-Niigata Prefecture Earthquake and 2005 Kashmir Earthquake. A correlation is developed between earthquake induced devastations and internal deformability of the earth's crust through detailed study.

1.4   ORGANIZATION OF THESIS

Chapter 2 describes the detailed overview, including geological and geomorphological settings, of the seismic events and areas selected for this study. Devastations in the study areas from the literature and field measurements/observations are highlighted in detail. Chapter 3 represents an improved method to extract Lagrangian ground displacements from available pre- and post-seismic digital elevation models. The method is also capable of filtering out landslides, manmade changes and other shallower soil mass movements. The application of the proposed method to the study areas and verification of the numerical outcomes with the field measurements and/or observations are also presented in Chapter 3 to develop a cause and effect relation.

Chapter 4 presents the methodology based on elastic dislocation theory for geodetic source

inversion analysis with the available fine resolution ground displacement data, presented in Chapter 3, as input. Application of this method to retrieve spatial distribution of slips on adopted fault models for both the selected earthquake (study areas) is also presented in Chapter 4.

Through forward modeling in elastic half space and available seismic moment across the fault rupture planes, an approach to obtain deformability and seismic stresses in the interior of earth's crust is described in Chapter 5. This chapter also presents application of this method to both the study areas and a detailed discussion and comparison of the internal deformability of the earth's crust to earthquake induced devastations.

Chapter 6 concludes and highlights the most important aspects of this study along with its practical applications for disaster management. This chapter also mentions possible future extensions of the presented study.

Chapter 2

2 Overview of Study Areas

For the subject study, the areas affected by two of the most catastrophic earthquakes of last decade, namely Mid-Niigata Prefecture Earthquake, 2004 (Japan) and Kashmir Earthquake, 2005 (Pakistan), are selected. The detailed features of both of these earthquakes are discussed in the following sections. For Mid-Niigata Prefecture Earthquake, JGD2000/ Japan Plane Rectangular Coordinate System is used. In this coordinate system, Japan is divided into 19 zones assigned with Greek numerals from I to XIX with the exception of isolated islands. The targeted study area lies in Zone VIII with its southwest corner located at 138°30'00"E, 36°00'00"N. For 2005 Kashmir Earthquake, Geographical Latitude and Longitude (WGS84) is used.

2.1   MID-NIIGATA PREFECTURE EARTHQUAKE

2.1.1   Introduction

The main shock of Mid-Niigata Prefecture Earthquake of magnitude 6.8 jolted central Japan at 17:56 JST (08:56 GMT) on October 23rd, 2004. The hypocenter of the main shock was located at 37.29°N, 138.87°E in Mid-Niigata Prefecture at a depth of 13 km. The maximum acceleration of 1500 cm/s^2 was recorded at Ojiya K-net station which is about 10km west of the epicenter (National Institute of Earth Science and Disaster Prevention, 2004). The Japan Meteorological Agency (JMA) has named it the "Heisei 16 Niigata Prefecture Chuetsu Earthquake" or "The Mid-Niigata Prefecture Earthquake of 2004".

The main earthquake was followed by a series of strong aftershocks in rapid succession with four of magnitude 6 or larger (Figure 2.1 and Table 2.1). These strong earthquakes had focal mechanisms of reverse fault type (shown as projections on the lower focal hemisphere in Figure 2.1) with the compression axes oriented WNW/ESE, consistent with the historical information of large earthquakes in this area. The epicenters of the aftershocks were distributed along the NNE and SSW direction within a length of about 30km immediately beneath the Higashiyama mountains zone (Honda et al., 2004). This continual tectonic movement has formed NNE-SSW trending geological folds of sedimentary rocks in the source region.

Table 2.1: Summary of the main shock and aftershocks of magnitude larger than 6. All these events are marked with numerals in Figure 2.1 and their focal mechanisms are also shown.

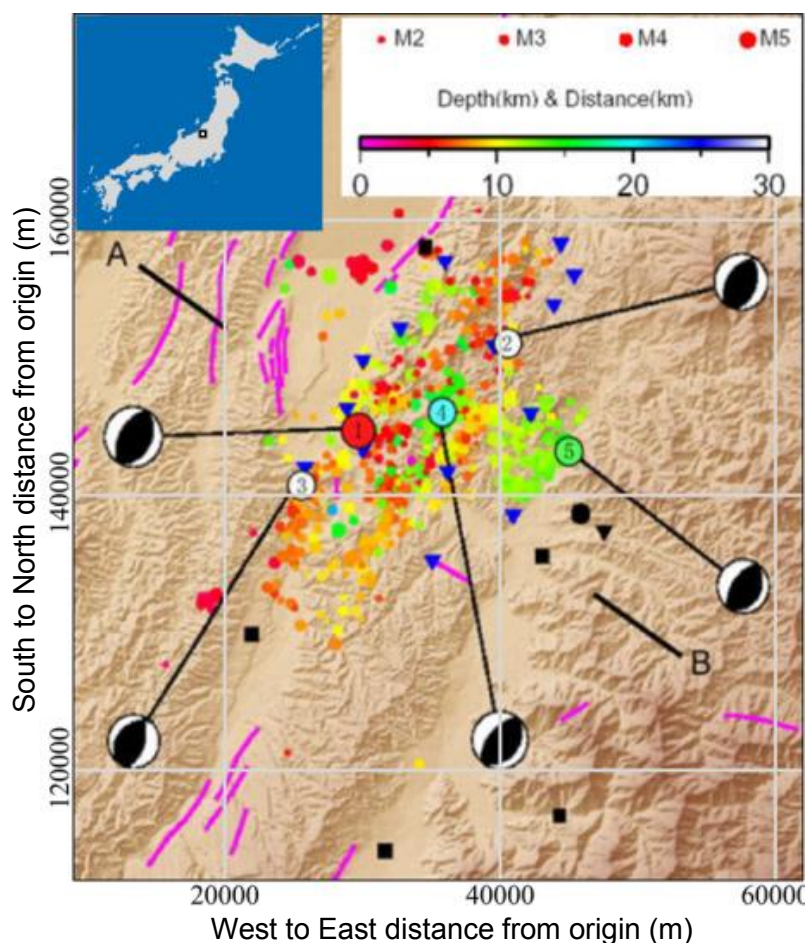| Date	Time	Magnitude	Depth (Km)	Category
October 23	17:56	6.8	13	Main shock
	18:03	6.3	9	Aftershock
	18:11	6.0	12	Aftershock
	18:34	6.5	14	Aftershock
October 27	10:40	6.1	12	Aftershock

Figure 2.1: Epicenteral distribution determined from the present aftershock observation [18:00 JST Oct. 24 to 20:00 JST Oct. 27, 2004; data from Sakai et al. (*2005*)]. Aftershocks are denoted by color according to depth. There are 625 aftershocks plotted, among which the main shock and large aftershocks are denoted by circles with numerals: 1. M6.8 mainshock (17:56 Oct. 23), 2. M6.3 aftershock (18: 03 Oct. 23), 3. M6.0 aftershock (18:11 Oct. 23), 4. M6.5 aftershock (18:34 Oct. 23), 5. M6.1 aftershock (10:40 Oct. 27). Focal mechanisms are shown as projections on the lower focal hemisphere, where shaded areas indicate tension and white areas indicate compression. Active faults are denoted by solid pink lines (Hirata et al., 2005). Topographical mapping is on the JGD2000/ Japan Plane Rectangular Coordinate System VIII with its southwest corner located as the origin at 138°30'00"E, 36°00'00"N.

2.1.2 Geological and Geographical Settings

The epicentral area is located in the Higashiyama Hills and its neighboring alluvial plain, where the Shinano River flows from SW to NE then turns to NW to N after merging with the Uono River (Figure 2.2). The area is one of the most active tectonic regions, in which a fold-and-thrust belt is well developed (Yoong and Okada, 2005).
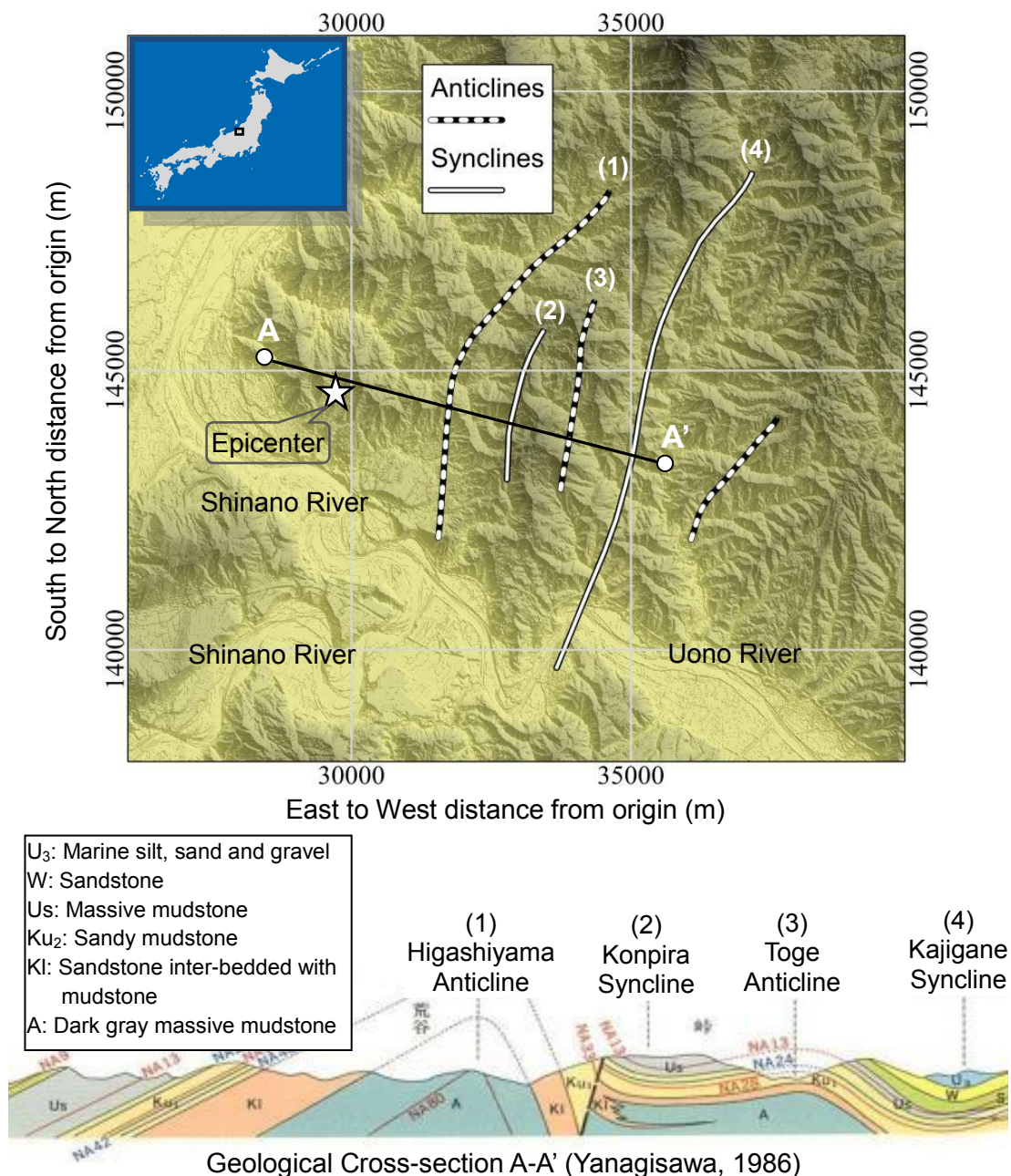

Geological Cross-section A-A' (Yanagisawa, 1986)

Figure 2.2: Terrain map for the epicentral area of Mid-Niigata Prefecture Earthquake along with detailed geological cross-section to show subsurface geological formation and details of folded structure. Topographical mapping is on the JGD2000/ Japan Plane Rectangular Coordinate System VIII with its southwest corner located as the origin at 138°30'00"E, 36°00'00"N.

Geological studies [Okamura et al., 1995; Ikeda et al., 2002; Sato et al., 2004] suggest that thick sediments accumulated in a rift system which formed in an extensional stress regime during back-arc spreading. Due to this tectonic and geologic background, many landslides have been occurring in this area and they characterize the geomorphic features.

The geological outline is summarized as follows from Yanagisawa et al. (1986) and Kobayashi et al. (1991). The Higashiyama Hills are underlain by Miocene to Pleistocene strata, which trend NNE-SSW with several anticlines and synclines (Figure 2.2). Where the fold axes plunge, the trend of the strata changes to E-W locally. The axes are named the Higashiyama anticline, Konpira syncline, Toge anticline, Kajikane syncline, and Komatsugura anticline from the west to the east with a half wavelength of about 1 -1.5 km (Figure 2.2). The strata consist mainly of mudstone, alternating beds of siltstone and sandstone, and sandstone with subordinate dacitic or andesitic volcanic rocks.

2.1.3   Devastations in Historical Earthquakes Hitting Active Folding Region

Taking a look at history, it is found that earthquakes in active folding areas have distinctive features and can trigger long lasting geotechnical issues. In an active folding zone, the action of deep-seated forces has been shortening sedimentary rock layers causing folded geomorphic surfaces to appear and develop. Looking at a fold surface in profile (Figure 2.3) upslope and downslope flanks of the fold join together at anticlines and synclines, respectively. Since the up-folded rocks along anticlines have been expanded and cracked over centuries, anticlines frequently have their crests deeply eroded, with a number of debris deposits rimming the eroded hollows. Large-scale landslides are found even on gentle mountain sides dipping towards synclines because their toes are often deeply eroded by rivers. The active folding regions can be thus one of the most landslide-prone zones. In active-folding areas, thick neritic sediments are found widely distributed and focal mechanisms are often complex in such a way that hypocenters of aftershocks scatter remarkably. Moreover, it is often difficult to identify if a particular destruction was caused by the main shock or one of its aftershocks.

2.1.3.1 Zenkoji Earthquake, 1847

The May 8th, 1847 Zenkoji Earthquake (M=7.4) jolted the active folding mountain terrain west of Nagano, central Japan. Devastations were serious along the entire 50km stretch of the Nagano western basin-edge fault that appeared along the skirts of the active folding mountains (Figure 2.4).
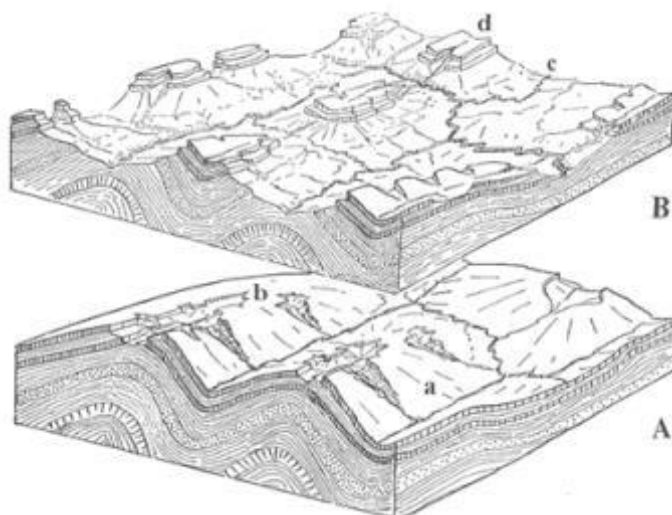
Figure 2.3: Erosion of geological fold (Original figure from de Martonne, 1927). Erosion develops from A to B in such a way that syncline valley (a) and anticline ridge (b) in A to become anticline valley (d) and syncline ridge (c) in B, respectively.
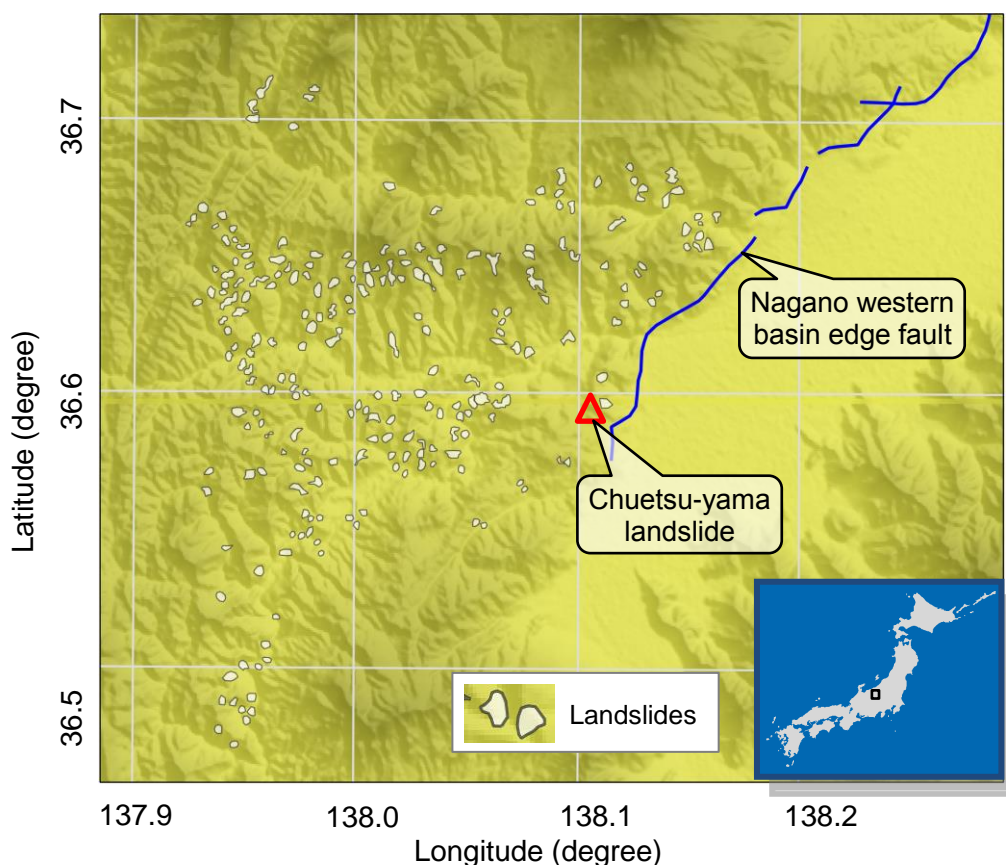

Figure 2.4: Landslides caused by the Zenjkoji Earthquake of 1847: The Nagano western basin edge fault is considered to have been responsible for the earthquake. Earthquake-induced landslides distribution is taken from Fig. 1-12 (by Akabane), the Report of Zenkoji Earthquake, Central Disaster Prevention Council (2008). A crack near the southern summit of the Chausu-yama twin peaks (Elevation 730m, Location: 37.294694°N, 138.875492°E, triangle mark) began to open wide, which was an early sign of a long-lasting landslide.

The earthquake caused about 44,000 landslides to occur on the hanging wall side of the fault. In 1884, 37 years after the earthquake, a big crack appeared near the southern summit of the Chausu-yama twin peaks and an 800m long soil mass started moving. After the heavy rains of 1930, the entire soil mass began to creep down the slope exhibiting thick, wet and sticky features, and the maximum speed of 93 m/year was reached in 1932-1934. The slope was finally stabilized in the 1970s with a tremendous amount of drainage works that were started in 1965 (Kato H. and Akabane H., 1986).

2.1.3.2 Senboku Earthquake, 1914

A M7.1 earthquake jolted a low-rising mountain terrain of Senboku, Akita, Japan on March 15th, 1914. Though the intensities registered at major cities were not surprisingly large, the reported deaths of 84 among the total 94 were concentrated locally within the 10km x 10km active folded Senboku area. Landslides in Senboku area that appeared in the report of Imperial Earthquake Investigation Committee, No. 82 (1915) and those from the Mid-Niigata Prefecture Earthquake of 2004, which will be explained later, are exactly alike in that just surface laminar sedimentary rocks were detached and slipped down the planar layer boundaries as shown in Figure 2.5.
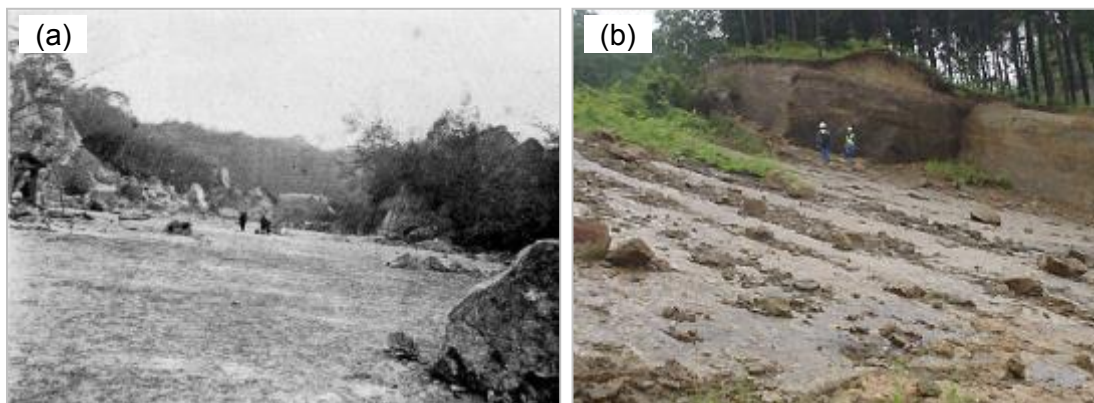

Figure 2.5: Similarities between Landslides in the March 15th, 1914 Senboku Earthquake and the October 23rd 2004 Mid-Niigata Prefecture Earthquake (a) Nunomata Landslide in Senboku Earthquake (b) Uragara landslide in Mid-Niigata Prefecture Earthquake.

2.1.4   Devastations in Mid-Niigata Prefecture Earthquake

2.1.4.1 Landslides and Landform Changes

Generally, landslides triggered by earthquake are one of the most damaging natural disasters. Damages caused by earthquake-triggered landslides can be often worse than those directly caused by intense shakes. Kobayashi (1981) found that more than half of all deaths in large earthquakes (M > 6.9) in Japan between 1964 and 1980 were caused by

landslides.

Mid-Niigata Prefecture Earthquake reportedly triggered and/or reactivated thousands of landslides, including 362 landslides with widths of more than 50 m and 12 large-scale landslides with individual volumes of more than 1 million cubic meters (Ministry of Land, Infrastructure and Transport, 2005). The economic loss due to these landslides was initially estimated at 8 billion US dollars, making this one of the costliest landslide events in history (Kieffer et al., 2006). Several mountain hamlets have been rendered uninhabitable for the foreseeable future. Forty five landslide dams were formed by this earthquake, flooding residential houses as well as rice fields. Among those, the Higashi Takezawa landslide dam and the Terano landslide dam were most catastrophic and demanded urgent countermeasures to control water level and prevent downstream villages from possible breaching. National Institution of Earth Science and Disaster Prevention (NIED) prepared a landslide-distribution map from a 1/6000 scale aerials photos through air-photograph interpretation (Oyagi et al. 2008) (Figure 2.6).
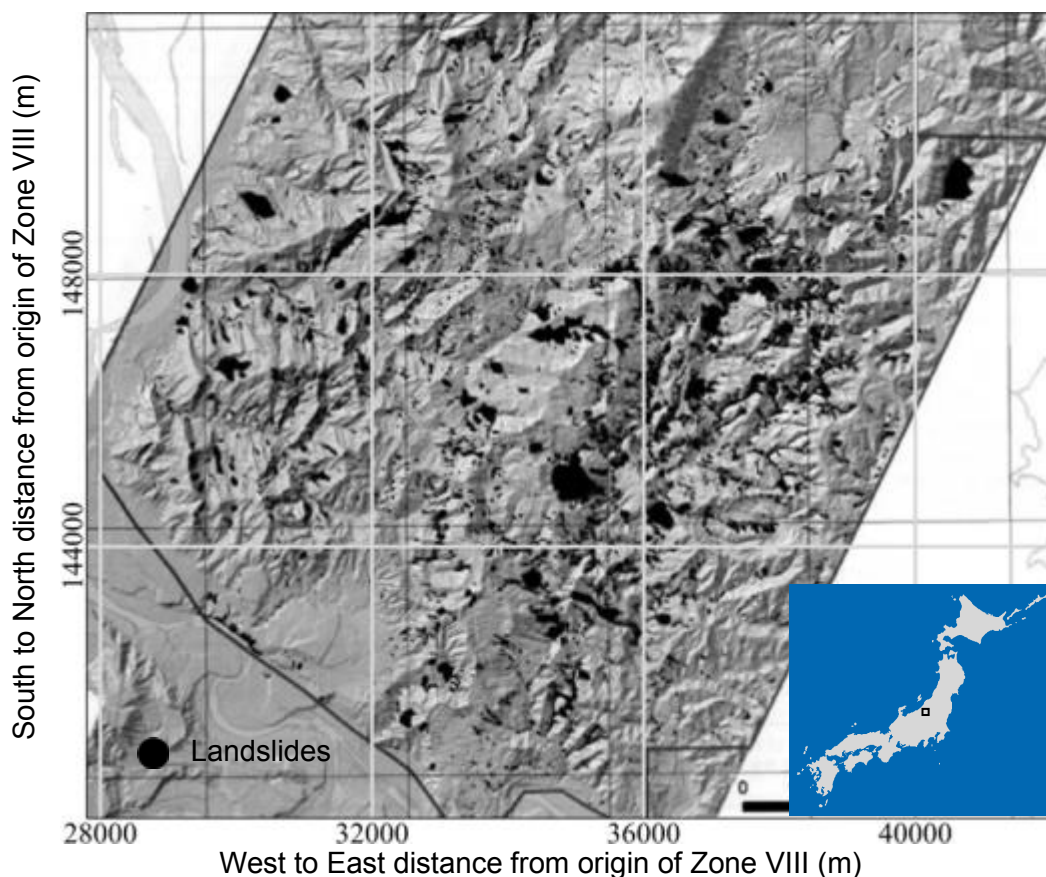

Figure 2.6: Distribution map of the landslides triggered by the Mid-Niigata Prefecture Earthquake (Oyagi, 2008). Topographical mapping is on the JGD2000/ Japan Plane Rectangular Coordinate System VIII with its southwest corner located as the origin at 138°30'00"E, 36°00'00"N.

In case of Mid-Niigata Prefecture earthquake, not only landslides but also surface tectonic displacements have caused some problems for rehabilitating the affected areas. As will be discussed in chapter 3, the tectonic movements have caused the middle part of both the Shinano and Uono Rives to be raised upward by about 0.5 to 1.0 meters. Probably due to this tectonic deformation, the upper stream reach of the Uono River was flooded in the heavy rain of June, 2005, about eight months after the earthquake.

2.1.4.2 Damage to Underground Facilities

Mountain tunnels, being underground structures and situated deep within rock layers, are generally considered to suffer appreciably less damage from earthquakes than surface structures (Okamoto 1973; Sharma and Judd 1991; Hashash et al. 2001); however, when a tunnel is located in a continuously compressed active folded region and experiences extremely strong earthquake shaking, it may still possibly be damaged.

Fifty (50) out of the total 138 tunnels (including normal railway tunnels, road tunnels, Shinkansen (bullet train) tunnels and water conveyance tunnels for hydroelectric power projects), that existed in the damaged region of 2004 Mid-Niigata Prefecture Earthquake, suffered various degrees of damage (Tunnel Engineering Committee, JSCE 2005). Most common damage patterns included

(1) Cracking in the tunnel lining parallel or slanted to the tunnel axis

(2) Compressive failure at the tunnel crown and spalling of concrete lining

(3) Upheaval of side wall concrete and cracks in invert concrete

Jiang et al. (2010) has comprehensively summarized the literature, construction details and performance of all the tunnels damaged by Mid-Niigata Prefecture Earthquake (Figure 2.7 and Table 2.2)

Among all other trunk lines, Juetsu Shinkansen line was most important and deeply embedded in the deep stable strata. Damages to Horinouchi, Uonuma, Myoken and Takiya tunnels of Juetsu Shinkansen line of Japan bullet train network (tunnel number 22-25 in table 2.2 and Figure 2.7), embedded in the deep soil strata with an average overburden thickness of more than 70 meters, have highlighted that the damages were not the results of localized shallow landslides. Detailed discussion on damage patterns and failure mechanisms of Juetsu Shinkansen tunnels is presented in Chapter 5

Table 2.2: The damages to tunnels in 2004 Mid-Niigata Prefecture Earthquake (Jiang et al., 2010)

No	Tunnel Name	Usage	Tunneling Method	Completion Time	Lining (cm)	Length (m)	Max. Overburden (m)	Width (m)	Height (m)	Damage Degree	Damage Description
1	Wanantu	Road	CTM	1963	C(50)	300	40	8.2	4.6	A1	Spalling in arch, spalling crack, and deformation in side wall
2	Kosendani2	Road	CTM	1983	C(60)	1088	62	9.5	4.8	A2	Crack, spalling in arch and sidewall
3	Yamamotoyama	Road	CTM	1981	C(60)	1839	140	10.2	7.5	B	Crack
4	Yamanaka	Road	CTM	1972	C(60-75)	1307	200	6.5	4.5	B	Longitudinal crack
5	Takeisi	Road	CTM	1986	C(50-60)	331	140	7.0	7.74	B	Longitudinal crack
6	Higasiyama	Road	CTM	1987	C	220	35	7.0	4.7	B	Crack in arch
7	Takezawa	Road	CTM	1965	C	18.2	6	6.0	4.5	A2	Crack in arch, side and bed
8	Siroyama	Road	CTM	1997	C	128	150	7.0	4.7	B	Longitudinal crack in side wall
9	Orinaka	Road	CTM	1994	C	374	60	9.25	4.7	B	Crack in arch and sidewall
10	Obirou	Road	CTM	1991	C	390	90	9.25	4.7	B	Crack
11	Sibumi	Road	CTM	1995	C	860	150	6.0	4.7	B	Spalling in arch
12	Haneguro (Roadway)	Road	CTM	1967	C(50)	506	100	5.6	5.2	A1	Compressive buckling in bed, crack in arch and sidewall
13	Haneguro (Pavement	Road	NATM	1994	C(30)	550	100	2.2	2.85	A2	Spalling
14	Junidaira	Road	CTM	1987	C(50-80)	210	40	8.5	4.7	A1	Spalling, deformation in sidewall
15	Rangi	Road	CTM	1989	C(60)	590	180	6.0	4.7	A2	Longitudinal crack in arch,

No	Tunnel Name	Usage	Tunneling Method	Completion Time	Lining (cm)	Length (m)	Max. Overburden (m)	Width (m)	Height (m)	Damage Degree	Damage Description
											upheave in bed
16	Siotani	Road	CTM	1983	C(50-60)	512.2	110	7.5	5.85	A2	Crack in arch
17	Kizawa	Road	NATM	1991	C(30-70)	305	30	6.0	4.7	A1	Deformation, spalling, opening in roadbed
18	Araya	Road	CTM	1977	C(60)	292	45	7.5	5.64	A1	Compressive buckling, crack, opening in bed
19	Tochio	Road	NATM	2001	C(30-50)	854	150	1035	4.7	B	Water leakage from juncture
20	Okimitouge	Road	NATM	2000	C	1080	150	8.5	4.7	B	Longitudinal crack in sidewall
21	Hosa	Shinkansen	CTM	1979	C(70-90)	6087	15	9.6	8.3	B	Crack in roadbed
22	Horinouchi	Shinkansen	CTM	1978	C(70-90)	3300	100	9.6	8.3	A2	Spalling in sidewall
23	Uonuma	Shinkansen	CTM	1977	C(70-90)	8624	70	9.6	8.3	A1	Spalling, upheave in bed, crack
24	Myoken	Shinkansen	CTM	1976	C(70-90)	1459	65	9.6	8.3	A1	Crack, upheave in roadbed
25	Takitani	Shinkansen	CTM	1977	C(70-90)	2673	55	9.6	8.3	A2	Crack
26	Sinfukuyama	Railway	CTM	1963	C(45)	1468	75	4.8	5.0	A2	Crack
27	Fukuyama	Railway	CTM	1923	CB(39)	1350	7	4.8	5.6	B	Crack
28	Wanantu	Railway	CTM	1965	C(50)	725	41	8.5	7.5	A1	Spalling, crack, failure in the juncture of arch and sidewall
29	Nakayama	Railway	CTM	1966	C(50)	1205	92	8.5	7.5	B	Crack
30	Usigazima	Railway	CTM	1966	C(50)	432	14	8.5	7.5	A2	Crack in portal
31	Tenou	Railway	CTM	1966	C(45-60)	285	11	4.7	5.1	A1	Crack
32	Sintouge	Railway	CTM	1967	C(35-50)	1372	75	4.7	5.1	A1	Crack
33	Touge	Railway	CTM	1921	CB(23-46)	641	70	4.8	5.1	A2	Crack

No	Tunnel Name	Usage	Tunneling Method	Completion Time	Lining (cm)	Length (m)	Max. Overburden (m)	Width (m)	Height (m)	Damage Degree	Damage Description
34	Hanada	Railway	CTM	1967	C(60)	880	28	8.6	6.3	B	Spalling
35	Tukayama	Railway	CTM	1966	C(50-60)	1766	150	8.7	6.3	A2	Crack
36	Higasiyama	Railway	CTM	1968	C(60)	166	22	8.8	6.4	B	Spalling
37	Iwayama	Railway	CTM	1927	CB(39-46)	652	54	4.7	5.2	B	Spalling
38	Iwazawa	Railway	CTM	1927	CB(39–47)	203	36	4.6	5.1	B	Spalling
39	Myoukouzan	Railway	CTM	1927	CB(23–91)	1465	151	4.6	5.2	A2	Crack
40	Kouyouzan	Railway	CTM	1970	C(45–60)	500	67	4.8	5.1	A2	Crack
41	Utigamaki	Railway	CTM	1927	CB(47–87)	425	30	4.6	5.2	A2	Crack
42	Akakura	Railway	CTM	1974	C(45–70)	10471	440	4.3-8.5	6.2-6.9	B	Spalling, crack in arch and sidewall, water leakage
43	Jusanmachi	Railway	CTM	1975	RC(55)	1695	40	5.05	5.68	B	Water leakage
44	Yakusitoge	Railway	CTM	1979	C(45–60)	6199	250	4.4-8.5	5.6-6.9	B	Spalling, crack in arch and sidewall, water leakage
45	Yabukami	Water	CTM	1941	C(40)	4856	100	4.85	4.85	B	Spalling in arch
46	Kamijo	Water	CTM	1927	C(24.2)	3265	95	3.83	3.42	B	Crack
47	Suhara	Water	CTM	1913	C(30)	1324	25	2.98	2.42	B	Crack
48	Ikazawa	Water	CTM	1920	C(47.6)	1322	49	2.12	2.52	B	Crack
49	Noborikawa	Water	CTM	1942	C(20)	2723	237	1.5	1.8	B	Crack

Damage degree *A1* corresponds to heavy damage requiring large-scale repair and reinforcement, *A2* corresponds to damage requiring repair and reinforcement and *B* corresponds to slight damage not requiring repair and reinforcement.
For tunnel lining, *C* is concrete, *CB* is concrete block and, *RC* is reinforced concrete.
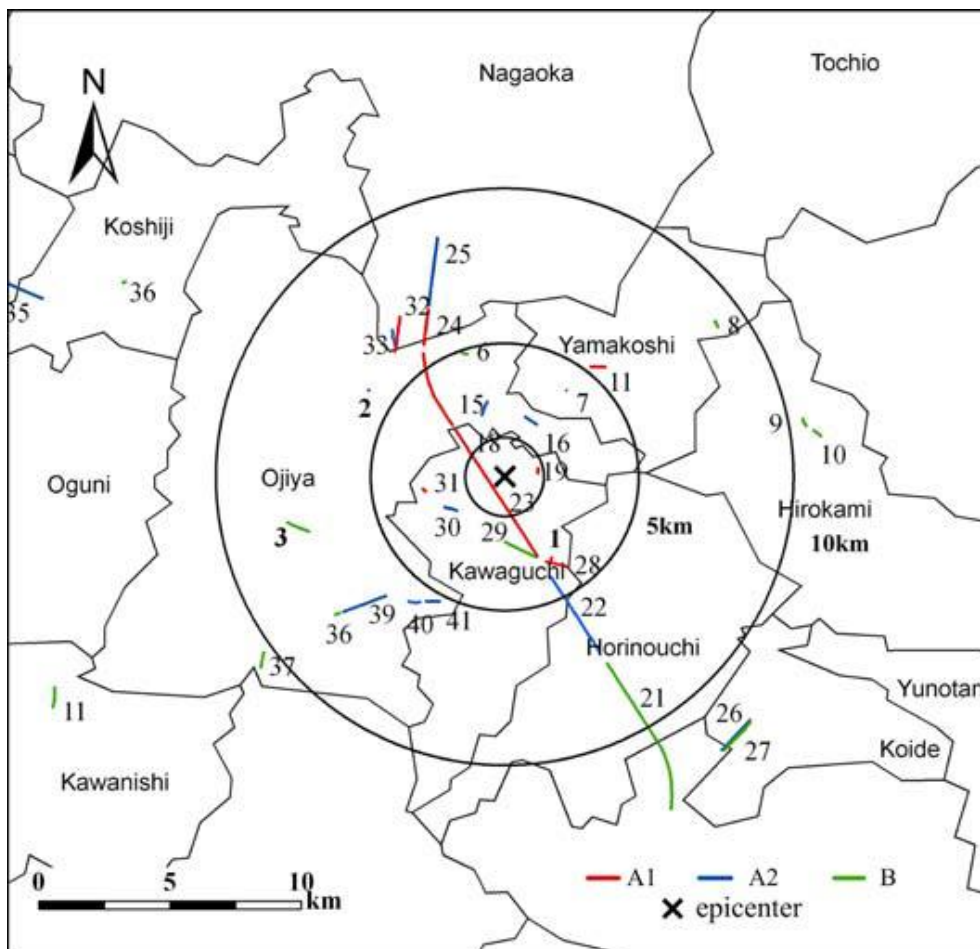
Figure 2.7: The distribution of the damaged tunnels (The numbers are the sequence number listed in Table 2.2.The color lines are the damage degree A1, A2 and B. (A1: Heavy damage requiring large-scale repair and reinforcement, A2: Damage requiring repair and reinforcement, B: Slightly damage not requiring repair and reinforcement) (Jiang et al., 2010)

2.2 2005 KASHMIR EARTHQUAKE

2.2.1 Introduction

An intense earthquake of magnitude 7.6 jolted northern areas of Pakistan and Pakistan administrated Kashmir at 08:50 (03:50UTC) on October 8th, 2005. The epicenter of the earthquake was located at latitude of 34.493^{o}N, longitude of 73.629^{o}E and focal depth of about 26 km (United States Geological Survey (USGS)). This is the location, around 90 km north-northeast of Pakistan's capital, Islamabad and 20 km northeast of Muzaffarabad, local capital of Pakistan administrated Jammu and Kashmir (Figure 2.8). The highest numbers of aftershocks (122) were recorded on October 9th, 2005 with a significant drop of aftershocks in subsequent days. The total aftershocks were 1778 at the end of 2005

(Pakistan Meteorological department, 2006). The earthquake resulted in more than 86,000 fatalities, 105000 people injured, 400,000 houses destroyed and 2.8 million people left homeless in northern Pakistan and Azad Jammu and Kashmir (Peiris et al., 2005a), and is by far one of the deadliest in the sub-continent.
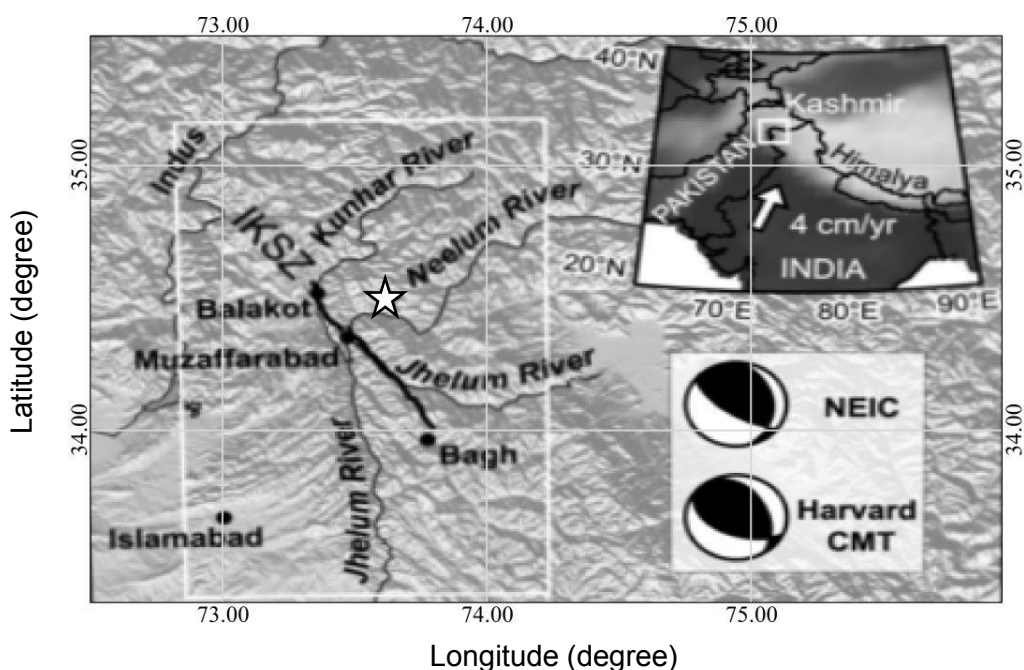
Figure 2.8: Epicentral map of 2005 Kashmir Earthquake along with the causative fault (thick black line). Star shows epicenter of the earthquake (Pathier et al., 2006).

2.2.2 **Physiography and Geological Settings**

The epicentral area lies in the lesser Himalayas, in Pakistan administrated Jammu-Kashmir. The climate of the area is monsoonal with an average annual precipitation of about 1510 mm, with a major portion falling as rain during the monsoon season (June-August). At higher altitudes (1500m above the see level), precipitation falls as snow during the winter (District Census Report, 1998).

The area devastated by the Kashmir earthquake is traversed by the Main Boundary Thrust (MBT) defining Hazara-Kashmir Syntaxis (HKS) (Figure 2.9). The causative Balakot-Bagh (B-B) fault, mapped by the Geological Survey of Pakistan prior to the earthquake, cuts HKS offsetting the MBT at the location where the MBT bends sharply from northwest to south (Figure 2.9). The fault has reverse separation with the northeast side moved up, which has been verified by high crustal deformation from satellite data and fault modeling [Sato et al., 2007]. Near Muzaffarabad, the fault separates Precambrian dolomite and limestone

(Muzaffarabad formation) on the northeast from Miocene Murree Formation on the southwest; farther southeast, the fault is entirely within the Murree Formation or forms the contact between the Murree and Kamlial formations (Figure 2.9) (Ahmad et al., 2009). Around Muzaffarabad city, failure occurred in Muzaffarabad Formation which forms steep valley slopes, many greater than 50° behind highly populated valley fills or branches of Jhelum River.
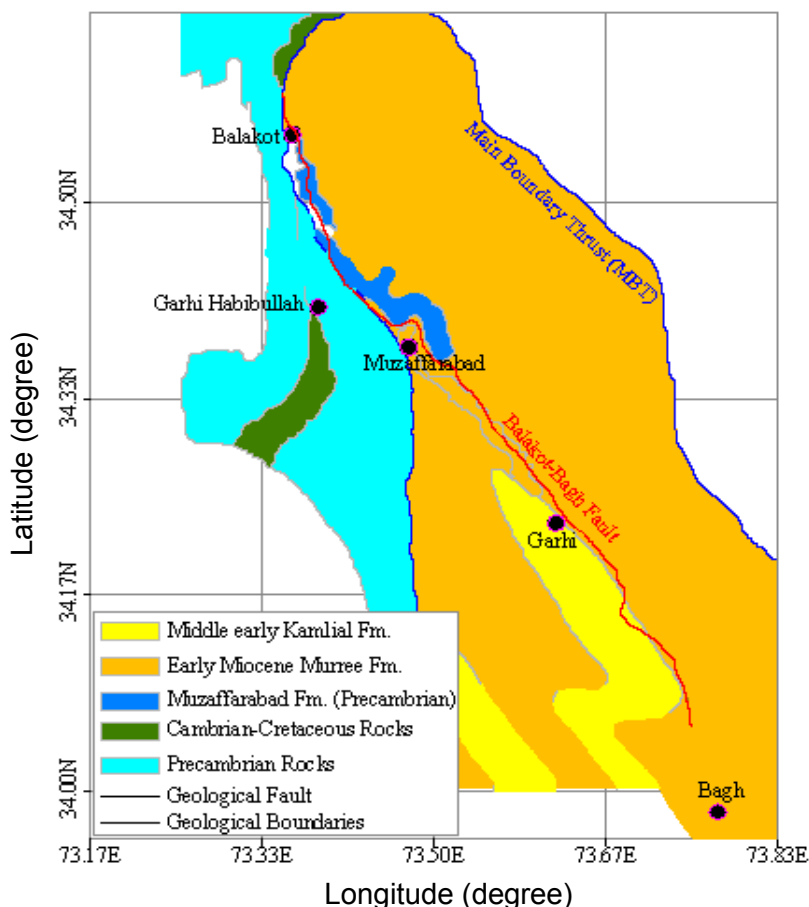
Figure 2.9: Simplified geological map of the epicentral area of 2005 Kashmir Earthquake with overlaid fault map. Balakot-Bagh fault (shown by red line) was responsible for the subject earthquake.

2.2.3   Devastations

Due to active seismicity, great relief, heavy monsoon rains, and accelerated erosion due to deforestation and construction, landsliding is one of the most prevalent hazards in the epicentral area. The earthquake triggered thousands of landslides throughout the region in an area of more than 7500 km^2, causing more than 1000 direct fatalities, destroying roads, and disrupting communication links. Blind reverse separation of the causative fault has

crushed and disintegrated dolomite slope surfaces along its total stretch. These crushed slopes are exploited by the extreme weather conditions (heavy monsoonal rains after very dry hot season) and a remarkable increase in slope failures and landslides was also reported due to rock weathering and rain infiltration in the years following the earthquake. Most (>90%) of the earthquake-induced landslides were rock and debris falls ranging from a few m^3 to >10^3 m^3 in size; but also included debris slides and debris flows (using Varnes' 1978 classification; Owen et al., 2008). Sato et al. (2007) interpreted 2424 landslides in 55km x 51 km epicentral area (Figure 2.10) using 2.5-m-resolution System Pour l'Observation de la Terre 5 (SPOT 5) stereo image.

The most worth mentioning is the massive Hattian-Bala landslide which flushed about four villages and blocked two tributaries of Jhelum River and created a huge landslide dam. Later this landslide dam was breached and caused flooding to its downstream reaches.
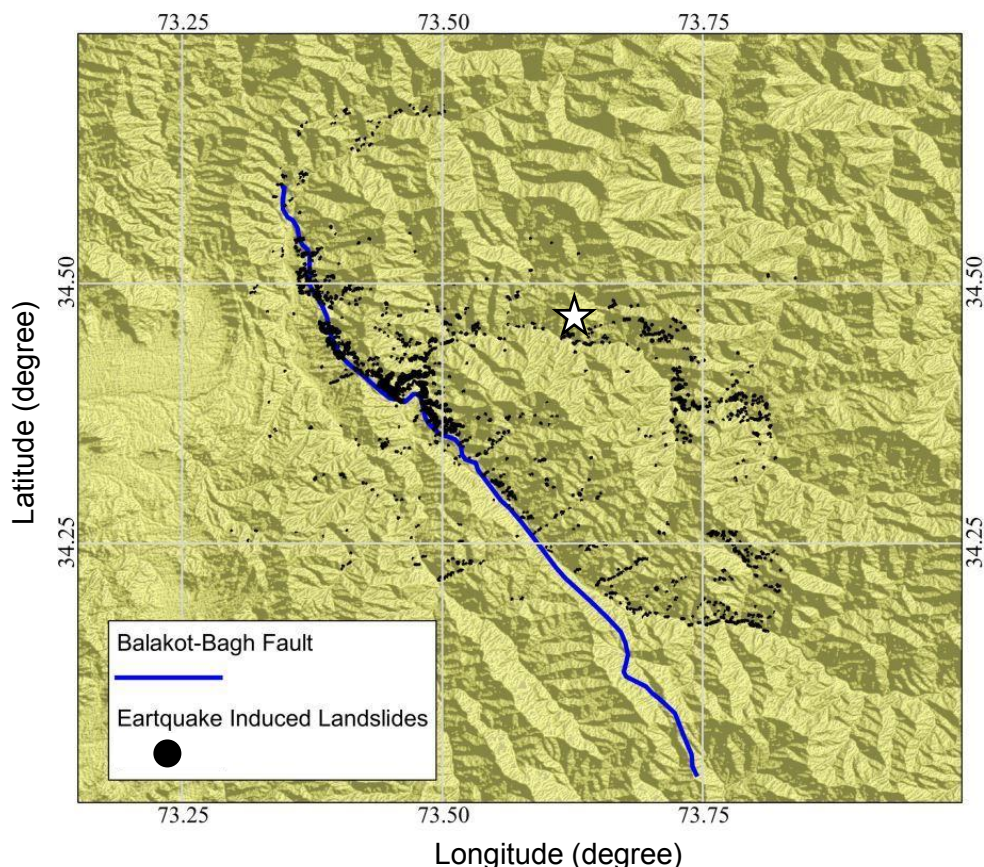
Figure 2.10: Landslide distribution map triggered by 2005 Kashmir Earthquake (after Sato et al., 2007). The star marks the location of epicenter.

2.3   SUMMARY

Mid-Niigata Prefecture Earthquake, Japan (2004) and 2005 Kashmir Earthquake, Pakistan are among the most catastrophic earthquakes our earth has experienced. Both the earthquakes hit rugged mountainous terrains and casted huge loss of lives and properties. In addition to their direct impacts, both the earthquake resulted in huge mass movements, which disrupted the natural channels and communication links, connecting sparse settlements. Socioeconomic and financial loss due to landslides, debris flows and other mass movements was highest in these earthquakes. Mid-Niigata Prefecture earthquake has also resulted in moderate to severe damage to underground facilities and life lines (railway and roadway tunnels, buried pipelines, drainage wells etc.). Being the two most pronounced earthquakes of most recent decade, their damage mechanism, cause investigation and their scientific justification are esteemed focus of this dissertation.

REFERENCES

1. National Institute of Earth Science and Disaster Prevention. (2004) Mid Niigata Earthquake. http://www.hrr.mlit.go.jp/saigai/H161023/1023_top.htmlS.

2. R. Honda, S.Aoi, H. Sekiguchi, N. Morikawa, T. Kunugi, and H. Fujiwara (2004). Ground motion and rupture process of the 2004 Mid Niigata Prefecture Earthquake obtained from strong motion data of K-net and KiK-net.
    http://www.kyoshin.bosai.go.jp/k-net/topics/niigata041023/index_e.htmlS, 2004.

3. N. Hirata, H. Sato, S. Sakai, A. Kato, and E. Kurashimo (2005). Fault system of the 2004 Mid Niigata Prefecture Earthquake and its aftershocks. Landslides 2:153-157

4. K. H. Yoong and A. Okada (2005). Surface deformations associated with the October 2004 Mid-Niigata earthquake: Description and discussion, Earth Planets Space, 57, 1093–1102

5. Y. Okamura, M. Watanabe, R. Morijiri, and M. Satoh (1995), Rifting and basin inversion in the eastern margin of the Japan Sea, Island Arc, 4, 166-181.

6. Y. Ikeda (2002). The origin and mechanism of active folding in Japan, Active Fault Research, 22, 67-70 (in Japanese with English abstract).

7. H. Sato, T. Iwasaki, S. Kawasaki, Y. Ikeda, N. Matsuta, T. Takeda, N. Hirata, and T. Kawanaka (2004), Formation and shortening deformation of a back-arc rift basin revealed by deep seismic profiling, central Japan, Tectonophysics, 388, 47-58.

8. Y. Yanagisawa, I. Kobayashi, K. Takeuchi, M. Tateishi, K. Chihara, H. Kato (1986). Geology of the Ojiya District. Geological Survey of Japan, Quadrangle Series (Scale 1:

50,000) Niigata (7) No. 50.

9. I. Kobayashi, M. Tateishi, T. Yoshioka, M. Shimazu, (1991). Geology of the Nagaoka District. Geological Survey of Japan, Quadrangle Series (Scale 1: 50,000) Niigata (7) No. 38

10. E. D. Martonne (1927), Regions of interior basin drainage. Geographical Review 17:397-414

11. Report of Zenkoji Earthquake, Central Disaster Prevention Council (2008), http://www.bousai.go.jp/jishin/chubou/kyoukun/rep/1847-zenkoJISHIN/

12. H. Kato, and H. Akabane (1986). Geology of Nagano District, with geological sheet map at 1:50,000. Geological Survey of Japan. 120.

13. Y. Kobayashi (1981). Causes of fatalities in recent earthquakes in Japan. Journal of Disaster Science 3:15-22.

14. D. S. Kieffer, R. Jibson, E. M. Rathje, and K. Kelson (2006). Landslides triggered by the 2004 Niigata Ken Chuetsu, Japan, Earthquake. Earthquake Spectra. 22, S47-S73.

15. N. Oyagi, S. Uchiyama, and T. Inokuchi (2008). Map of Landslides Caused by the 2004 Niigata-ken Chuetsu (Mid Niigata) Earthquake (MJMA=6.8). Technical Note of the National Research Institute for Earth Science and Disaster Prevention, 317.

16. S. Okamoto (1973) Introduction to Earthquake Engineering, University of Tokyo Press, Tokyo, 29-40

17. Y. Jiang, C. Wang and X. Zhao (2010). Damage assessment of tunnels caused by the 2004 Mid Niigata Prefecture Earthquake using Hayashi's quantification theory type II. Nat Hazards, 53:425–441.

18. S. Sharma and W. R. Judd (1991). Underground opening damage from earthquakes, Engineering Geology 30, 263-276.

19. Y. M. A. Hashash, J. J. Hook, B. Schmidt, J. I. C. Yao (2001). Seismic design and analysis of underground structures. Tunneling and Underground Space Technology 16, 247-273.

20. District Census Report, Population Census Organization, Government of Pakistan, Islamabad, Pakistan, 1998.

21. N. Peiris, T. Rossetto, P. Burton, and S. Mahmood (2005a). "EEFIT Mission: October 8, 2005 Kashmir Earthquake" Earthquake Engineering Field Investigation Team (EEFIT), The Institution of Structural Engineers

22. E. Pathier, E. J. Fielding, T. J. Wright, R. Walker, B. E. Parsons, and S. Hensley (2006). Displacement field and slip distribution of the 2005 Kashmir earthquake from SAR imagery, Geophysical research letters, Vol. 33, L20310.

23. H. P. Sato et al. (2007) Interpretation of landslide distribution triggered by the 2005

Northern Pakistan earthquake using SPOT 5 imagery. Landslides 4(2): 113-122

24. H. Ahmad, R. S. Yeast, MonaLisa (2009) "Geological setting of the 8 October 2005 Kashmir earthquake" J Seismology 13(3): 315-325.

25. D. J. Varnes (1978). Slope movement types and processes. In: Schuster, R.L., Krizek, R.J. (Eds.), Landslides: analysis and control. National Academy of Sciences, Transportation Research Board Special Report, vol. 76, pp. 12–33.

26. L. A. Owen, U. Kamp, G. A. Khattak, E. L. Harp, D. K. Keefer, M. A. Bauer (2008). Landslides triggered by the October 8, 2005, Kashmir earthquake. Geomorphology 94, 1–9

Chapter 3

3 Lagrangian Ground Displacements

3.1   INTRODUCTION

During an earthquake, stresses in the interior of the earth adjacent to the activated fault are redistributed leading to permanent ground deformations, which can be measured by comparing pre- and post-seismic geodetic observations. Most common methods to monitor landform changes during last two decades or so include GPS control measurement, level measurement, long baseline interface measurement etc. But these measurements are limited to certain areas and only monitor discrete points. Due to the remoteness of disaster struck areas, usually high mountains, and due to its spatial extension, remote sensing is a cost efficient and more practical tool for monitoring terrain dynamics.

Recent development of remote sensing technologies such as Laser Imaging Detection and Ranging Technology (LIDAR) and Interferometric Synthetic Aperture Radar (InSAR) has enabled the acquisition of images of landforms and the changes in elevation with high precision. However the methods allow us to detect displacements only in the Eulerian description, in which the description of motion is made in terms of the spatial coordinates which does not follow the motion of soil particles. When InSAR images are taken from different satellite flight directions, the 3-D displacement field of the terrain can also be determined. These attempts have been made by Fialko et al. (2005), Wright et al. (2004), Tobita et al. (2001), etc. Nevertheless, it can still not distinguish the shallower deformations (e.g. landslides, debris flows, manmade changes etc.) and, furthermore, difference of spatial resolution of LIDAR and InSAR images is another concern.

Konagai et al. (2009) compared two digital elevation models for the mountainous terrain jolted by the 2004 Mid-Niigata Prefecture Earthquake, and obtained changes in elevation were converted to Lagrangian displacements assuming that a coherent mass movement (Lagrangian displacement) changes gently in space such that neighboring pixels would experience the same Lagrangian displacements. Since Konagai et al. used high 2-m resolution DEMs, much of their energy was devoted to separate tectonic deformations from shallow coherent mass movements, which appeared as landslides over the entire mountainous terrain of the target area. As long as geotechnical hazards and rehabilitation

issues are to be discussed, we need to have both shallow and deeper soil displacements. This chapter highlights the deeper part of ground deformation and improves Konagai's original method in a manner such that shallow displacements can be separated in a more reliable manner and more precise ground displacements can be obtained.

3.2   MATHEMATICAL FORMULATION

A method, initially proposed by Konagai et al. (2009) to obtain Lagrangian components of tectonic displacements considering three consecutive patches of the terrain surface arranged in a triangular position, has been improved to incorporate rotations of the soil patches about the planar axes. The procedure for filtering out landslides and large scale man-made changes has been also revised.

Landforms herein are given as raster graphic images of pixels having information of their elevations, which pixels (nodes) are arranged in square as a background   Eulerian grid. It is assumed that there is a planar ground patch, *i*, immediately above a node *i*, and a soil particle *k* on this patch is exactly at the point where node *i* is projected (Figure 3.1).This patch with inclinations of θ_{x_1} and θ_{y_1} in *x* and *y* directions, respectively, moves to a new position, changing the inclinations to θ_{x_2} and θ_{y_2}. Figure 3.2 shows the two-dimensional system illustrated in an easy-to-understand manner. Referring to Figures 3.1 and 3.2, Eulerian change in elevation ($\Delta_{z,i}$), which is measured exactly above node *i*, is expressed in terms of the Lagrangian vector, $\{\Delta_{x,k} \ \Delta_{y,k} \ \Delta_{z,k}\}$, of the movement of the soil particle, *k*, on this patch as

$$[-t_{x_2,i} \quad -t_{y_2,i} \quad 1] \begin{Bmatrix} \Delta_{x,k} \\ \Delta_{y,k} \\ \Delta_{z,k} \end{Bmatrix} = \Delta_{z,i} \qquad (3.1)$$

where $t_{x_2,i} = tan\theta_{x_2}$ and $t_{y_2,i} = tan\theta_{y_2}$, i.e. direction tangents of the soil patch in its new position.

Arranging three soil patches, i_1, i_2 and i_3, immediately next to each other in a triangular manner (Figure 3.3), and using the displacement of its center, $\{\Delta_{x,k} \ \Delta_{y,k} \ \Delta_{z,k}\}^T$, as the representative Lagrangian displacement vector of the triangle, the following set of solvable simultaneous equations is obtained.
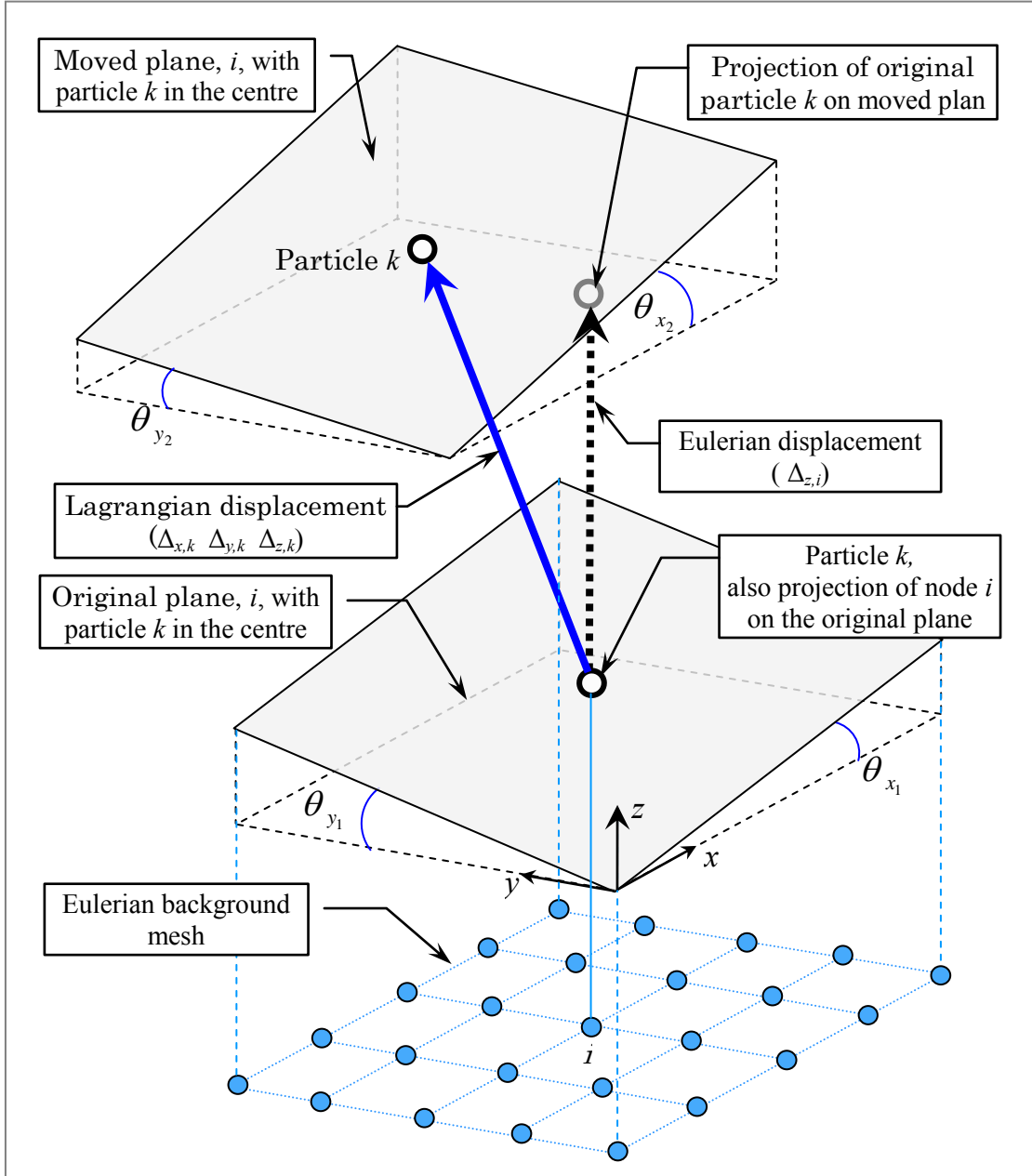
Figure 3.1: Description of the method to convert Eulerian changes in elevation to Lagrangian displacements

$$
\begin{Bmatrix} \Delta_{z,i_1} \\ \Delta_{z,i_2} \\ \Delta_{z,i_3} \end{Bmatrix} = \begin{bmatrix} -t_{x_2,i_1} & -t_{y_2,i_1} & 1 \\ -t_{x_2,i_2} & -t_{y_2,i_2} & 1 \\ -t_{x_2,i_3} & -t_{y_2,i_3} & 1 \end{bmatrix} \begin{Bmatrix} \Delta_{x,k} \\ \Delta_{y,k} \\ \Delta_{z,k} \end{Bmatrix} = \mathbf{T} \begin{Bmatrix} \Delta_{x,k} \\ \Delta_{y,k} \\ \Delta_{z,k} \end{Bmatrix} \tag{3.2}
$$

Solving the above set of simultaneous equations (eq. 3.2) for all triangles within the target zone, Lagrangian components of displacement vectors $\{\Delta_{x,k} \ \Delta_{y,k} \ \Delta_{z,k}\}^T$ can be obtained for the entire target zone.
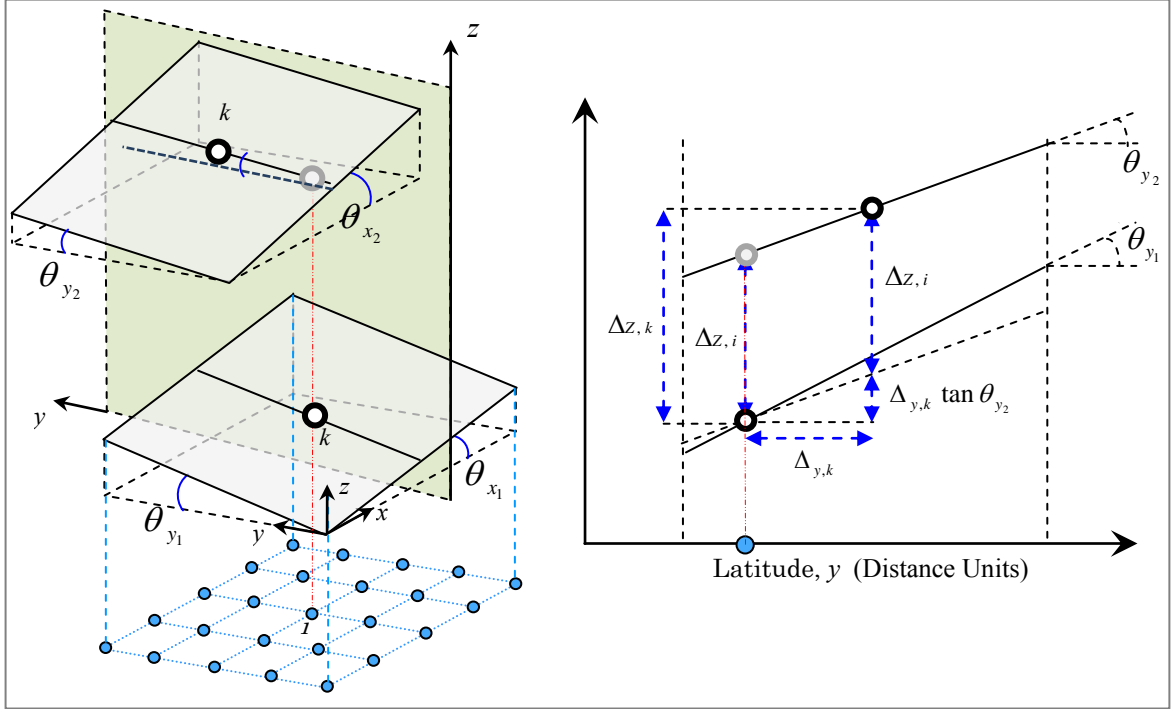
Figure 3.2: Description of the method in two dimensional settings to simplify the concept. $\Delta_{z,i}$ is the Eulerian change in elevation while $\{\Delta_{y,k}\ \Delta_{z,k}\}$ are the Lagrangian displacement components. Although particle k and consequently the soil patch *i* can move to any arbitrary position; however, to make the 2D illustration easily understandable, movement of particle k only in y direction is shown which makes the cut plane parallel to y-axis.

3.2.1   Filtering for Shallow Ground Displacements

The obtained Lagrangian vectors show motion of the soil particles on the ground surface, which can be greatly affected by landslides and man-made changes. To separate tectonic deformations from the entire Lagrangian displacements, landslides and large scale manmade changes are filtered out by limiting the Lagrangian vertical component of displacement below a threshold value. This threshold value is set so that the center of moved plane remains within the projected boundary of the original plane. The following filtering criterion is used:

$\Delta_{z,k}$ > Threshold for Lagrangian vertical displacement

$$\Delta_{z,k} > \{t_{x_2,i} \quad t_{y_2,i} \quad 1\}\{\Delta_{x_{lim}} \quad \Delta_{y_{lim}} \quad \Delta_{z_{lim}}\}^{\mathrm{T}} \tag{3.3}$$

where, $\Delta_{x_{lim}}$ and $\Delta_{y_{lim}}$ are half the planar dimensions of the soil patch in *x* and *y* direction, respectively. $\Delta_{z_{lim}}$ is the vertical movement of earth's crust. While applying to the Mid-Niigata Prefecture Earthquake, the value of vertical movement can be determined to be 1.36 meters from the maximum vertical tectonic displacement of the main shock in this

earthquake (Hikima and Koketsu, 2005). This value can be set to any level depending on the objective of analysis for each study case.
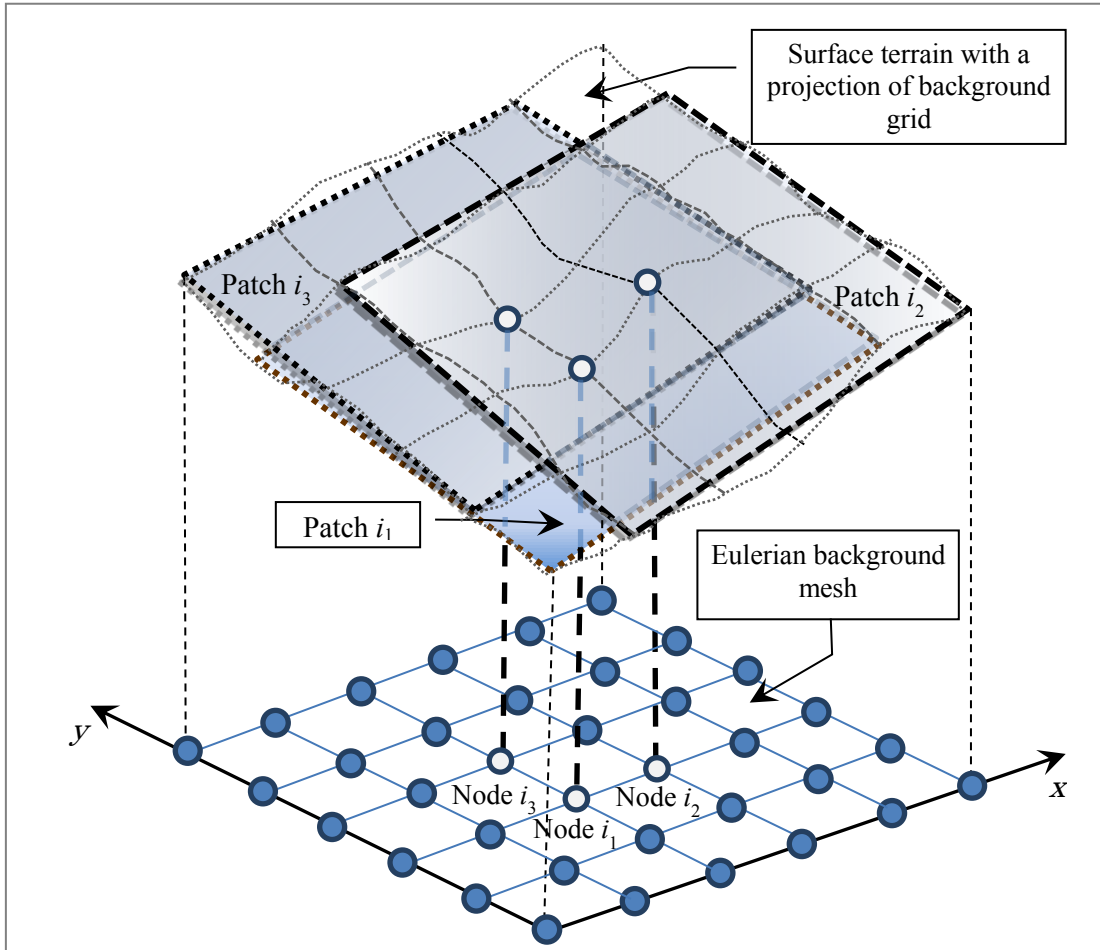
Figure 3.3: Three consecutive soil patches arranged in a triangular pattern to solve a set of simultaneous equations for Lagrangian components of displacement.

3.2.2   Filtering for Ill- Conditioned System of Equations

To obtain a reliable solution, the condition of coefficient matrix **T** in the equation (3.2) is important. A system of equations is considered to be well-conditioned if a small change in the coefficient matrix or a small change in the right hand side results in a small change in the solution vector. This small change in the solution vector is namely important digits or tolerance of accuracy. The matrix condition can be determined as;

$$Cond(T) = {\alpha_{tol}}/{\varepsilon_{machine}} \tag{3.4}$$

Where machine epsilon, $\varepsilon_{machine}$, gives an upper bound on the relative error due to

rounding in floating point arithmetic.

If MATLAB is used for calculation, the machine epsilon of default data type (double precision) is obtained as $\varepsilon_{machine} = 2.2201 \times 10^{-16}$ with "eps" command. Setting the tolerance of calculation accuracy to any desired level, the condition of matrix T can be obtained by equation (3.4). All the sets of equations not fulfilling this criterion need to be filtered out to get a reliable solution. For the example case described in the following section, α_{tol} is set at 0.1.

3.2.3   Moving Average Method

However, the obtained Lagrangian displacement components often show a remarkable scatter. Man-made changes during the time between two DEM's and presence of some non-surface objects on digital surface models might be the most prominent among possible causes. Therefore, the moving average method was used for overall features of displacements. Assuming that the scattered values follow the Gaussian distribution within a square window, the most frequent value (mode) is interpreted to be the real vector of the soil displacement for this area. Sweeping the entire zone with this square window, the whole picture of the deformation can be obtained.

The size of the smoothening window has to be determined from its physical interpretation. The window size, to discuss the tectonic deformations, is desirable to be larger than the largest hidden landslide in the target area to minimize the effect of the hidden coherent landslide mass movements. At the same time, the size should not be too large to allow significant variation of the tectonic deformation within the smoothening window.

3.3   APPLICATION TO MID-NIIGATA PREFECTUR EARTHQUAKE

3.3.1   Targeted Study Area

The area chosen for this study is a low-raised mountainous terrain of Japan which was jolted by the magnitude 6.8 Mid-Niigata Prefecture Earthquake of October 23rd, 2004 and had very clear active folding geological structure (Yoong and Okada, 2005). Like other historic earthquakes hitting active folding areas, the Mid-Niigata Prefecture Earthquake triggered a large number of landslides along with tectonic displacements that have caused some problems for rehabilitating the affected areas. An 11 × 7.5 km active folding area of Yamakoshi mountainous terrain (Figure 3.4) is selected as target zone to get the Lagrangian displacements from an available set of digital elevation models (DEMs).
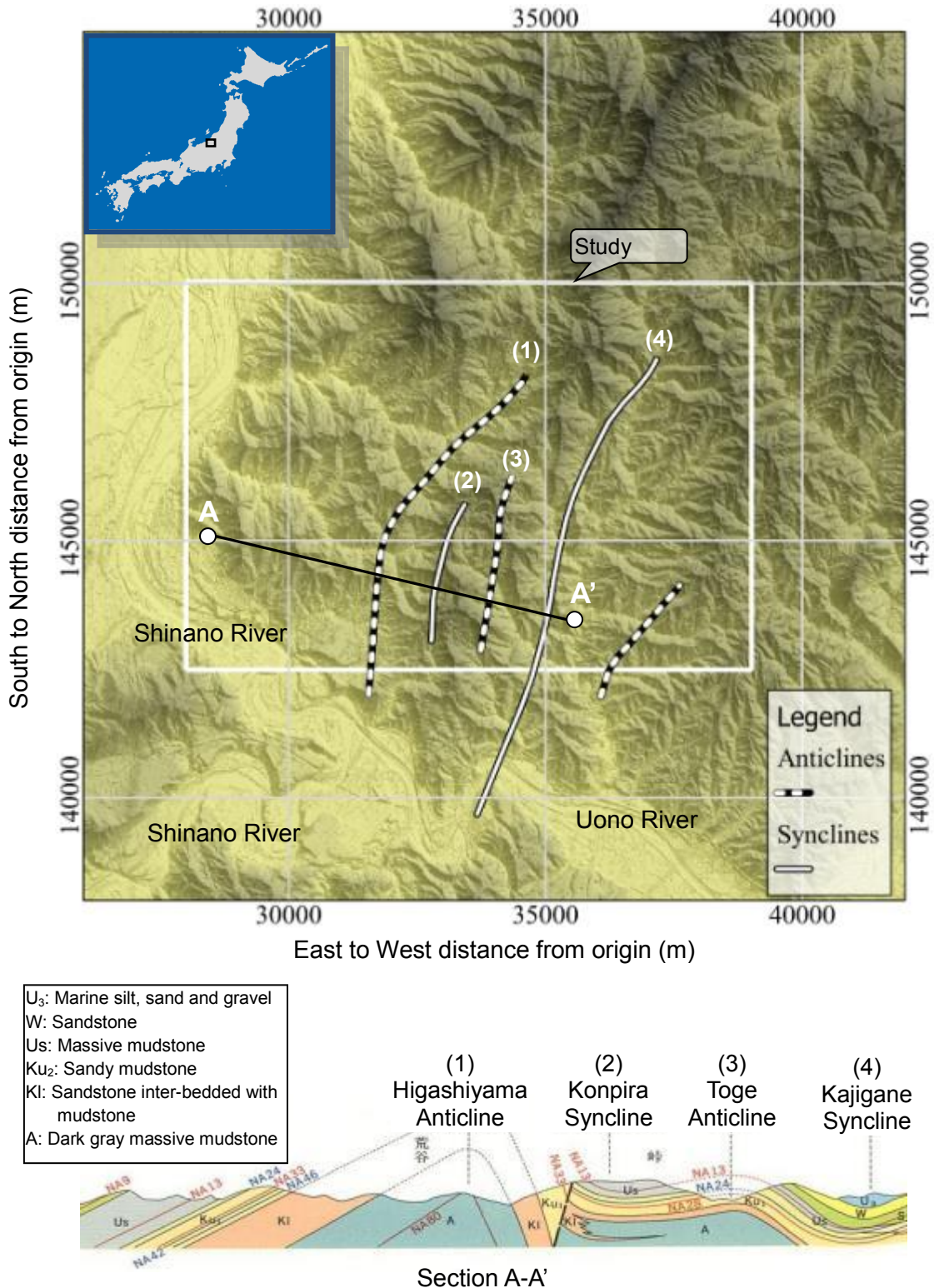
Figure 3.4: Terrain map for the epicentral ear of Mid-Niigata prefecture Earthquake along with geological details. Solid white line shows targeted study area. Topographical mapping is on the JGD/2000 Japan Rectangular Coordinate System VIII with its southwest corner located as the origin at 138°30'00"E, 36°00'00"N.

3.3.2   Preparation of Digital Elevation Models (DEMs)

There were only 13 triangulation pints within the target zone and 9 out of those 13 points were not considered to have been affected by landslide. However, the points are so sparsely distributed that a thorough discussion can't be made upon a clear image of displacement. Therefore, precise digital elevation models (2m resolution) before and one day after the Mid-Niigata Prefecture Earthquake (Oct. 24) were used for the analysis (Figure 3.5).
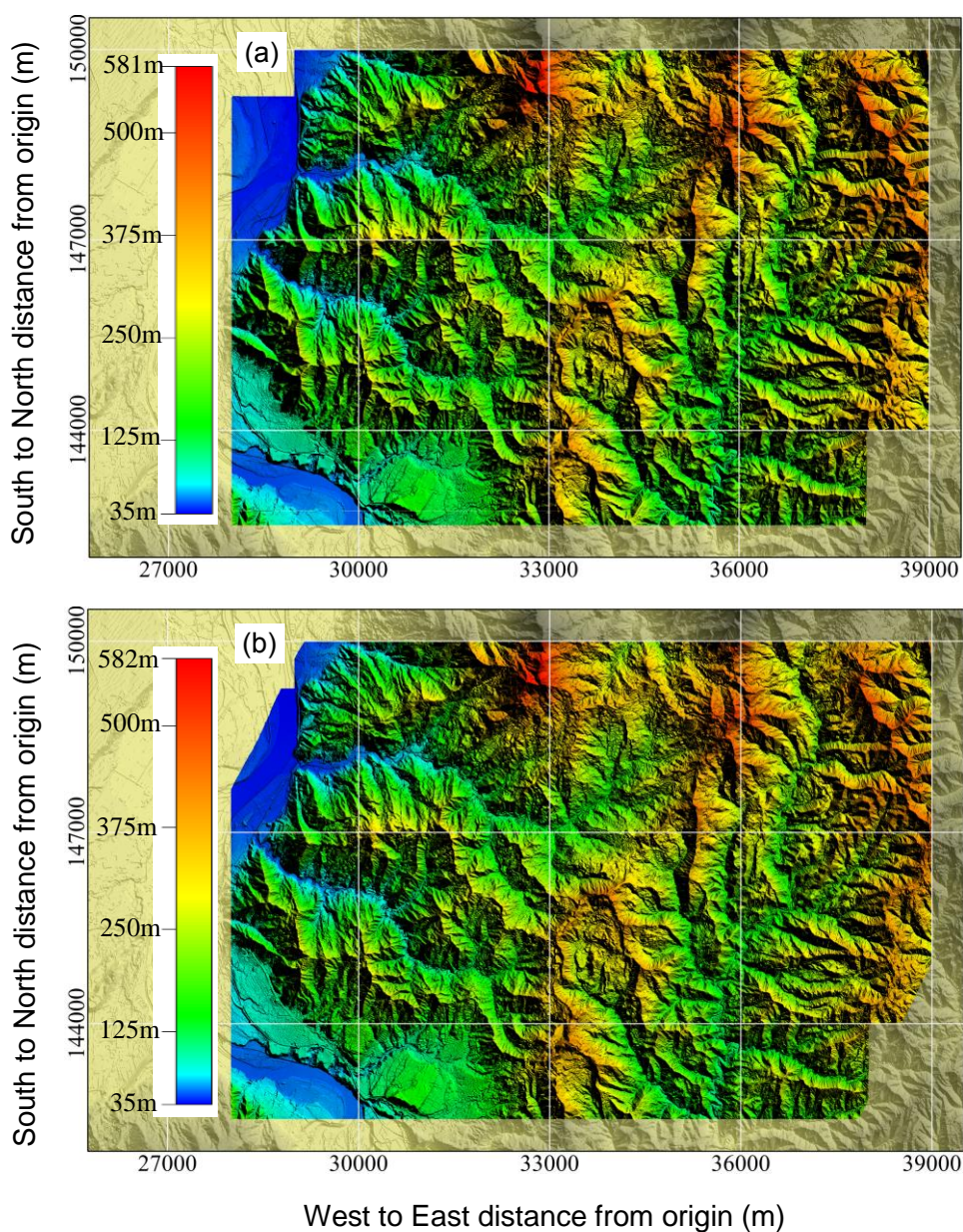
Figure 3.5: Digital elevation models of the target area (a) Pre-earthquake time DEM prepared from aerial photographs of 1975-1976 and triangulation data of 1986 (b) Post-earthquake time DEM obtained by LIDAR scanning on October 24, 2004. Topographical mapping is on the JGD/2000 Japan Rectangular Coordinate System VIII.

No precise DEM was available for the target zone before the earthquake. Therefore a series of aerial photographs on a scale of 1/8000 to 1/10,000, taken in 1975–1976 by Geospatial Information Authority of Japan, together with the triangulation data of 1985 were used to prepare a precise DEM of the topography. The DEM for the post-earthquake time (Oct. 24, 2004) was obtained using the Laser Imaging Detection and Ranging technology (LIDAR) (JSCE active folding project, 2008). Both the pre- and post-seismic DEMs, having a spatial resolution of 2 meters, were carefully prepared and all the non-surface objects were filtered out.

3.3.3   Ground Features and Optimized Nominal Plane

The size of the soil patch (mentioned in Figures 3.1 and 3.3) is to be determined from the ground features and the objective of the analysis. As is shown in Figure 3.6, there were a number of manmade changes of landform over the 28 years interval between DEMs prepared in 1976 and 2004. These changes include creation of ponds for Koi-fish farm business, road widening, etc.
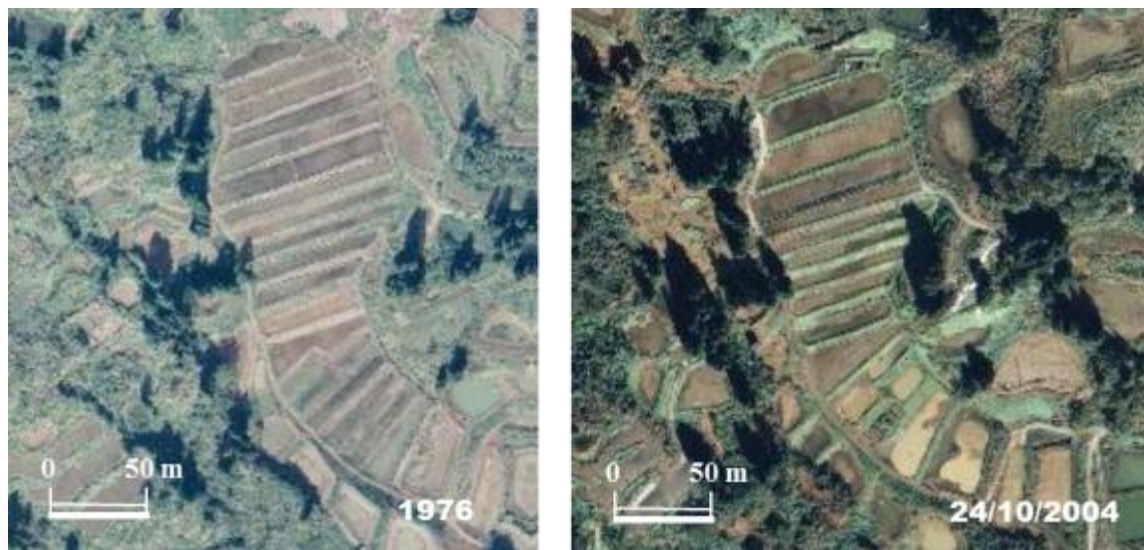
Figure 3.6: Improvement of farmland in Yamakoshi: Location of the lower left corner of each photo is 37.337928°N, 138.878678°E. The left and right photos were taken respectively in 1976 (Geospatial Information Authority of Japan) and on Oct. 24th, 2004 (JSCE Active folding Project, 2008). Some of the terraced paddy fields were converted to Koi fish ponds.

The size of soil patch should be large enough to minimize the effect of these earthworks and to contain the maximum targeted movement of a particle. Reflecting these manmade changes and with the objective of tracking surface tectonic displacements, an 8m × 8m soil

patch, least-square regressed from the points in the square domain surrounding the center point, is used. In order to apply for any other case study, the required resolution of DEM and size of soil patch may vary depending on the target to be achieved. To monitor large soil movements like landslides, a larger soil patch with relatively crude spatial resolution of DEM may serve the purpose; but, of course, finer resolution of DEM gives more refined pattern of displacement.

3.3.4   Lateral and Vertical Components of Ground Displacement

First of all, large changes in elevation were filtered out by applying the filtering criteria. Distribution of the filtered points gives good correlation with the landslide map (Figure 3.7), making this method capable of tracing landslides. At the lower left corner of the target zone, Shinano River is located and much flatter topography is present (Figures 3.4 and 3.7). Large bunch of filtered points in this area is possibly due to the combined effect of reflection from river water, ill conditioned system of equations for the flat land and fluctuation in the water level.

Figure 3.8 shows lateral components of Lagrangian ground displacements extracted from the DEMs sweeping the whole target zone with a 1400m x 1400m smoothening window. Shinano River Office, Hokuriku Regional Bureau of the Ministry of Land, Infrastructure and Transport (MLIT), has been measuring exact locations of bench marks along both the Shinano and Uono Rivers on regular basis. Lateral components of the bench marks' displacements due to the earthquake are also plotted on Figure 3.8. There is a NNE-SSW trending 1 to 2 km wide belt of large eastward movement to the west of and along the Kajigane syncline. This belt of lateral displacements seems to have appeared on the hanging wall side of the line of intersection between the ground surface and the straight extension of the hidden deep-dipping fault rupture plane for the major event, whose geometry was estimated by Hikima and Koketsu (2004). The second cluster of large lateral displacement vectors that has appeared 4 to 5 kilometres west of the Kajigane Syncline, is near the projection on the ground surface of the hidden fault rupture plane for the first largest aftershock of M6.3, which took place at 18:03 JST, about 7 minutes after the main event (Hikima and Koketsu, 2004). While comparing the lateral components of Lagrangian ground displacements with landslide map of Figure 3.7, it is found that large clusters of ground displacements are concordant with thick clusters of landslides.
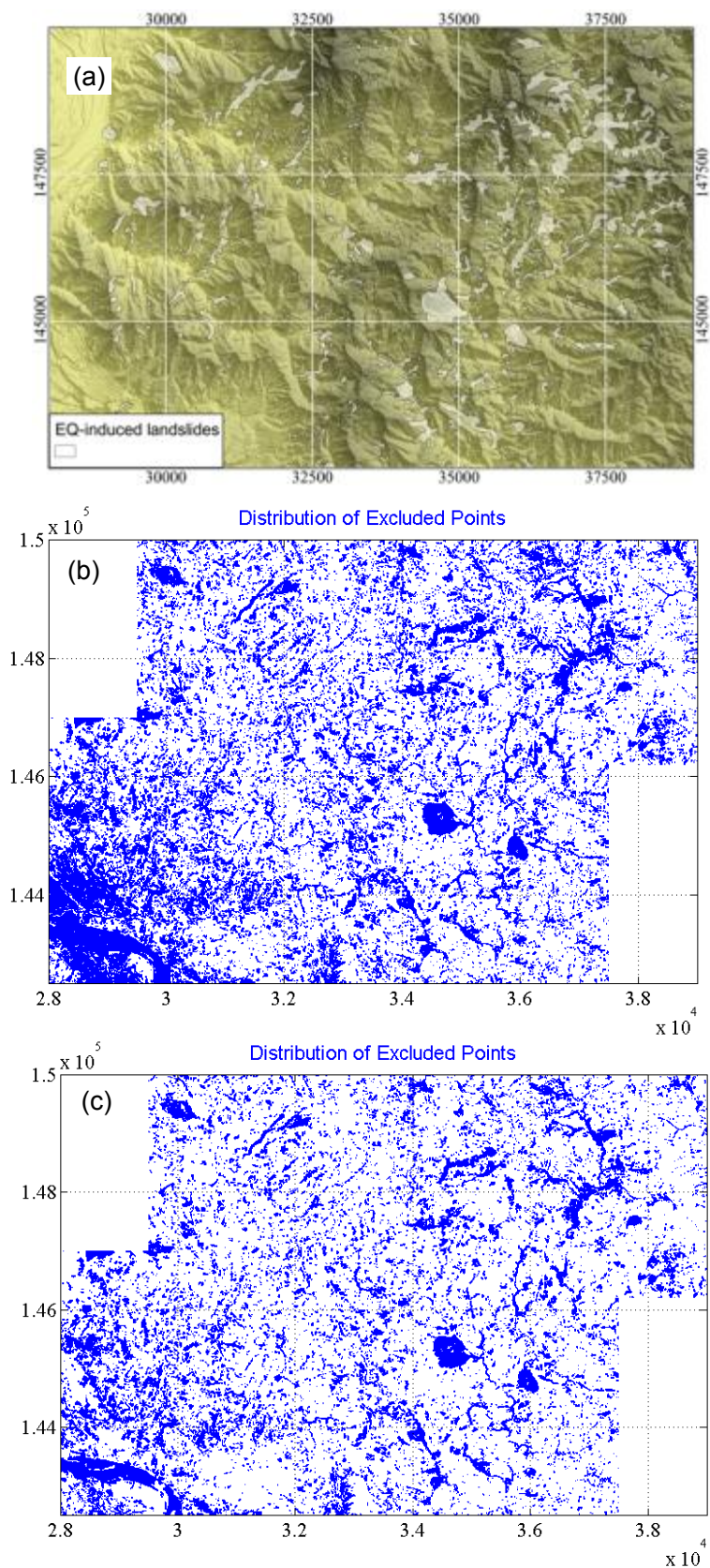
Figure 3.7: Evaluation of filtering criteria (a) earthquake induced landslides with in the study area (b) distribution of the filtered points for landslides, manmade changes and ill conditioned tangential matrices (c) distribution of filtered points for landslides and manmade changes.
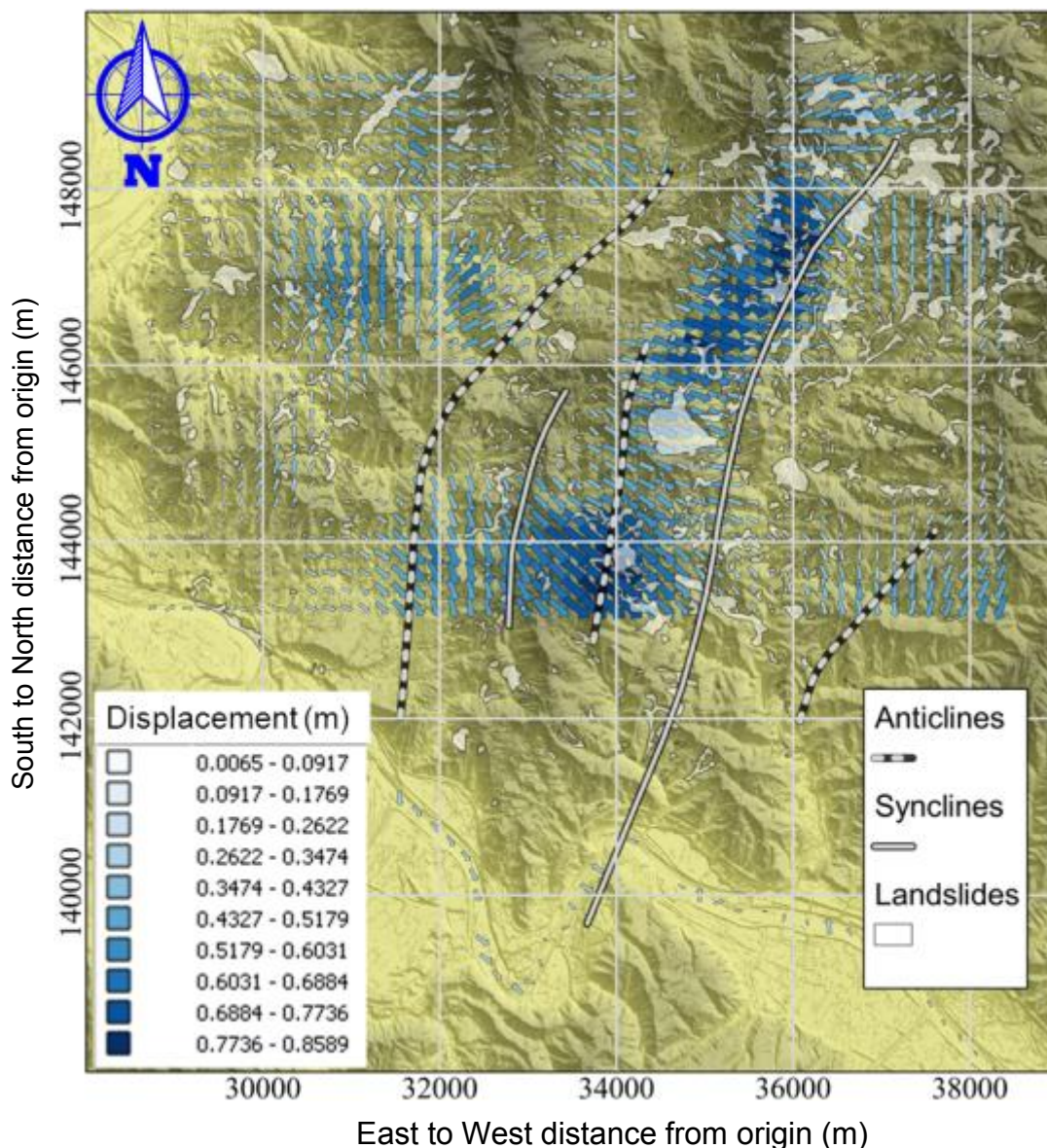
Figure 3.8: Lateral components of Lagrangian ground displacements for the study area. Topographical mapping is on the JGD/2000 Japan Rectangular Coordinate System VIII.

Figure 3.9 shows vertical components of Lagrangian ground displacements. It is notable that there are two areas in the target zone, which have been pushed up by 1.0 to 1.5 meters. The most remarkable hump spreads wide across the south-western part of the study area where the Uono River joins the Shinano River. The Uono River, after flowing straight west through a flat wide spread valley of Horinouchi, meets the sedimentary silty sand rock ridge (Figure 3.10(a)). The river then abruptly changes its direction, from SE-NW to NE-SW, along this rock ridge, making a sharp down-folded bend. Then it forces its way through the narrow and lowest points among the mountains making a sharp up-folded bend. On the geological map of this area (Yanagisawa et al., 1986), the approximately 2 km-long stretch of the Uono River between these two bends continues straight to both the

Kajigane and the Kodaka synclines at its north and south ends, respectively, suggesting that this 2 km-long stretch of the river is a part of the large Kajigane syncline.
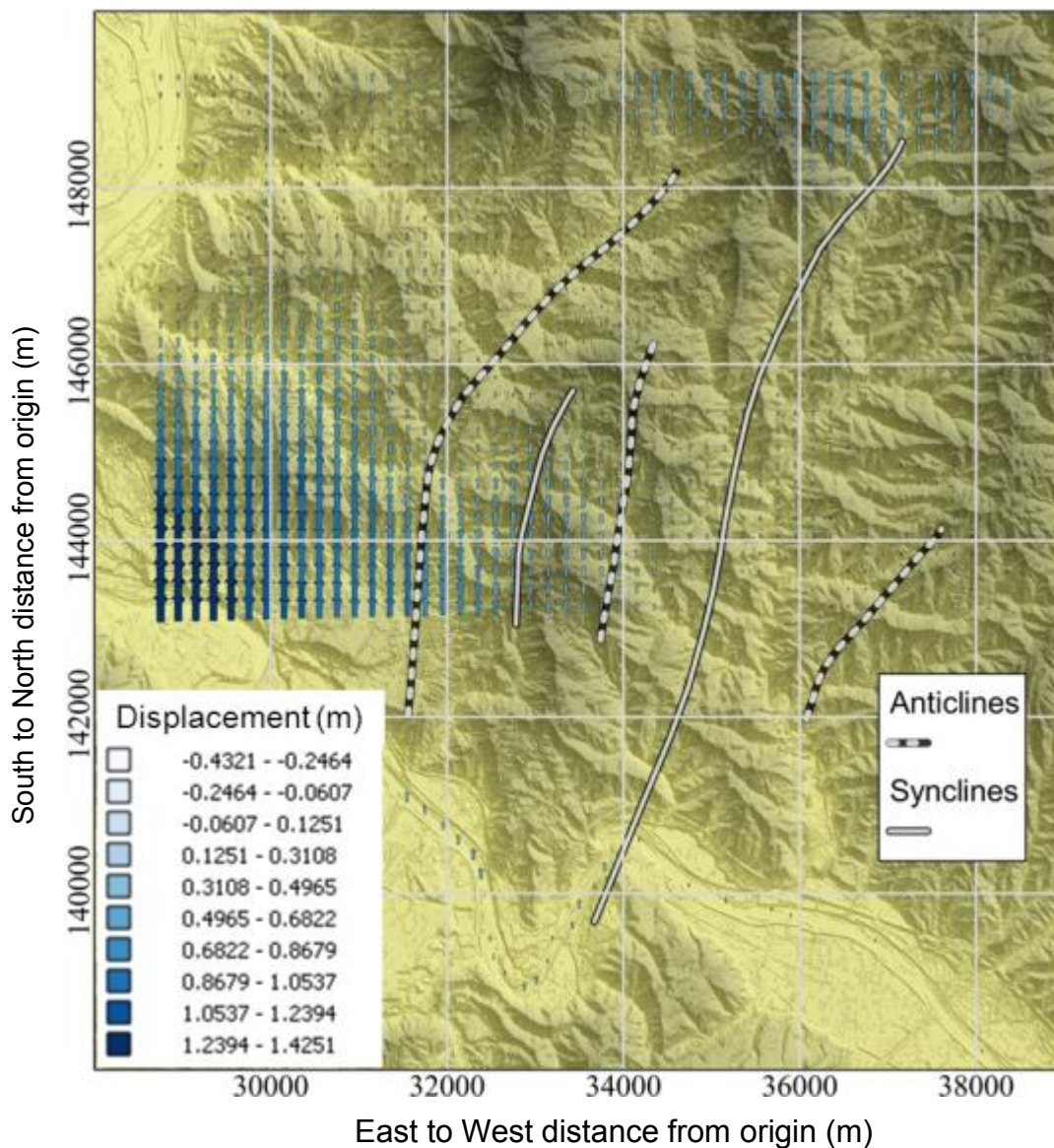
Figure 3.9: Vertical components of Lagrangian ground displacements for the study area. Topographical mapping is on the JGD/2000 Japan Rectangular Coordinate System VIII.

The areas along the upper reach of this part of the Uono River were flooded due to heavy rainfall of June 27th-28th, 2005, about 8 months after the earthquake, and were flooded again in heavy rains of July 2011 (Figure 3.10). Assuming that the same amount of water in the 2005 rain flowed down the Uono River as existed before the earthquake (ignoring the landform changes caused by the Mid-Niigata Prefecture Earthquake), possible water depths at all bench marks along the 57.5km-long flooded zone (from BM No. 15 at 37.26642°N, 138.862209°E, to BM No. 72.5 at 37.25923°N, 138.899975°E) were estimated by using the Manning empirical equation (open circles in Figure 3.11, (Dooge J.C.I., 1992)).
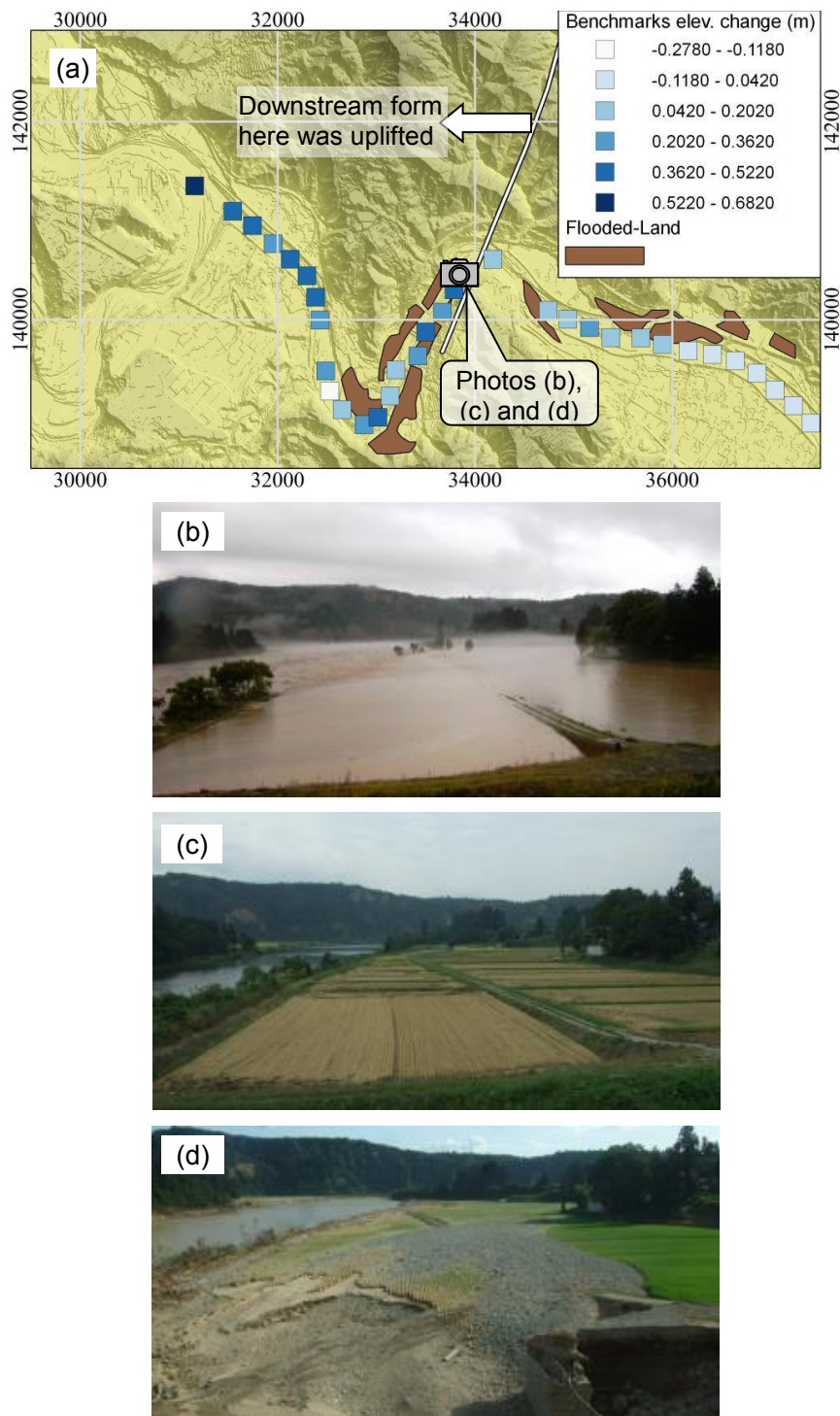
Figure 3.10: Farmlands flooded in the heavy rain of June, 2005, about eight months after the earthquake. (a) Locations of flooded farm lands (Hokuriku Regional Agricultural Administration Office, Ministry of Agriculture, Forestry and Fisheries, and Uonuma City), and change in elevations at benchmarks along Uono River on Zone VIII of the Japanese National Grid System (Shinano River Office, Hokuriku Regional Bureau of MLIT) (b) Flooded area near Benchmark No. 42.5km (Photo by Kotajima, S., 28th June, 2005) and (c) a photo at a later date from the same location (37.259828°N, 138.876801°E) as above (Photo by Konagai, K., 19th September, 2010) (d) the same area flooded again in heavy rains of July 2011 (Photo by Konagai, K., 4th August, 2011).

For this estimation, precise dimensions for the river cross-sections and inclinations at all benchmarks before and after the earthquake were provided by the Shinano River Office, Hokuriku Regional Bureau of the Ministry of Land, Infrastructure and Transport (MLIT). Solid circles in Figure 3.11 show the actual water levels at all bench marks reached in the 2005 flood, while open circles show virtual water levels calculated for the Uono River as it existed before the earthquake. At almost all points, the virtual water levels (open circles) are lower than those (solid circles) reached in the 2005 real flood. Actual water levels were higher than the high water levels (HWL) at bench marks # 37.5, # 52.5 and # 62.5, while virtual water levels at these points do not reach the high water levels. This figure thus suggests that there was a cause-and-effect relation between the earthquake-induced tectonic deformation and the flooding of June, 2005.
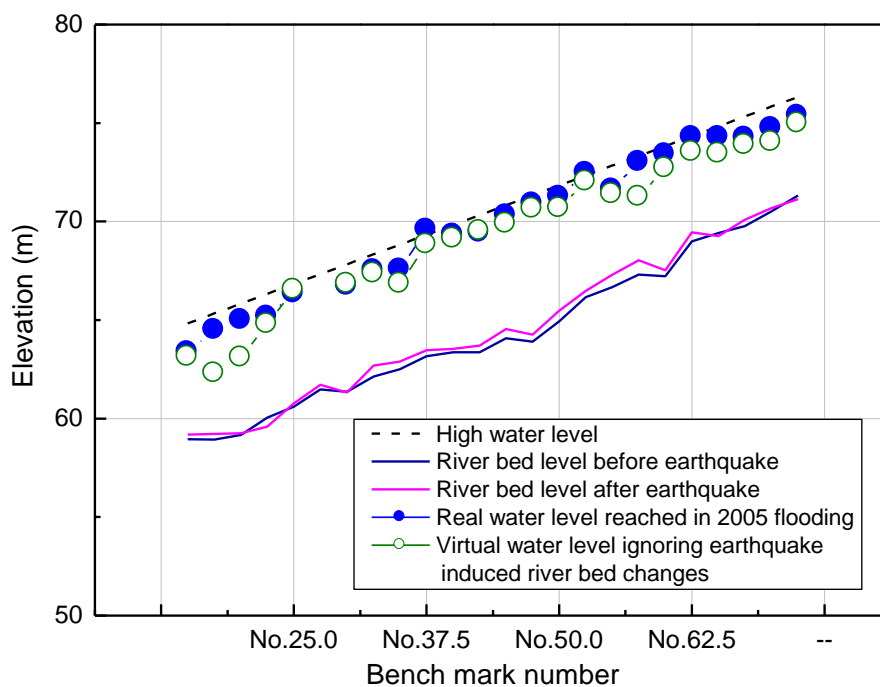
Figure 3.11: Water level reached during the flood of June 2005 and the virtual water level estimated from manning's formula.

3.3.5   Smoothening Window and Calculation Accuracy

There were nine triangulation points within the target zone which were not considered to be affected by the landslides (Figure 3.12 and table 3.1), set and measured by Niigata Prefecture for the purpose of road construction. Figure 3.13 shows a promising accuracy of the calculated Lagrangian ground displacement components against the triangulation data as compared to Eulerian changes in elevation.
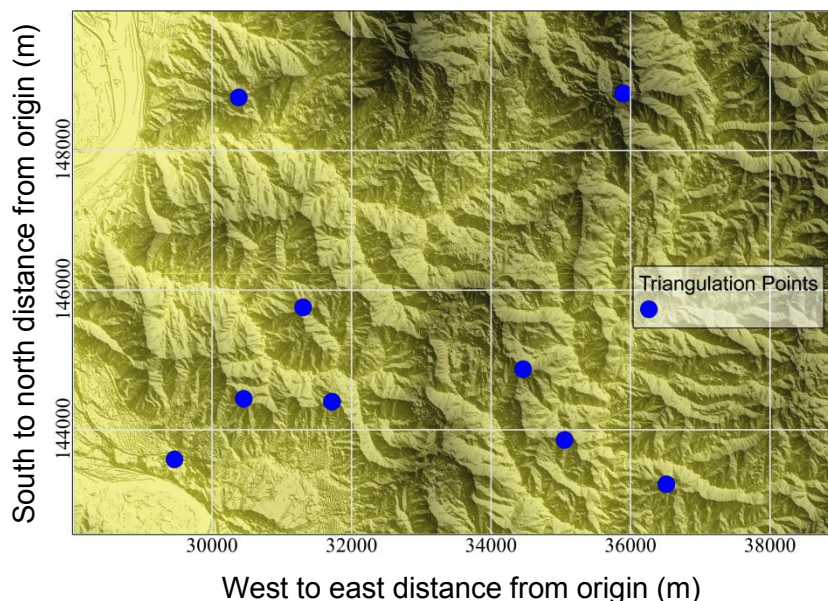
West to east distance from origin (m)
Figure 3.12: Position of triangulation points within targeted study area.

Table 3.1: Triangulation points with in the targeted study area. Easting and northing is the distance from the origin of Zone VIII on Japanese national grid system

Number	Easting	Northing	ΔX	ΔY	ΔZ
	(m)	(m)	(m)	(m)	(m)
1	30383.69	148759.80	-0.080	0.487	0.330
2	35894.37	148816.80	0.183	0.209	0.720
3	36512.94	143221.50	-0.326	-0.131	-0.050
4	35054.97	143855.20	0.883	-0.823	0.260
5	34459.33	144868.60	0.547	-0.327	0.440
6	29461.64	143576.40	-0.121	-0.128	0.970
7	30454.47	144444.20	-0.133	-0.124	1.040
8	31306.06	145754.40	-0.421	0.278	0.800
9	31719.38	144402.80	-0.215	-0.404	0.870

The selected size of the smoothening window (1400m x 1400m) should be larger than the largest landslides in the target area. Within the target zone, active folding structure has an average fold length of about 2.8km. Therefore, selection of half the fold length as smoothening window will not allow significant variation within the smoothening window. A sensitivity analysis has also been carried out for different sizes of smoothening windows. Figure 3.14 shows that a 1400m x 1400m smoothening window gives closest correlation with the triangulation measurements.

(a)

(b)
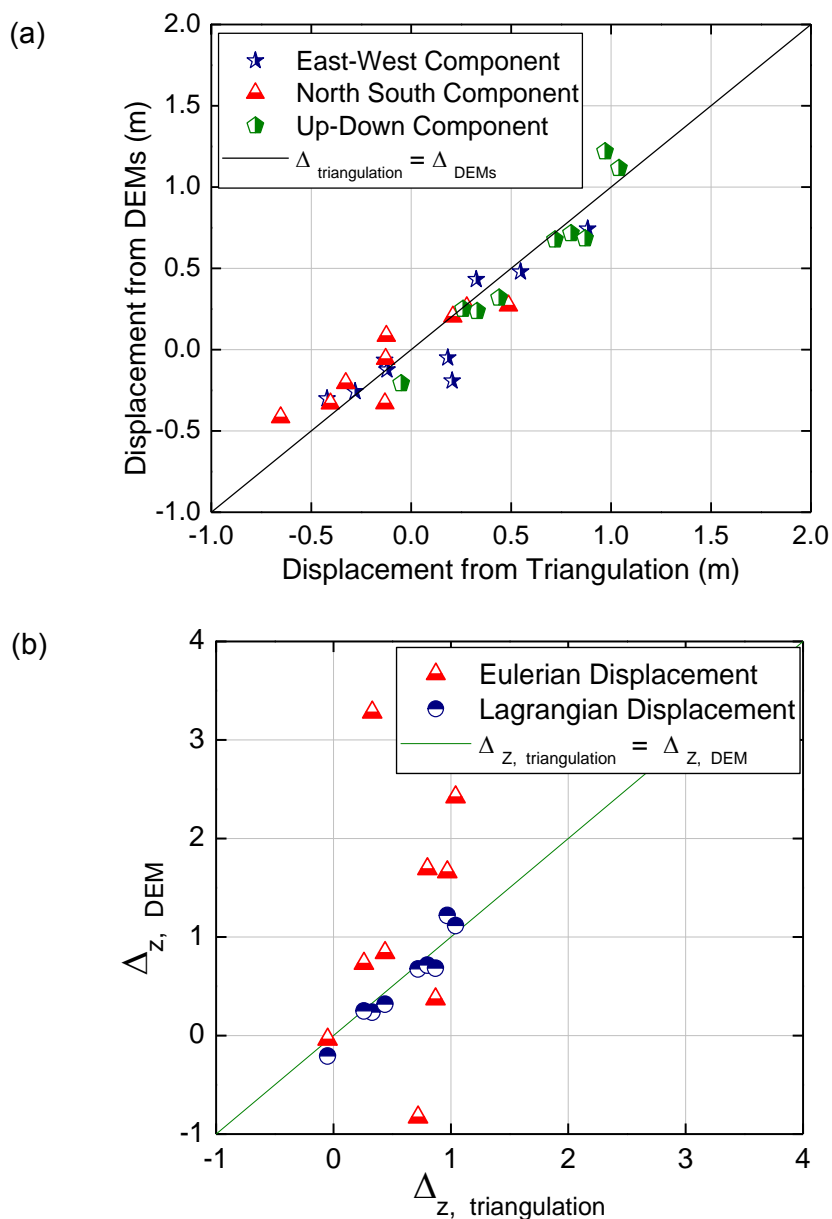
Figure 3.13: Verification of the process for obtaining Lagrangian ground displacement (a) Comparison of all the three components against the triangulation data (b) comparison of the vertical component of Lagrangian and Eulerian displacement against the triangulation data

3.4   SUMMARY

The impact of a large inland earthquake is serious not only because of its direct effect on our lives and properties but also because of its long-lasting problems for land conservation that can appear as landslides and debris flows. Therefore, study of terrain dynamics is vital to comprehend the possibility of hazards and to propose and apply rational rehabilitation tactics.
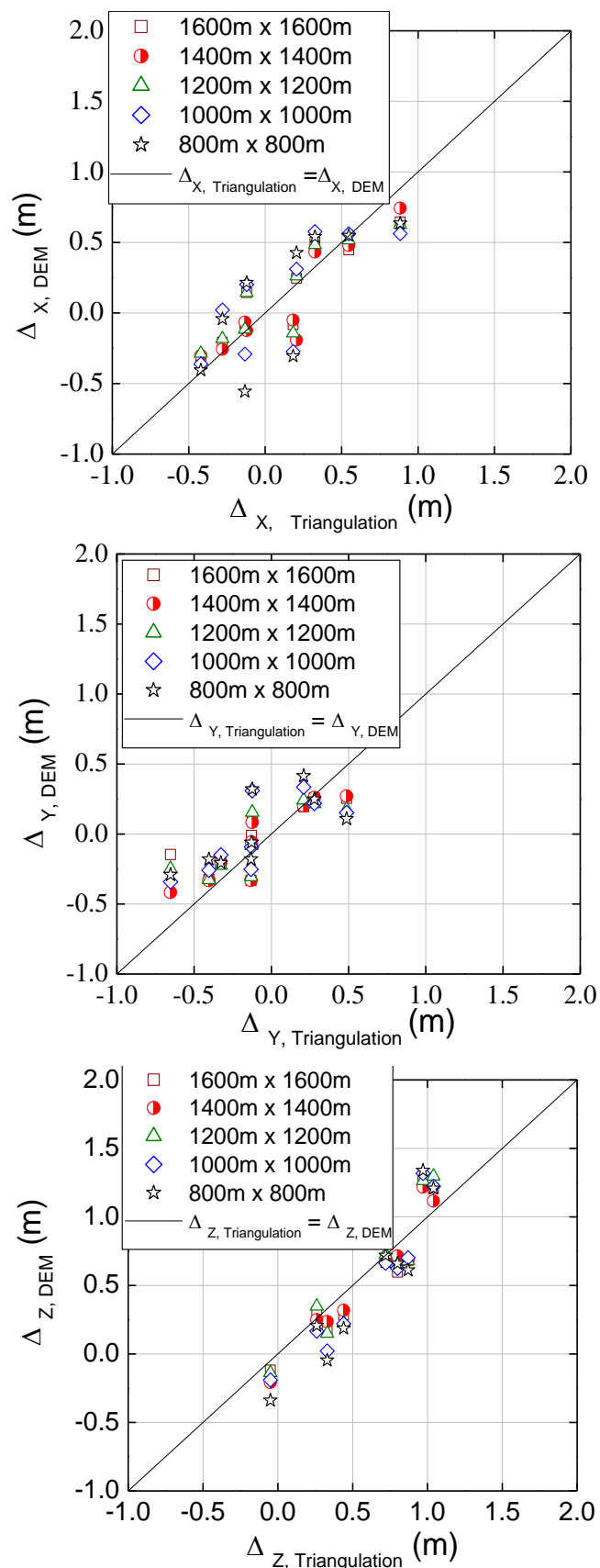
Figure 3.14: Sensitivity analysis for different sizes of the smoothening windows and comparison with the triangulation data for all the three components of Lagrangian ground displacements.

Due to the remoteness of disaster struck areas, usually high mountains, and due to its spatial extension, remote sensing is a cost efficient and more practical tool for monitoring terrain dynamics. Despite of the momentous development, remote sensing technology is still scarce to obtain history dependent Lagrangian ground displacements and in distinguishing deeper and shallower parts of crustal deformations. In this chapter, an improved method is proposed to extract three dimensional Lagrangian ground displacements from available set of pre- and post-seismic digital elevation models (DEMs) with the underlying assumption that tectonic displacements vary smoothly in space. The method is also capable of filtering and tracing out shallow soil displacements (landslides, manmade changes etc.) from the total tectonic displacements.

In the later half, practicality of the proposed method is evaluated by its application to the epicentral area of Mid-Niigata Prefecture Earthquake. Filtered shallow ground displacements have shown a remarkable correlation with the earthquake induced landslides. Calculated lateral and vertical Lagrangian ground displacement components were also found precisely concordant with the filed measurements and/or observations and have helped to develop a cause and effect relation between the co- and post-seismic devastations and Lagrangian ground displacements.

REFERENCES

1. Y. Fialko, D. Sandwell, M. Simons, and P. Rosen (2005), Three-dimensional deformation caused by the Bam, Iran, earthquake and the origin of shallow slip deficit, Nature, 435, doi:10.1038/nature03425, 295-299.

2. T. J. Wright, B. E. Parsons, and Z. Lu (2004). Toward mapping surface deformation in three dimensions using InSAR, Geophys. Res. Lett., 31, L01607, doi:10.1029/2003GL018827.

3. M. Tobita, M. Murakam, H. Nakagawa, H. Yarai, S. Fujiwara and P. A. Rosen (2001). 3D surface deformation of the 2000 Usu Eruption measured by matching of SAR images. Geophysical Research Letters, 28, 4291.

4. K. Konagai, T. Fujita, T. Ikeda, and S. Takatsu (2009). Tectonic deformation buildup in folded mountain terrains in the October 23, 2004, Mid-Niigata earthquake, Soil Dynamics and Earthquake Engineering, 29(2), 261-267.

5. K. Hikima and K. Koketsu (2005). Rupture processes of the 2004 Chuetsu (mid-Niigata prefecture) earthquake, Japan: A series of events in a complex fault system, Geophysical Research Letters Vol.32, L18303, 5.

6. K. H. Yoong and A. Okada (2005). Surface deformations associated with the October 2004 Mid-Niigata earthquake: Description and discussion, Earth Planets Space, 57, 1093–1102

7. JSCE Active folding Project Earthquake Damage in Active-Folding Areas: Creation of a comprehensive data archive and suggestions for its application to remedial measures for civil-infrastructure systems (2005-2007) Research and Development Program for Resolving Critical Issues, Special Coordination Funds for Promoting Science and Technology (2008) (Core research organization: JSCE, Leader: K. Konagai).

8. N. Oyagi, S. Uchiyama, and T. Inokuchi (2008). Map of Landslides Caused by the 2004 Niigata-ken Chuetsu (Mid Niigata) Earthquake (MJMA=6.8), Technical Note of the National Research Institute for Earth Science and Disaster Prevention, 317.

9. Yanagisawa, Y., Kobayashi, I., Takeuchi, K., Takeishi, M., Chihara, K. and Kato, H. (1986) Geology of the Ojiya District. Quadrangle Series Scale 1:50,000, Niigata (7), 50. *Geological Survey of Japan*.

10. Dooge, J.C.I. in (1992): Yen BC, editor. Channel wall resistance: Centennial of Manning's formula. Littleton, Colorado, Water Resources Publications.

11. National Research Institute for Earth Science and Disaster Prevention (NIED) and Japan Science and Technology Agency (2008) Landslide Map Database.
http://lsweb1.ess.bosai.go.jp/jisuberi/jisuberi_mini_Eng/jisuberi_top. htmlS.

12. National Institute of Earth Science and Disaster Prevention. (2004) Mid Niigata Earthquake. http://www.hrr.mlit.go.jp/saigai/H161023/1023_top.htmlS.

Chapter 4

4 Source Inversion Analysis

4.1   INTRODUCTION

Estimation of damage caused by an earthquake primarily demands strong ground motion records. Although there has been a significant development to record strong ground motions in the last few decades, seismograms have been often missing or very sparsely available, especially in developing countries. A deep insight into the earthquake focal mechanism and spatial and temporal distribution of slips on fault rupture planes is of core importance to understand/determine stains buildup up in soils and rocks within the earth crust, especially along the dislocated fault, and eventually to understand earthquake induced devastations.

Inversion of recorded seismograms to obtain fault mechanism and spatial and temporal rupture history of an earthquake is a common approach in seismology. Nevertheless, unavailability of the seismogram records frustrates all attempts to achieve the goal. The static ground displacement can be determined by comparing geodetic observations or satellite imageries at any time after the seismic event. Therefore, to determine the spatial distribution of slips on a fault rupture plane by inverting static ground displacement sought to be of wider application. Inversion of static ground surface displacements is as old as the introduction of elastic dislocation theory in seismology (e.g. (Maruyama, 1964 and Matsu'ura 1977a, 1977b), which quantitatively relates the fault slip distribution to the ground surface displacement. With the increased number of seismic disasters and development of the technology to precisely detect crustal deformations, inversion of geodetic data has been extensively used over the last few decades.

The geodetic data inversion problems are well developed for both the linear (e.g. Matsu'ura, 1977a, 1977b; Matsu'ura and Hasegawa, 1987; Matsu'ura and Iwasaki, 1980; Yabuki et al., 1992) and nonlinear (e.g. Miyashita et al., 1978; Ward and Barrientos, 1986; Barrientos, 1988) cases and have been used since then. However, use of fine resolution ground deformation data with shallow ground displacements (landslides, manmade changes etc.) filtered out, especially around the source area, needs to be emphasized and can give more

refined and reliable picture of spatial distribution of slips even on complex multi-segmental fault geometry. The concept of finer sample spacing in the near field as compared to far field is also used by Funning et al. (2005). When practical applications of the geodetic data inversion are discussed, particularly in developing countries, we must assume that the fault geometry is not always known. For linear geodetic inversion cases, fault model can be obtained from the crustal deformation pattern, distribution of aftershocks, and by minimization of the misfit between back synthesized ground displacements for the adopted fault model and observed ground displacements. Above all, however, the method is to be verified first under the limited number of uncertainties. Available with very fine resolution and precise Lagrangian displacements of the terrain (presented in Chapter 3) and the fault geometry estimated from dense seismometer networks, the area affected by Mid-Niigata Prefecture Earthquake is considered to be one of the most appropriate areas for this purpose. Once reliability and practicality is verified, it can be used for any other study area. This chapter encompasses linear geodetic inversion for Mid-Niigata Prefecture Earthquake and 2005 Kashmir Earthquake.

4.2   MATHEMATICAL FORMULATION

An insight of the fault rupturing process within the earth's crust is an imperative need for the fields of earthquake engineering and seismology. Response of the medium to a unit slip in the source region (Green's functions) relates surface displacements to the distribution of slip across the fault rupture plane based on elastic dislocation theory. Therefore, an inversion problem can be set up to retrieve static image of slip distribution from the observed geodetic data.

According to Aki and Richard (1980) and referring to Figure 4.1, the generalized observation equation of the static co-seismic surface displacement at position (x, y) due to a displacement discontinuity at position (*x', y'*) across the faulting surface, Σ, is

$$u_n(x,y) = \int_{\Sigma} S_p(x',y') * G_{np}(x,y;x',y')d\Sigma \qquad (4.1)$$

G_{np} in equation (4.1) is Green's function for the nth component of ground displacement at (x, y) to a point dislocation in p-direction at (x', y') across the fault surface, Σ, $u_n(x,y)$ is the nth component of static ground displacement and $S_p(x',y')$ is the fault slip in p-direction

(Figure 4.1). With N number of sub-faults, the observation equation can be split into the directional components and in strike and dip directions as
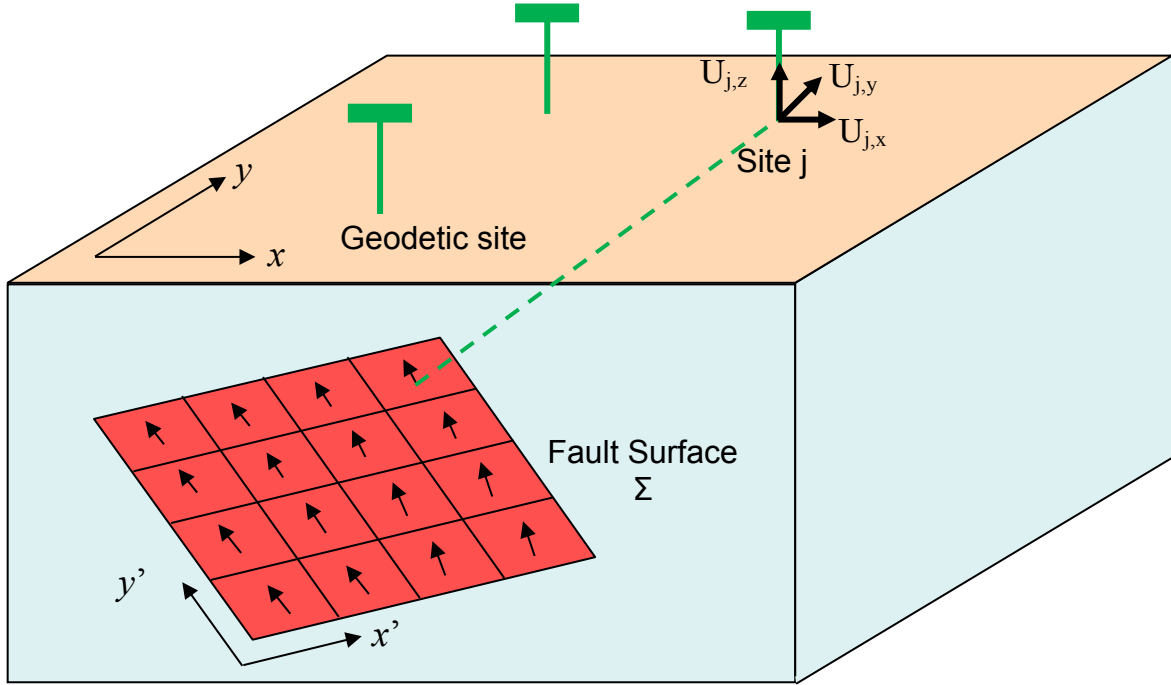
Figure 4.1: Schematic illustration of the inversion scheme to obtain fault rupture from observed/pre-determined static ground displacements.

$$u_{j,x} = \sum_{I=1}^{N} [G_{ij,x}^{ss} S_{ij}^{ss} + G_{ij,x}^{ds} S_{ij}^{ds}]$$

$$u_{j,y} = \sum_{I=1}^{N} [G_{ij,y}^{ss} S_{ij}^{ss} + G_{ij,y}^{ds} S_{ij}^{ds}] \tag{4.2}$$

$$u_{j,z} = \sum_{I=1}^{N} [G_{ij,z}^{ss} S_{ij}^{ss} + G_{ij,z}^{ds} S_{ij}^{ds}]$$

The partitioned system of equations (eq. 4.2) can be represented in the matrix form as

$$[u] = [G_{ss} \quad G_{ds}] \begin{bmatrix} S_{ss} \\ S_{ds} \end{bmatrix} \tag{4.3}$$

4.2.1 Calculation of Green's Function

Green's functions are calculated by discrete-wavenumber method (Bouchon, 1981), which is based on exact discretization of the wave field emitted by the source. A single source is

replaced by and equivalent source array whose radiation, because of wave interference, may be expressed in discretized form (Bouchon 1979, 1980; Bouchon and Aki, 1977). According to Bouchon (1981), the compressional displacement potential of elastic wave field radiated by pulsating point source in an infinite homogeneous space is given by

$$\emptyset(R;\omega) = \frac{e^{i\omega(t-\frac{R}{\alpha})}}{R} \tag{4.4}$$

Where, R is the distance between source and observation point, α is the compressional wave velocity, ω is angular frequency and t is time.

For source located at origin, the above equation can be expressed in cylindrical coordinates by Sommerfeld integral as;

$$\emptyset(r,z;\omega) = -ie^{i\omega t}\int_0^\infty \frac{k}{v}J_0(kr)\,e^{-ivz}dk \tag{4.5}$$

Where

$$v = \sqrt{k_\alpha{}^2 - k^2}, \qquad \text{Im}(v) < 0 \tag{4.6}$$

$$k_\alpha = \omega/a \tag{4.7}$$

Sommerfeld integral, outside the origin, is a particular solution of the wave equation

$$\frac{\partial^2\varphi}{\partial r^2} + \frac{1}{r}\frac{\partial\varphi}{\partial r} + \frac{1}{r^2}\frac{\partial^2\varphi}{\partial\theta^2} + \frac{\partial^2\varphi}{\partial z^2} - \frac{1}{\alpha^2}\frac{\partial^2\varphi}{\partial t^2} = 0 \tag{4.8}$$

Considering a set of sources uniformly and continuously distributed along the circumference of a circle of radius L , centered at origin, with an additional point source located at the center, the final displacement potential is given as;

$$\emptyset(r,z;\omega) = -\frac{i\pi}{L}\sum_{n=0}^\infty \varepsilon_n \frac{k_n}{v_n}J_0(k_n r)\,e^{-iv_n z} \tag{4.9}$$

Where

$$v_n = \sqrt{k_\alpha{}^2 - k_n{}^2}, \qquad \text{Im}(v_n) < 0 \tag{4.10}$$

$$k_n = 2n\pi/L \tag{4.11}$$

Reflection-transmission method (Kennett and Kerry, 1979) is used to obtain solution for a laterally homogenous stratified elastic half space.

4.2.2   Smoothing Constraint

Having sufficient number of observations, the observed system of equations (eq. 4.3) is over-determined. However, the solution demands the stabilization techniques due to underdetermined model parameters. A smoothing constraint is assigned in such a way that the spatial distribution of the slips has a gradual/smooth variation in space. The slip can be smoothened by minimizing the rate of change of slip i.e. curvature of slip. Curvature is quantified by Laplacian operator, given as;

$$\nabla^2 = \frac{\partial^2}{\partial x^2} + \frac{\partial^2}{\partial y^2} + \frac{\partial^2}{\partial z^2} \tag{4.12}$$

Following finite difference method, differential of any function P(x) is given as;

$$\frac{\partial P(x)}{\partial x} = \lim_{\Delta x=0} \left[\frac{P(x + \Delta x) - P(x)}{\Delta x} \right] \tag{4.13}$$

For a finite and small Δx, the limit can be dropped. i.e.,

$$\frac{\partial P(x)}{\partial x} = \frac{P(x + \Delta x) - P(x)}{\Delta x} \tag{4.14}$$

Differentiating once again, the second partial derivative of P(x) is given as

$$\frac{\partial^2 P(x)}{\partial x^2} = \frac{P(x + \Delta x) - 2P(x) + P(x - \Delta x)}{\Delta x^2} \tag{4.15}$$

Therefore, referring to Figure 4.2, the curvature of slip in both x and y directions is given as

$$L_{i,j} = \frac{S_{i-1,j} - 2S_{i,j} + S_{i+1,j}}{\Delta x^2} + \frac{S_{i,j-1} - 2S_{i,j} + S_{i,j+1}}{\Delta y^2} \tag{4.16}$$
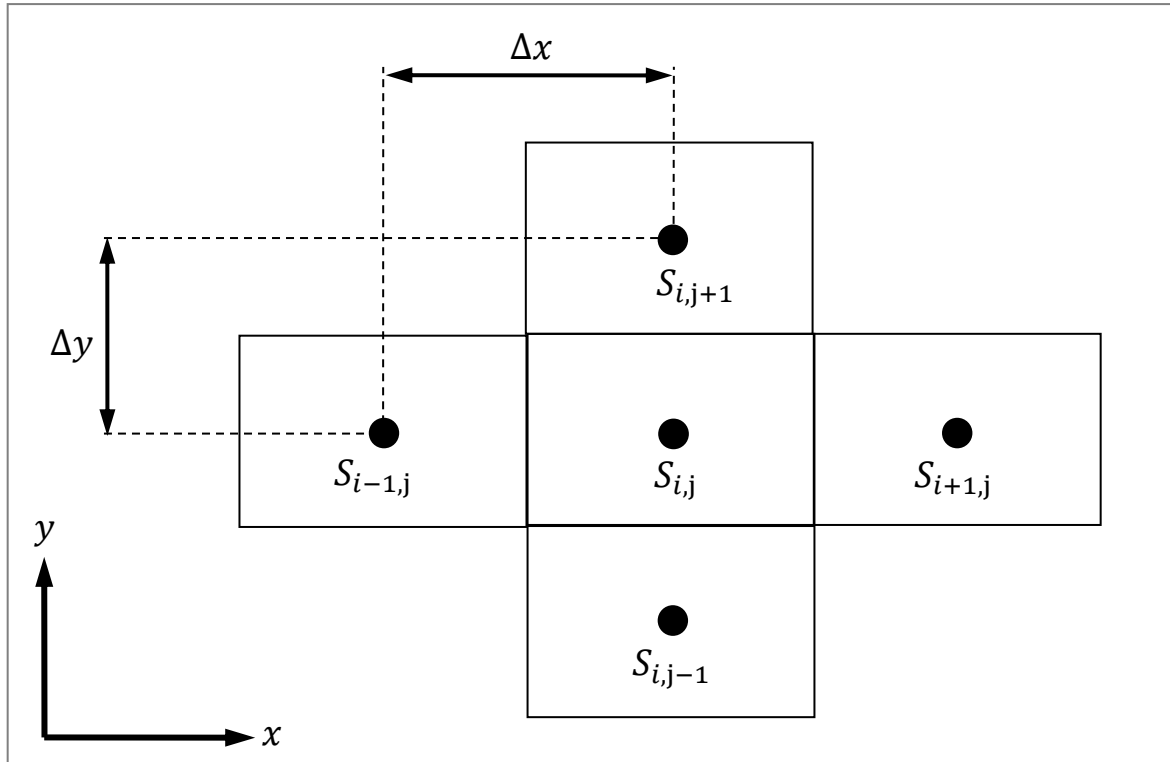
Figure 4.2: Schematic illustration for spatial smoothing of variable slips, both along strike and dip directions.

By adding the smoothing constraint, the original equation (eq. 4.3) transfers to a system of coupled equations as

$$
\begin{bmatrix} u \\ 0 \\ 0 \end{bmatrix} = \begin{bmatrix} G_{ss} & G_{ds} \\ \lambda L & 0 \\ 0 & \lambda L \end{bmatrix} \begin{bmatrix} S_{ss} \\ S_{ds} \end{bmatrix}
\tag{4.17}
$$

where λ is a scalar factor to tune the extent of smoothing. $\lambda = 0$ gives no smoothing effect. The degree of smoothing increases with the increasing value of λ. The inversion solution highly depends on the strength of smoothing constraint. The moment release distribution, however, is too complicated because of over-interpretation of the data, and the solution is unstable due to noise in the data and/or synthetic Green's functions.

A non-negative constraint is assigned by limiting the rake angle variation to suppress destructive interference between adjacent sub-faults. The resulting non-negative least square problem is solved by using the routine NNLS of Lawson and Hanson (Lawson and Hanson, 1974)

4.2.3   Optimization of Smoothing

Distribution of the slips on fault rupture planes is highly sensitive to the adopted smoothing constraint. Minimization of misfit between back synthesized and observed waveforms, and minimum seismic moment criterion have also been used by different authors for optimizations of the smoothing. In this study, an optimized value of the smoothing constraint is determined by Akaike's Bayesian Information Criterion (ABIC) (Akaike, 1980).

4.3   APPLICATION TO MID-NIIGATA PREFECTURE EARTHQUAKE

4.3.1   Fault Model and Parameters

The fault geometry for this earthquake was really complex such that three aftershocks with JMA magnitudes of 6.0 or greater occurred in rapid sequence. Different fault geometries and mechanisms have been proposed by different researchers: a 42km x 24km reverse fault dipping to the northwest (Honda et al., 2005), a multi-segment fault model proposed by Hikima (Hikima and Kokettsu, 2005) with five fault planes corresponding to the main shock and the following four largest aftershocks with magnitude larger than 6. In the current study, Hikima's fault model is adopted excluding segment "C" (Figures 4.3 and 4.4). This segment showed a minimum slip in Hikima's analysis and also the distribution of aftershocks doesn't make a clear pattern for this segment. For spatial discretization, each fault segment is divided into sub-faults having a size of 2km x 2km. The rake angles were allowed to vary within 45° centered at 93°, which is the rake angle of the moment tensor solution of F-net. The summary of the adopted fault parameters is presented in Table 4.1 and Figure 4.4.

Table 4.1: Summary of the fault parameters for Mid-Niigata Prefecture Earthquake

Rupture Plane	Length (km)	Width (km)	Strike (deg.)	Dip (deg.)	Depth of hypocenter (km)	Sub-faults
A	24	16	216	53	9.0	12 x 8
B	8	8	20	34	7.0	4 x 4
D	20	12	216	55	12.0	10 x 6
E	8	8	39	29	11.5	4 x 4
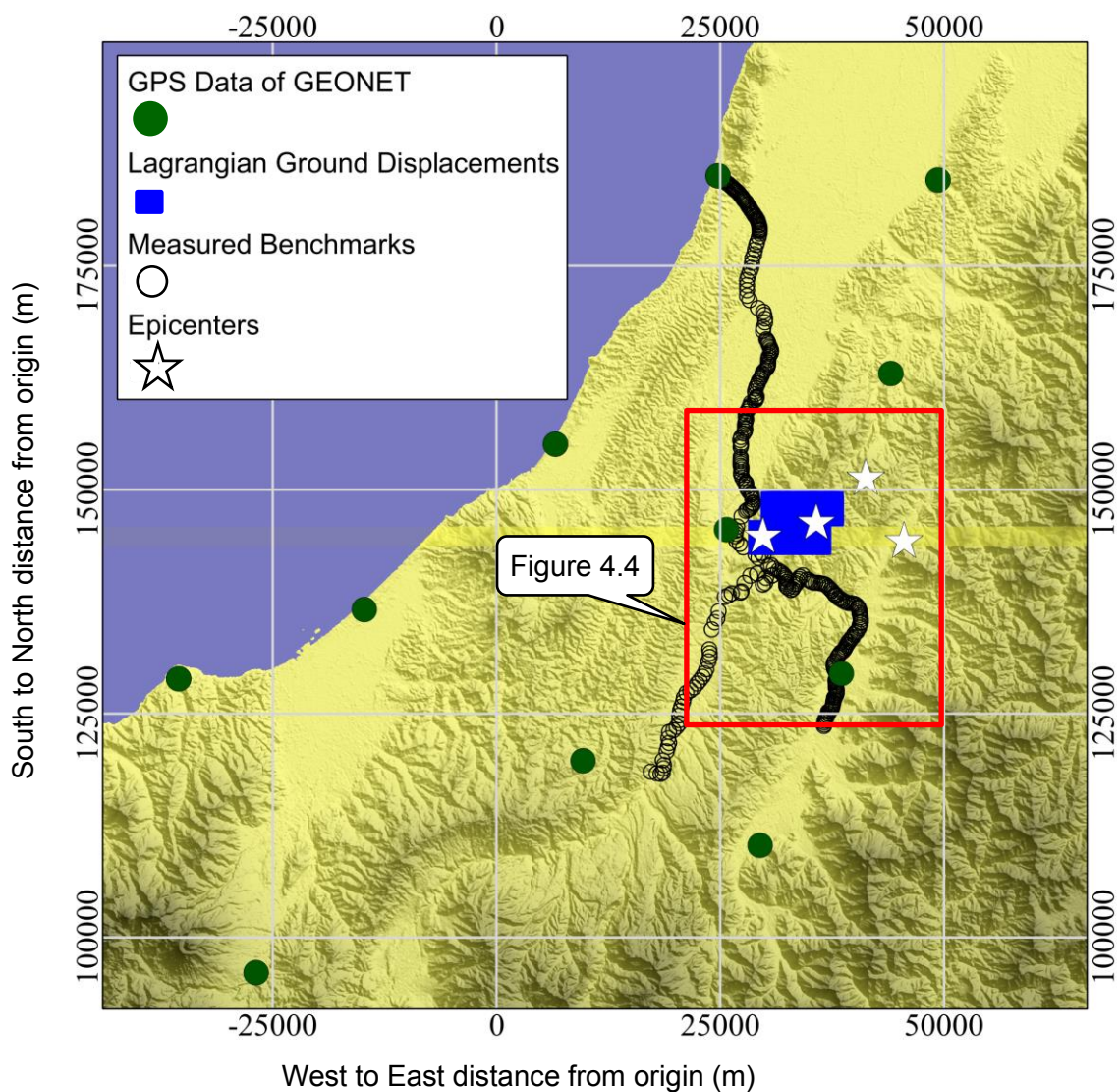
Figure 4.3: Layout map showing the position of ground surface displacements along with the epicenters of major events in Mid-Niigata Prefecture Earthquake. Topographical mapping is on the JGD2000/ Japan Plane Rectangular Coordinate System VIII.
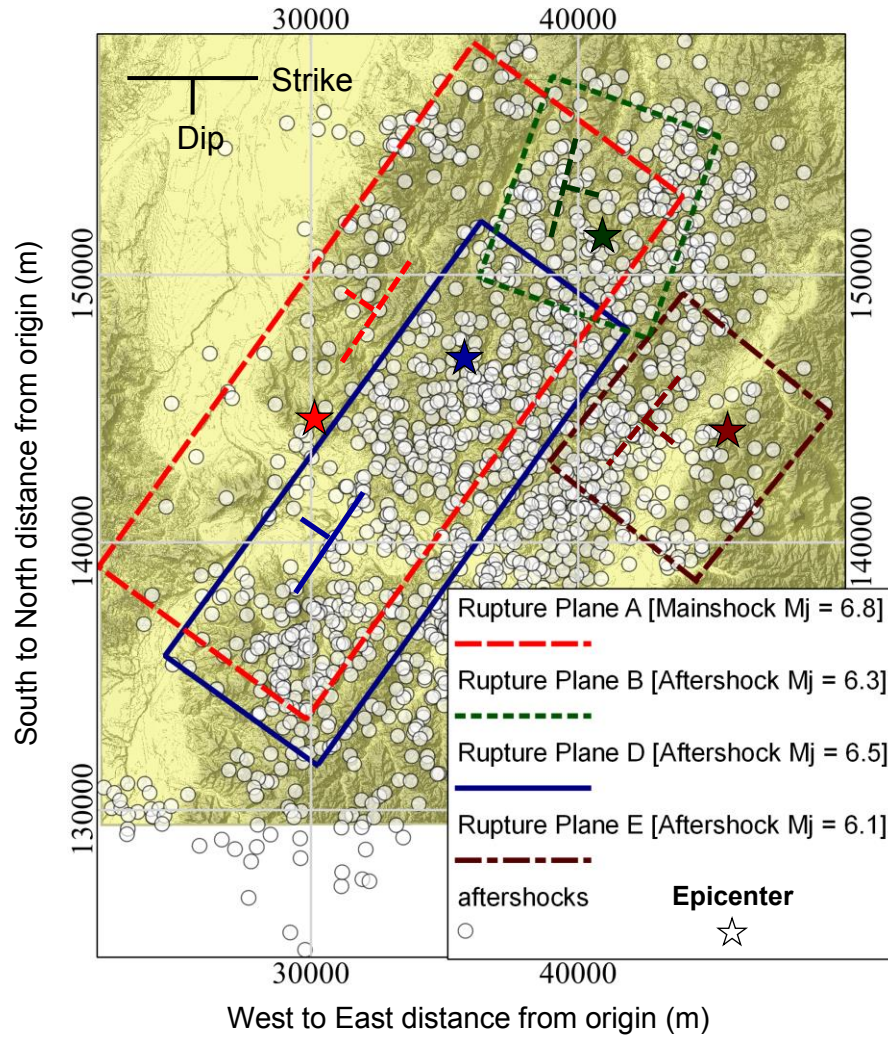
Figure 4.4: Aftershocks distribution along with surface projection of the rupture planes for a multi-segment fault model. Colored stars are the hypocenters of seismic events corresponding to each fault plane. Detailed parameters of each all four rupture planes are presented in Table 4.1. Topographical mapping is on the JGD2000/ Japan Plane Rectangular Coordinate System VIII

4.3.2.   Earth Structure

In order to obtain appropriate Green's functions, a laterally homogeneous stratified media, overlaying a half-space, was considered. Material properties of each layer (material density, ρ and two lam's constants λ and μ) are determined from the representative velocity structure of the source region (shown in Figure 4.5), obtained by combining bore hole data logging, geological information and seismic exploration.
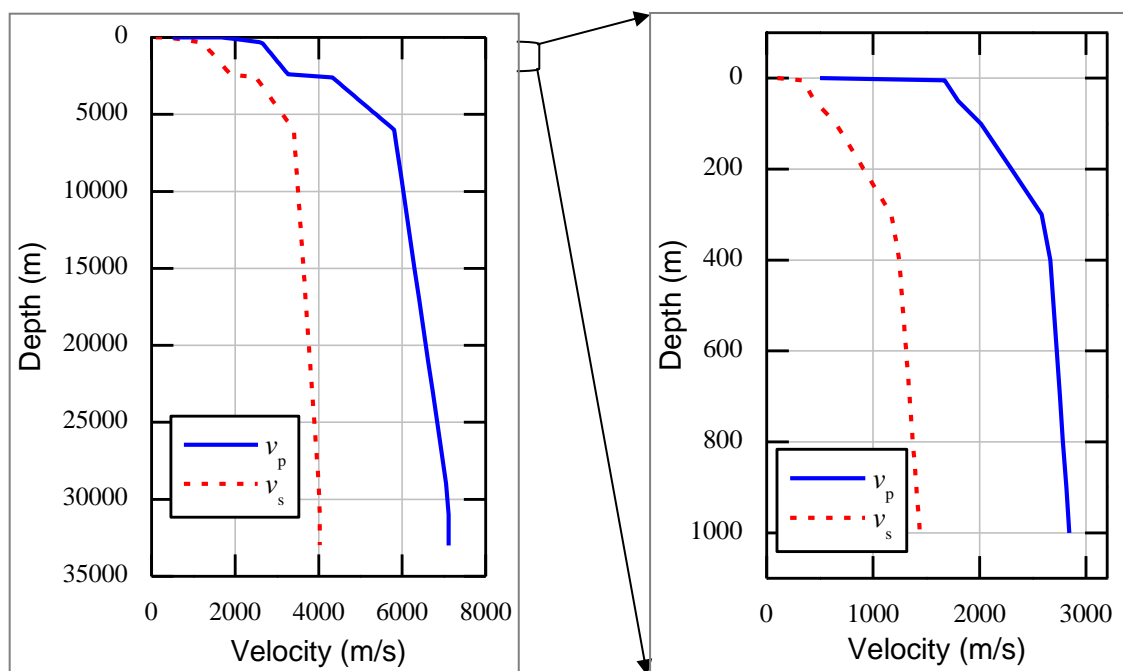
Figure 4.5: Velocity structure model to calculate Green's function. v_p and v_s are the primary and secondary wave velocities, respectively (Honda et al., 2005).

4.3.3.　　Slip Distributions

Since the area with known surface tectonic displacements is much smaller compared to the size of ruptured area, static GPS observations of GEONET and the benchmarks measurements along Shinano and Uono Rivers (shown in Figure 4.3) were also considered. Figure 4.6 shows surface projection of the slip obtained by the inversion analysis for an optimized value of the smoothing coefficient (λ value corresponding to the minimum value of ABIC, Figure 4.7) and all four rupture planes have shown almost a dip-slip pattern. For the main shock of M6.8 at 17:56 (rupture plane A, Figure 4.4), there are two asperities. The larger one is distributed around the hypocenter and a maximum slip of about 1.75m is reached. For the largest aftershock of M6.5 at 18:34 (rupture plane D, Figure 4.4), significant slips are mainly distributed around its hypocenter, and extend to its south and southwest. The maximum simulated value is 1.04m. Rupture plane B (after shock of M6.3) has a maximum slip of 0.56m around its hypocenter and dies off towards the ground surface; while, slips are all smaller than 10cm on rupture plane E (aftershock of M6.1).

Slip distribution pattern and magnitude are in close agreement with total slip distribution obtained by inversion of waveform records (Hikima and Koketsu, 2005).
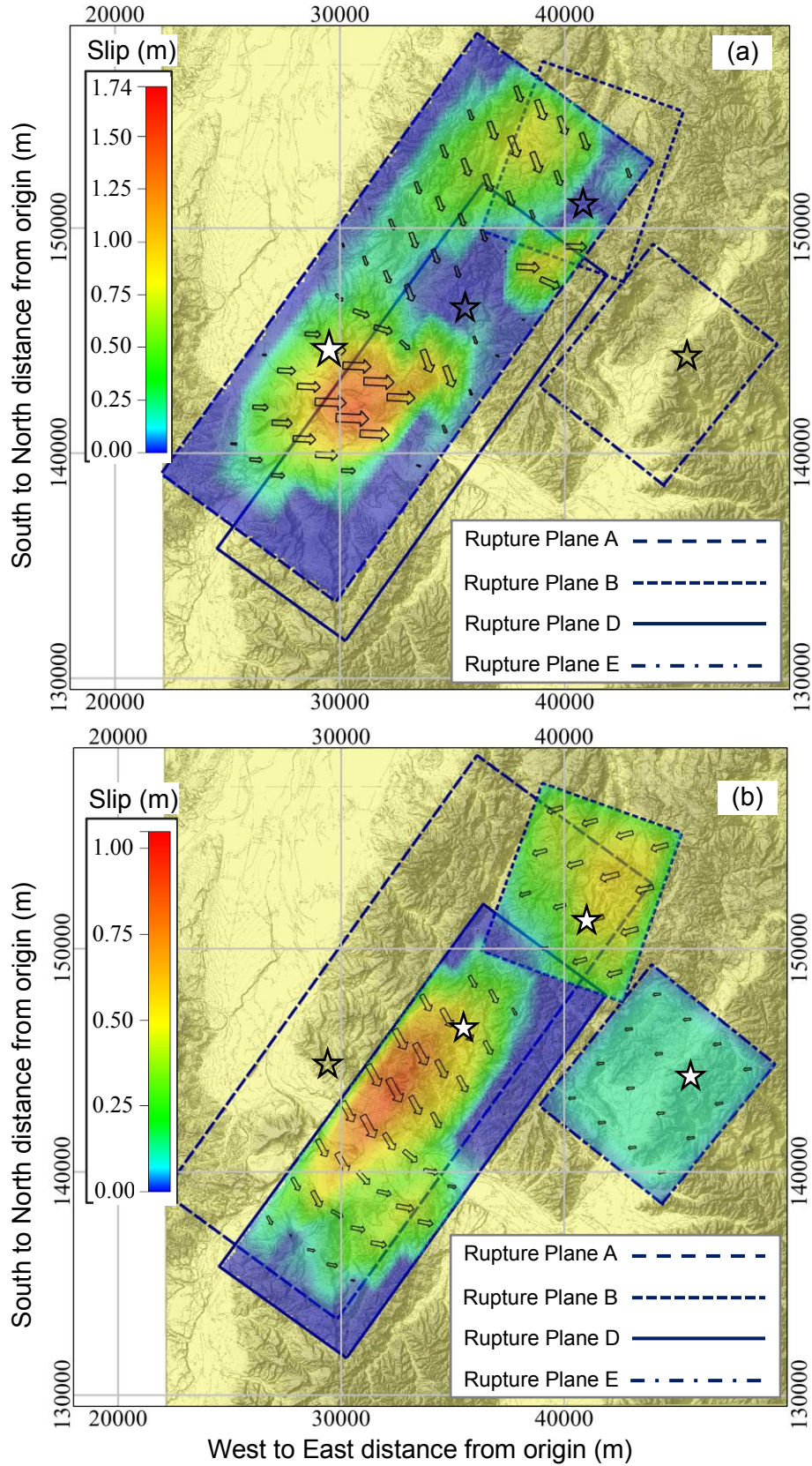
Figure 4.6: Surface projection of the fault slip distribution for a) Rupture plane A (the main shock), b) Rupture planes B, D and E (three largeest aftershocks). All rupture planes are defined in Figure 4.4 and Table 4.1. The vectors are to show the direction of slip. Topographical mapping is on JGD2000/ Japan Plane Rectangular Coordinate System VIII.
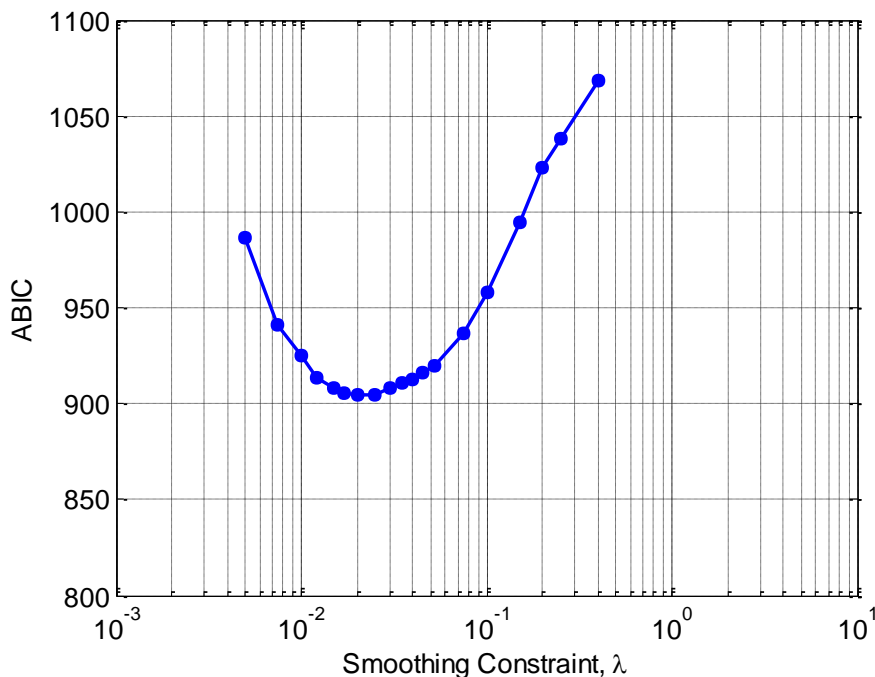
Figure 4.7: Selection of the optimized value of smoothing constraint, λ, using Akaike's Bayesian Information Criterion (ABIC)

4.3.4.   Interference Test and Effect of Data Resolution

Though the obtained slip distribution is close to that of the obtained results by inverting the seismogram records (Hikima and Koketsu, 2005), which ensures practicality of inverting static ground displacements, inverting the total static displacements may not always distinguish the slips on each segment of a complex multi-segment fault rupture sequence. To examine the extent of interference, the ground displacement components are back synthesized (Figure 4.8) using only the fault slips of rupture plane "A" (main shock). While carrying out the inversion analysis with the back-synthesized ground displacements for the complete rupture sequence, small amount of slips were observed for the other rupture planes (rupture planes B, D and E) (Figure 4.9). However, the magnitudes of slips across the other rupture planes are small enough to ensure tolerable extent of interference.

Figure 4.10 shows the surface projection of the fault slip obtained by inverting only the GPS and benchmark datasets. It is quite clear from the figure that without considering the fine resolution ground displacement data above the source region (presented in Chapter 3), a refined slip pattern cannot be obtained. GPS sites are sparsely deployed (at an interval of 20 to 30km) while the benchmarks are measured only along the Shinano and Uono Rivers and it remains difficult to obtain high quality co- or post-seismic slip distribution, especially for small to moderate earthquakes. For those mentioned above, the method will be promising when a dataset of tectonic displacements covers much wider area.
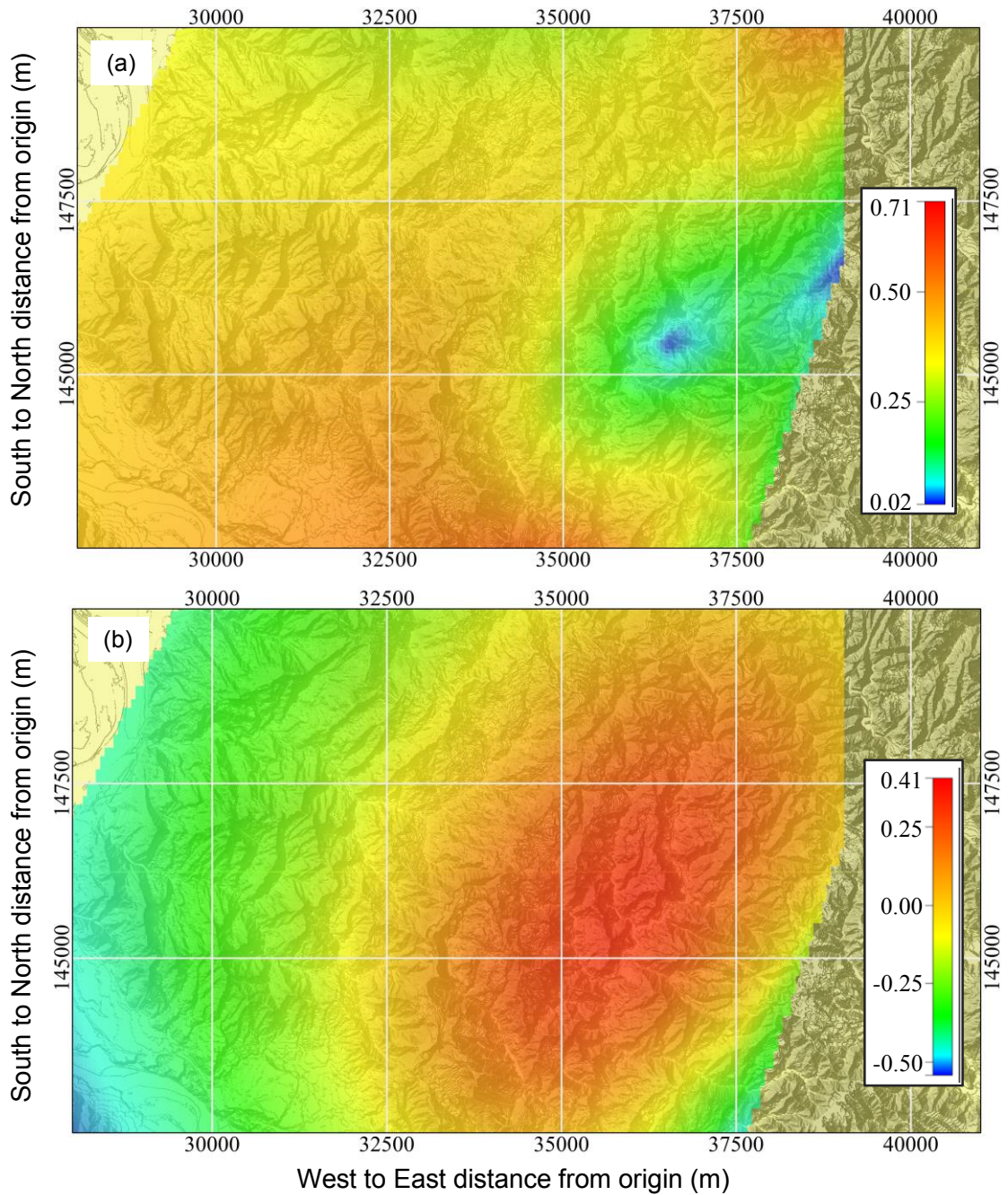
Figure 4.8: Synthesized ground displacement using the fault slip of Segment A, shown in figure 4.7a. a) Lateral component of displacement b) Vertical component of displacement. Topographical mapping is on the JGD2000/ Japan Plane Rectangular Coordinate System VIII.
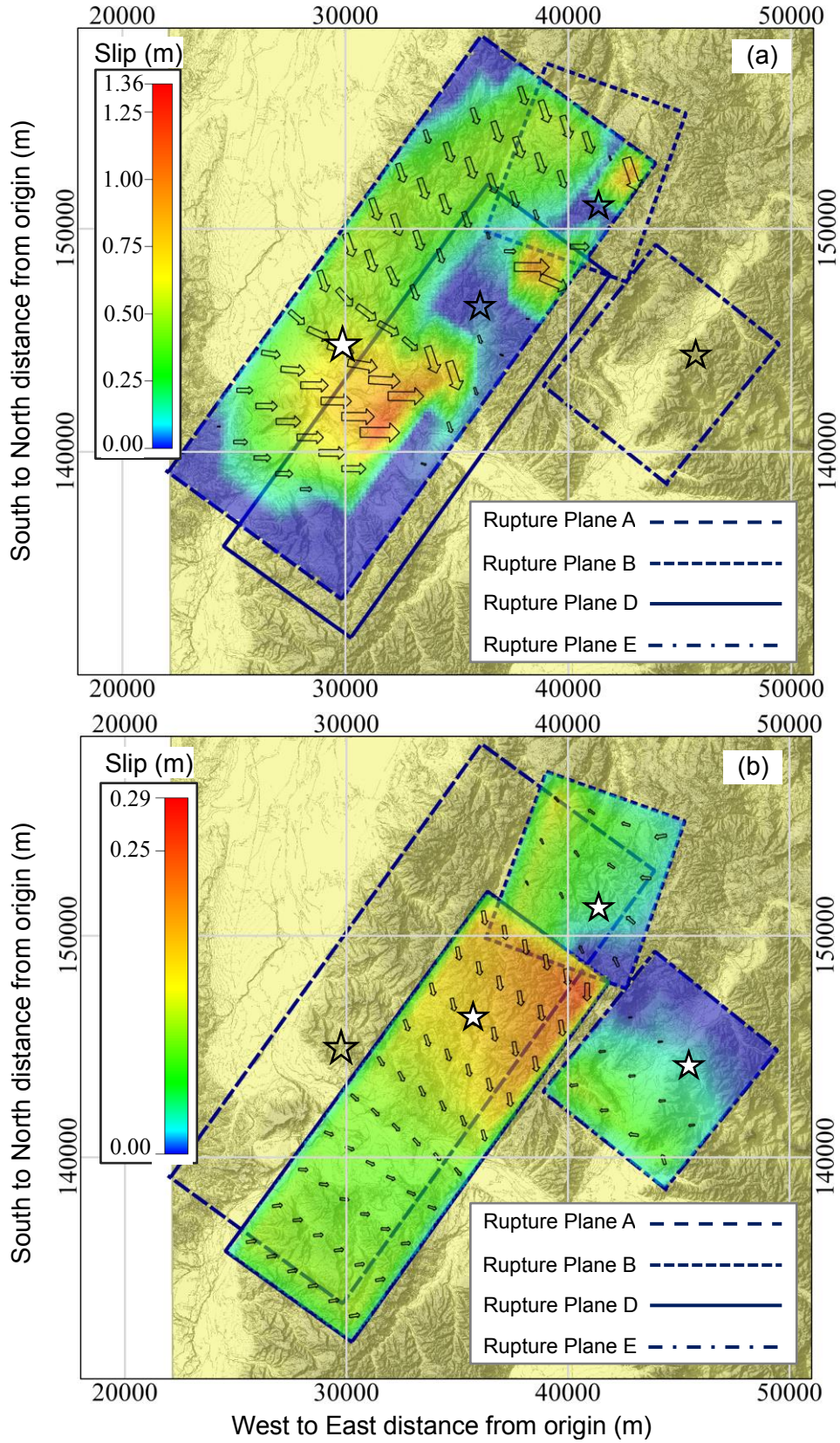
Figure 4.9: Surface projection of the fault slip distribution obtained by inverting the synthesized ground displacement of figure 4.8 for (a) rupture plane A (main shock) and (b) rupture planes B, D and E (three large aftershocks). Topographical mapping is on JGD2000/ Japan Plane Rectangular Coordinate System VIII.
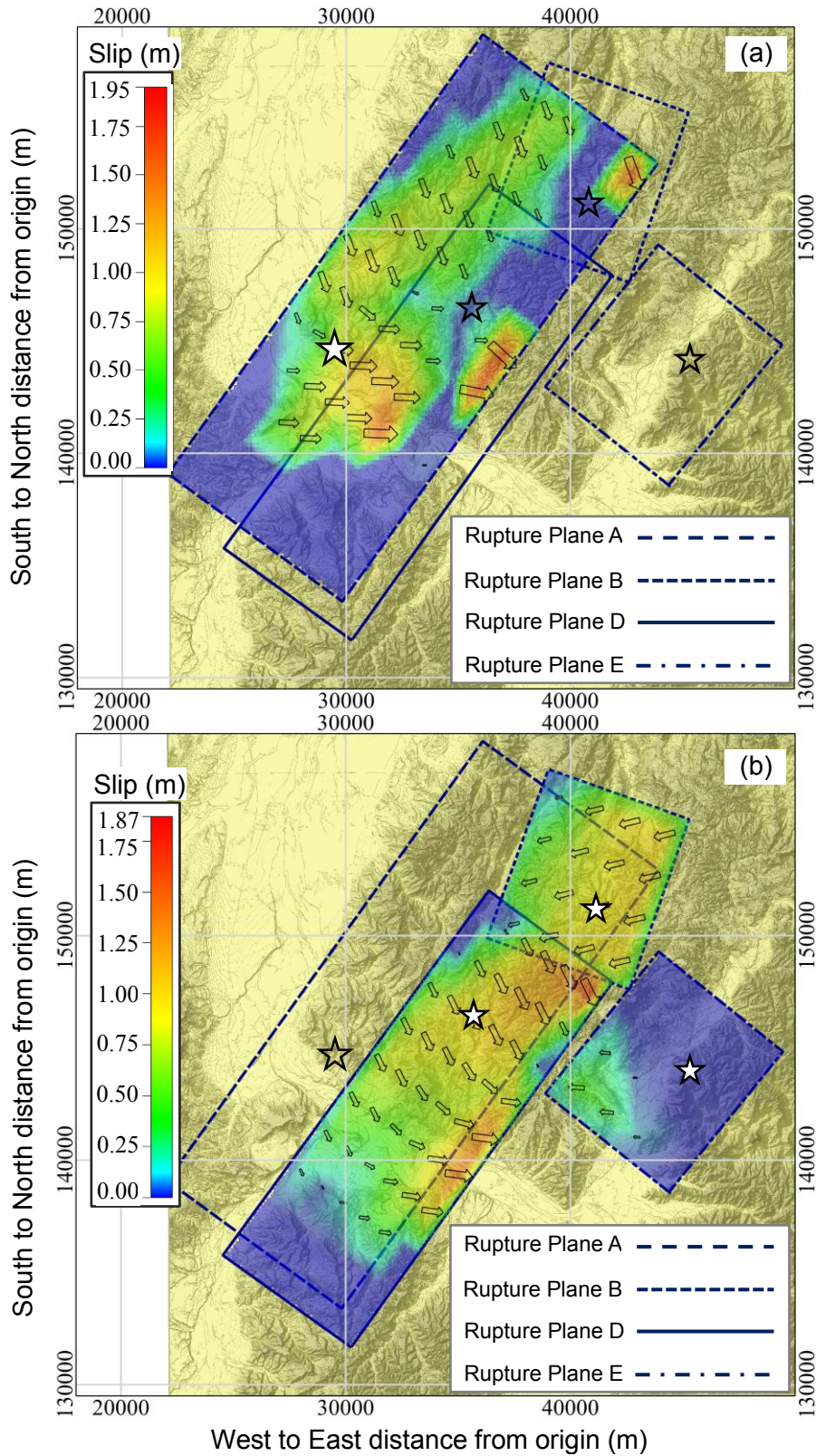
Figure 4.10: Surface projection of the fault slip distribution obtained by inverting the GPS and benchmark measurement data for (a) rupture plane A (main shock) and (b) rupture planes B, D and E (three large aftershocks). It's elaborated that without including the detailed ground deformation data above the source area, a refined slip pattern cannot be obtained. Topographical mapping is on JGD2000/ Japan Plane Rectangular Coordinate System VIII.

4.4   APPLICATION TO 2005 KASHMIR EARTHQUAKE

4.4.1   Crustal Deformations

Since the occurrence of 2005 Kashmir Earthquake, different authors have tried to extract three dimensional crustal deformation associated with this earthquake (e.g. Fujiwara et al., 2005; Pathier et al., 2006 etc.), adopting different data sources and analysis techniques. All of them have revealed a northwest-southeast trending wider belt of large crustal deformation having a length of over 75 km. Filtered lateral and vertical components of ground displacement obtained by Fujiwara et al. (2006) are shown in Figure 4.11 along with the topographical map and surface trace of the ruptured Balakot-Bagh fault.
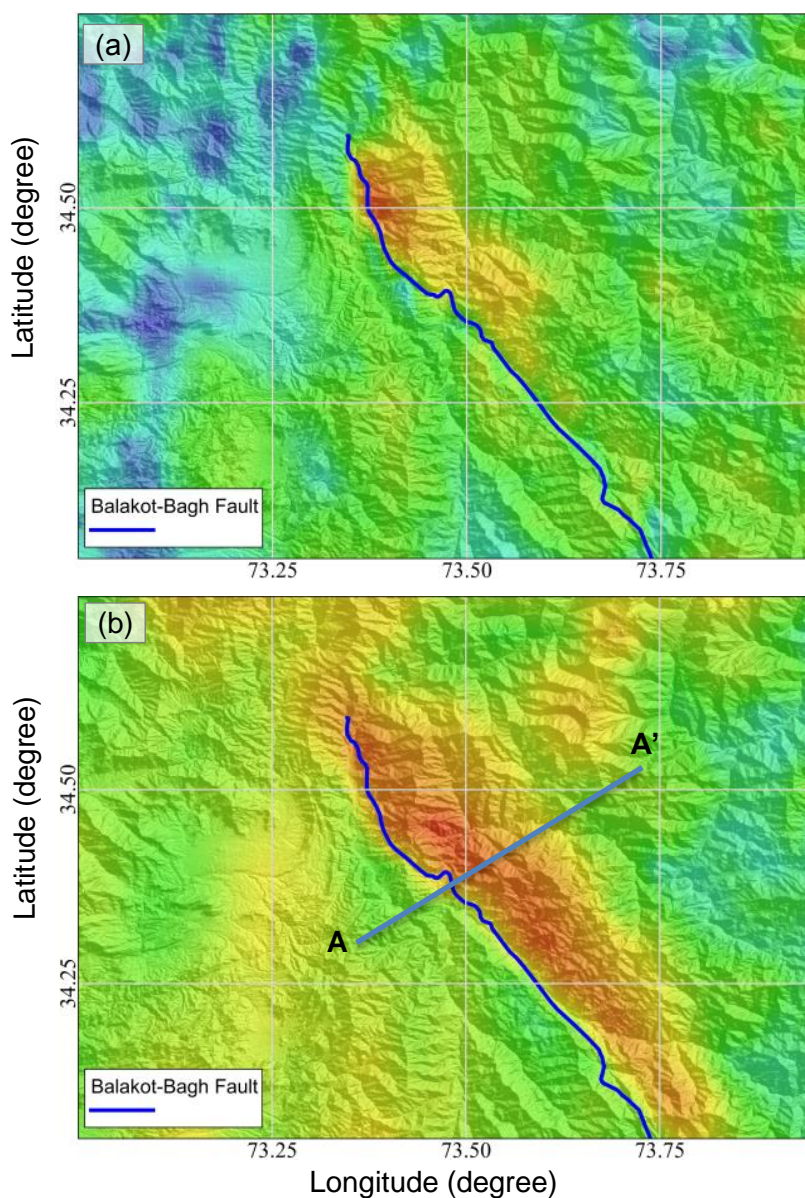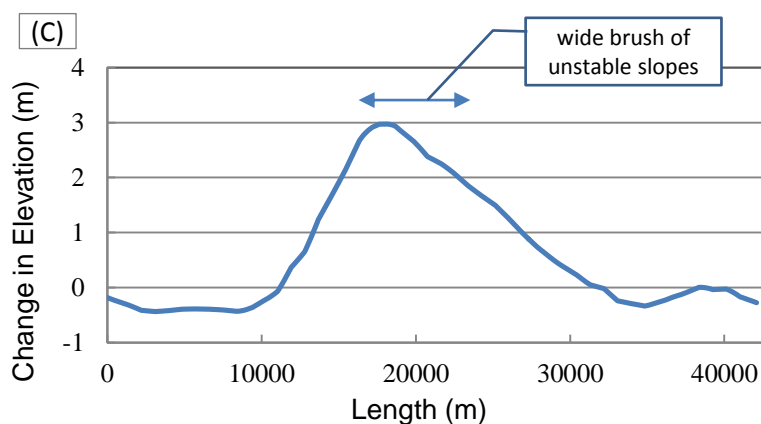
Figure 4.11: Three dimensional crustal deformations extracted from the SAR data, overlaid the terrain map (a) Lateral component (b) Vertical component (c) Section A-A' to show vertical dislocation and wide brush of unstable and crushed slopes (after Fujiwara et al. 2006).

The earthquake devastated area has a rugged mountainous terrain which is not easy to be assessed and, therefore, the crustal deformation data can be used to gauge the extent of fault and type of displacement. The largest ground displacement was detected to the north of Muzaffarabad city, where the vertical component reached about 3.5 meters while the lateral component is 5.0 meters. Although vertical dislocation was not clearly observable due to blind reverse separation of the fault, a similar magnitude of deformation and highly concentrated landslides and slope failures were observed by the authors during their repeated filed surveys (Figure 4.12).

Figure 4.12 (a) Photograph showing fault rupture, slope failures and landslides behind Muzaffarabad city (b) closed up view to elaborate fault movement pattern and extent of wide brush being disturbed by the fault movement.

4.4.2   Fault Model and Parameters

In the age of significantly developed technology, various techniques are available to obtain earthquake mechanism and detailed source parameters soon after the occurrence of the seismic event. However, adoption of the different techniques and data sources results in a wide variation of source parameters. For example, the strike, dip and rake angles for Kashmir earthquake were N133E, 40° and 123°, respectively, according to Harvard CMT solution (http://www.seismology.harvard.edu/CMTsearch) while N133E, 29° and 140° according to USGS solution (http://neic.usgs.gov). Since USGS solution is rooted in modeling body waves, the dip angle is considered to be more accurate (for shallow hypocenters) as compared to Harvard CMT solution, where they have modeled long period surface waves.

Different fault models have been proposed by different authors to elucidate the earthquake mechanism more precisely (e.g. Pathier et al., 2006; Avouac et al., 2006; Wang et al., 2007 etc., Table 4.2). Most of them have used a homogenous half-space as earth structure, which might have over simplified the actual ground condition. In this study, the authors have considered a fault rupture plan having dimensions of 90km x 30km in strike and dip directions, respectively, which is extracted from the crustal deformations pattern and aftershocks distribution. The strike and dip angles were considered as 320° and 29°, respectively; while the rake angle was allowed to vary within 45° from its center (123°), which is the rake angle of Harvard CMT solution. For spatial discretization, the fault plane is divided into 3km x 3km sub-faults. The detailed fault geometry and parameters are shown in Figure 4.13 and table 4.3.

Table 4.2: Source and fault model parameters for Kashmir Earthquake from literature

	Source	Strike (degree)	Dip (degree)	Rake (degree)	Length (km)	Width (km	Depth of Hypocenter (km)
1	Harvard CMT solution	N133E	40	123	--	--	--
2	USGS	N133E	29	140	--	--	--
3	Avouac et al., 2006	320	29	--	75	30	11
4	Pathier et al., 2006	321.5	31.5	--	100	30	11.5
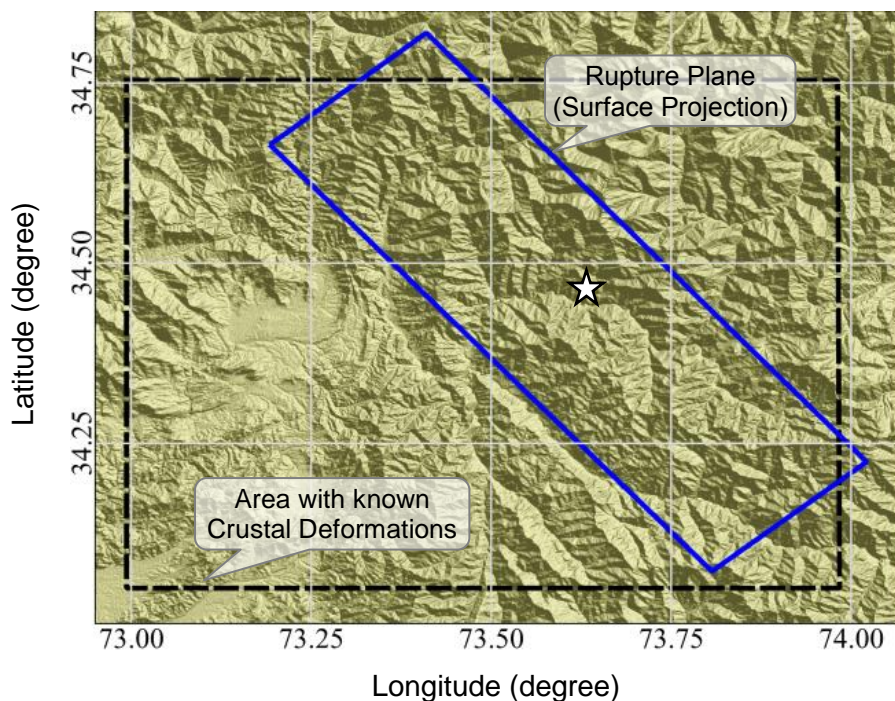
Figure 4.13: Layout map showing the surface projection of fault rupture plane and position of available crustal deformation for 2005 Kashmir Earthquake. The star shows the location of hypocenter.

Table 4.3: Summary of fault model parameters used for source inversion

Length (km)	Width (km)	Strike (deg.)	Dip (deg.)	Depth (km)	Sub-faults
90	30	320	29	12	30x10

4.4.3   Earth Structure

For calculation of green function, a laterally homogenous layered half space was considered, whose details are obtained by combining the sediment accumulation information (compiled by Laske et al. and available in the form of a free software CRUST2.0) and bore hole data for the top 100 meters of the crust (Figure 4.14).

4.4.4   Slip Distributions

Figure 4.15 shows the surface projection of the fault slip distribution for optimum value of smoothing constraint (λ). The slip pattern confirms a thrust fault type with the largest simulated value of slip reaching about 7.6 meters. The largest asperity of slip is located to the north of Muzaffarabad city, same location where the largest crustal deformation has

been detected. Slip vectors larger than 3 meters are concentrated in the shallower depth (less than 7 km) which would be taken as one of the most prominent causes for catastrophic devastation in the near field. By superimposing the fault slip distribution vectors on the crustal deformation map, it can be found that the slip vectors close to ground surface are very well consistent with the crustal deformations (Figure 4.16), in terms of magnitude as well as direction.
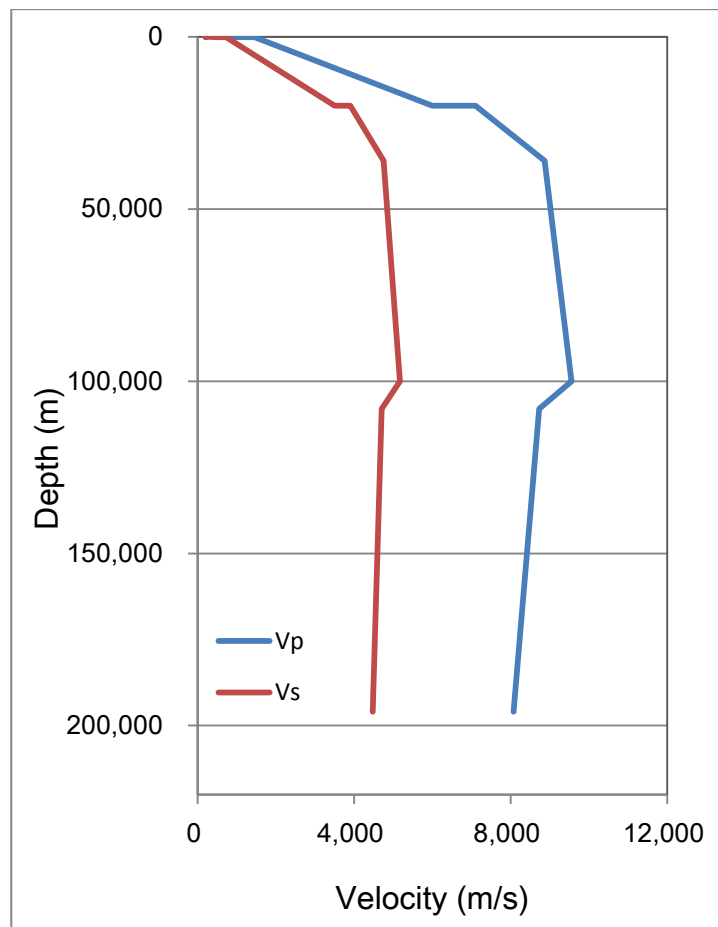
Figure 4.14: Representative earth structure of the source region to calculate Green's function. v_p and v_s are primary and shear wave velocities, respectively

4.5   SUMMARY

Inversion of recorded seismograms to obtain fault mechanism and spatial and temporal rupture history is a common approach in seismology. However, the seismogram records are missing in many cases, especially in the developing and the third world countries. Therefore, inverting the pre-determined/observed static ground displacement is considered to have wider applicability.
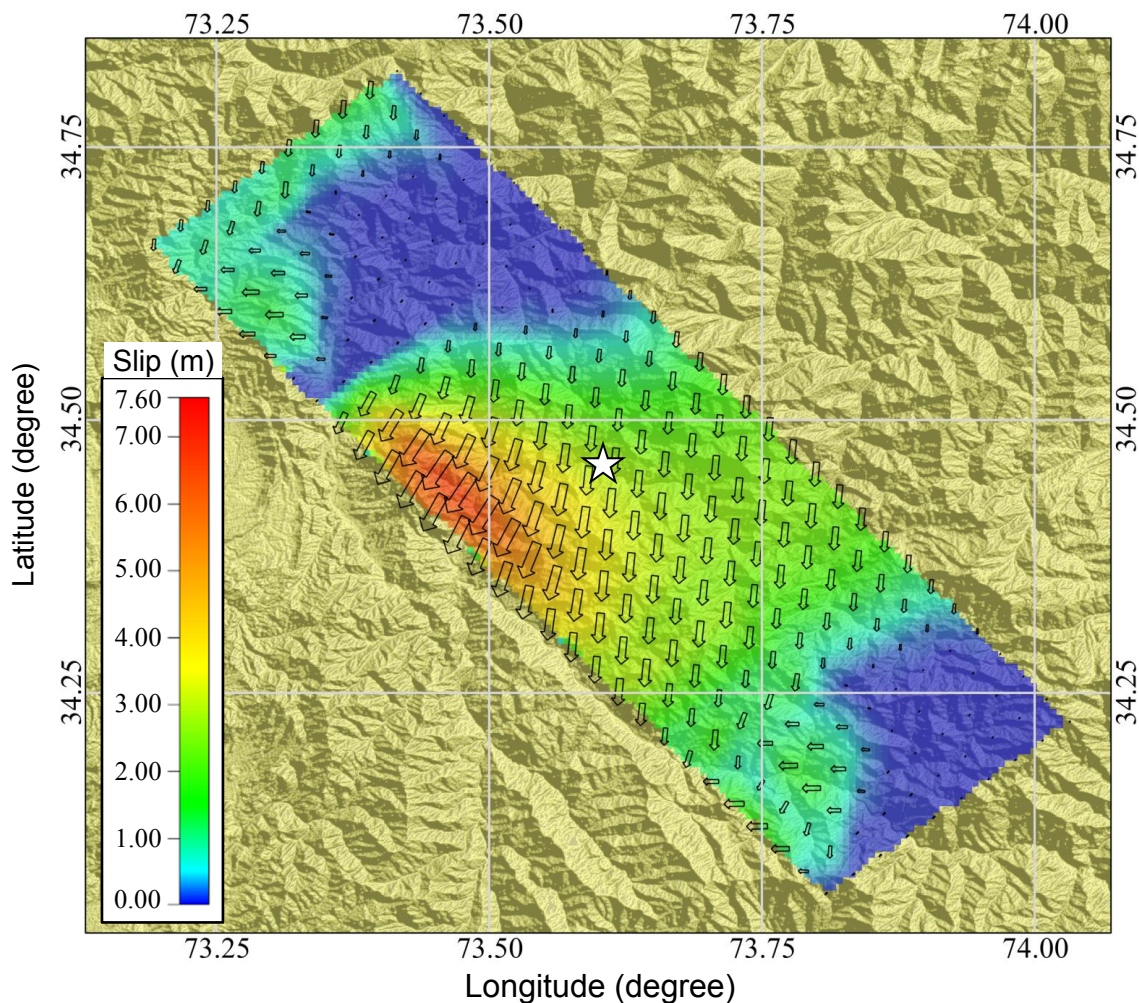
Figure 4.15: Surface projection of the fault slip distribution obtained by the linear geodetic data inversion. The color shows the scale for slip while the vectors are to show only the direction of slip. White star shows the location of hypocenter.
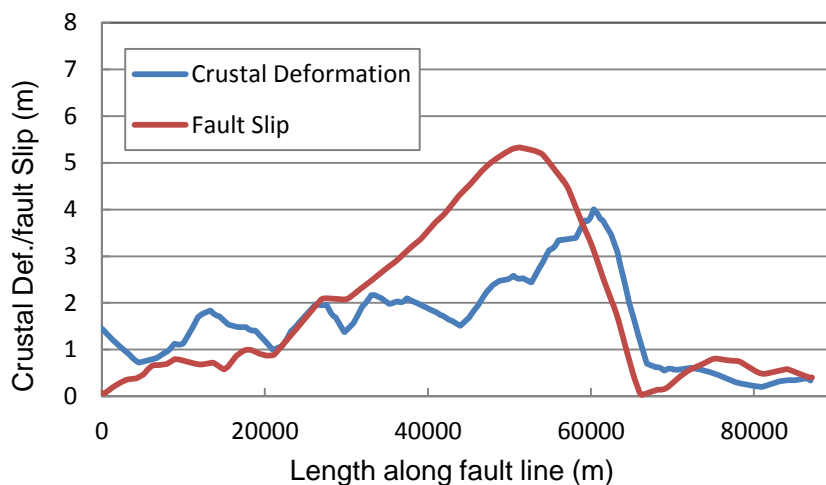
Figure 4.16: Comparison of the lateral component of crustal deformation along the adopted fault rupture plane and fault slip distribution near the ground surface. A very close correlation is observed.

Inversion of very precise and fine resolution Lagrangian ground displacement, around the source area, along with GPS and benchmark observations has successfully simulated the static image of fault slip distribution for a complex multi-segment fault model of Mid-Niigata Prefecture Earthquake. The slip distribution pattern and magnitude with the maximum slip of 1.75m for the main shock was found close to the solutions obtained by the inversion of seismogram records, thus ensuring the acceptability of the method to estimate spatial rupture patterns of seismic faults for better rehabilitation tactics. Interference between the slip distributions on different fault planes of a complex multi-segment fault would definitely exist, especially when the fault planes are close enough and overlapping. However, it was proven that the extent of interference is of practically acceptable level. Furthermore, a detailed and refined slip pattern can be obtained by using high resolution ground deformation data.

Geodetic data inversion analysis has also been carried out for the source of 2005 Kashmir Earthquake with a known fault rupture plan of size 90km x 30kn and strike and dip angles of 320° and 29°, respectively. The earth structure is obtained by combining the sediment accumulation information to the borehole data. A reverse fault type has been revealed through the analysis, which is in accordance with the pre-existing active faults. The largest asperity of fault slip has been observed at shallower depth around the extension of hypocenter and to its north. The maximum simulated value of fault slip is about 7.6 meters. This is the same location where large crustal deformation has been detected by different authors. The magnitude and pattern of fault slip at the surface extension of the fault plane is well consistent with three dimensional crustal deformations pattern both by magnitude and direction.

REFERENCES

1. T. Maruyama (1964). Statical elastic dislocation in an infinite and semi infinite medium, Bull. Earthquake Res. Inst. Univ. Tokyo, 42, 289–368.

2. M. Matsu'ura (1977a). Inversion of geodetic data. Part I: Mathematical formulation, J. Phys. Earth, 25, 69–90.

3. M. Matsu'ura (1977b). Inversion of geodetic data. Part II: Optimal model of conjugate fault system for the 1927 Tango earthquake, J. Phys. Earth, 25, 233–255.

4. M. Matsu'ura and Y. Hasegawa (1987). A maximum likelihood approach to nonlinear inversion under constraint, Phys. Earth planet. Inter., 41, 179-187.

5. M. Matsu'ura, T. Iwasaki, Y. Suzuki and R. Sato (1980). Statical and dynamical study on faulting mechanism of the 1923 Kanto earthquake, J. Phys. Earth, 28, 119-143.

6.   T. Yabuki and M. Matsu'ura (1992). Geodetic data inversion using Bayesian information criterion for spatial distribution of fault slip, Geophsics, 109, 363-375.

7.   Y. Miyashita and M. Matsu'ura (1978). Inversion analysis of static displacement data associated with the Alaska earthquake of 1964, J. Phys. Earth, 26, 333-349.

8.   S. N. Ward and S. E. Barrientos (1986). An inversion for slip distribution and fault shape from geodetic observations of the 1983 Borah Peak, Idaho, earthquake, J. geophys. Res., 91, 4909-4919.

9.   S. E. Barrientos (1988). Slip distribution of the 1985 Central Chile earthquake, Tectonophysics, 145, 225-241.

10. G. J. Funning, B. Parsons and T. J. Wright (2005). Surface displacements and source parameters of the 2003 Bam (Iran) earthquake from Envisat advanced synthetic aperture radar imagery, J. of Geophysical Research, Vol. 110, B09406, doi:10.1029/2004JB003338.

11. K. Aki and P. G.. Richards (1980). Quantitative Seismology, W. H. Freeman, San Francisco 932 pp.

12. M. Bouchon (1979) Discrete wave number representation of elastic wave fields in three-space dimensions, J. Geophys. Res. 84, 3609-3614.

13. M. Bouchon (1980). Calculation of complete seismograms for an explosive source in a layered medium, Geophysics 45, 197-203.

14. M. Bouchon and K. Aki (1977). Discrete wave number representation of seismic source wave fields, Bull Seism. Soc. Am. 67, 259-277.

15. M. Bouchon (1981). A simple method to calculate Green's function forelastic layered media, Bull. Seism. Soc. Am. 71, 959–971.

16. B. L. N. Kennett and N. J. Kerry (1979). Seismic waves in stratified half space, Geophys. J. R. astr. Soc., 57, 557–583.

17. H. Akaike (1980). Likelihood and the Bayes procedure, in Bayesian Statics, J. M. Bernardo, M. H. DeGroot, D. V. Lindley, and A. F. M. Smith (Editors), University Press, Valencia, Spain, 143–166.

18. C. L. Lawson, and R. J. Hanson (1974). Solving Least Square Problems, Prentice-Hall, Inc., New Jersey 340 pp.

19. R. Honda, S. Aoi, H. Sekiguchi, T. Kunugi, and H. Fujiwara (2005). Ground motion and rupture process of the 2004 Mid Niigata Prefecture Earthquake obtained from strong motion data of K-net and KiK-net, Earth Planets Space, 57, 527–532.

20. K. Hikima and K. Koketsu (2005). Rupture processes of the 2004 Chuetsu (mid-Niigata prefecture) earthquake, Japan: A series of events in a complex fault system, Geophysical Research Letters, Vol.32, L18303, 5.

21. S. Fujiwara, M. Tobita, H. P. Sato, S. Ozawa, H. Une, M. Koarai, H. Nakai, M. Fujiwara, H. Yarai, T. Nishimura and F. Hayashi (2006): "Satellite Data Gives Snapshot of the 2005 Pakistan Earthquake," Vol. 87, 7, pp 73-77.

22. E. Pathier, E. J. Fielding, T. J. Wright, R. Walker, B. E. Parsons, and S. Hensley (2006), "Displacement field and slip distribution of the 2005 Kashmir earthquake from SAR imagery," Geophysical research letters, vol. 33, L20310, doi:10.1029/2006GL027193

23. J. P. Avouac, F. Ayoub, S. Leprince, O. Konca, D. V. Helmberger (2006). "The 2005, Mw 7.6 Kashmir earthquake: Sub-pixel correlation of ASTER images and seismic waveforms analysis," Earth and Planetary Science Letters 249, pp 514-528

24. H. Wang, L. Ge, C. Xu, and Z. Du (2007). "3-D coseismic displacement field of the 2005 Kashmir earthquake inferred from satellite radar imagery," Earth Planets Space, 59, 343–349

<div align="right">

Chapter 5

</div>

5 Seismic Stresses in the Interior of Earth's Crust and their Role in Damaging Underground Structures and Triggering Landslides

5.1   INTRODUCTION

Although it still attracts less attention, internal and surface deformations of earth contribute equally or even more than strong ground motions to the earthquake induced devastations. With the increased geodetic observation sites and development of advanced geomorphological surveying techniques in last few decades, more reliable information and knowledge about the earthquake source and rupture mechanism has become evident (as presented in Chapter 4) which can be used as input to model earth's internal and surface deformations.

Most of the moderate to large historical earthquakes are accompanied by numerous landslide disasters and damage to surface and underground infrastructure facilities and life lines (e.g. damage to deeply buried railway and road tunnels, gas and water supply lines, drainage wells, surface communication links etc.). Detailed knowledge of their damage mechanisms is an imperative need for developing rational strategies and design and construction specifications for rehabilitation/reconstruction of the existing facilities and for new construction. Different authors have adopted different parameters and approaches to reach to the root cause of such devastations.

In this chapter, an approach is presented where seismic stresses and deformations in the interior of earth are considered as controlling parameters for earthquake induced damages to surface and subsurface infrastructures.

5.2   ESTIMATION OF SEISMIC STRESSES

For evaluation of co-seismic stress changes in the interior of a semi-infinite half medium, the method developed by Okada (Okada, 1985 and 1992) has been widely used. However, a homogeneous half-space model may oversimplify the actual earth structure, and a model of horizontally layered half-space is considered to be a workaround. There has been a

progressive development in the numerical techniques, numerical stability and computational efficiency of such models since early fifties of nineteenth century based on kernel functions in the wave-number domain (e.g. Sato, 1971; Sato and Matsuura 1973; Sing, 1971 etc.). Both numerical and analytical approaches have been followed to integrate kernel function or wavenumber spectra for a stratified medium. Exponential growth of calculation for kernel functions limited analytical approach to not more than four layers by that time. The simplest and most convenient form of propagator matrix method was first introduced by Thomson (1950) and Haskell (1953) to calculate displacement vector across the layered medium. Although this method was very simple and applicable for any unlimited number of layers, the results showed instability for evanescent cases due to the operation between two different increasing exponentials. Knopoff (1964) and Dunkin (1965) partially solved the problem by introducing minor of the propagator matrix. Nevertheless, it has its own limitations of limited layer thickness and computational cost (Kind, 1983, Schwab et al. 1984). Conclusively, the continuous efforts of improvement in mathematical formulation, stability of results and computational cost were limited in one way or other.

More recently, a robust and stable numerical scheme was developed by Wang (Wang 1999; 2003), and is used herein for the same stratification assumed for the target terrain in source inversion analysis.

5.2.1   Mathematical Formulation

With known dislocation across the fault rupture plane as seismic source, a two point boundary value problem can be solved to obtain stresses/strains and displacement in the interior of stratified earth's crust (Figure 5.1).

The partial differential equation governing static deformation in an elastic medium is given by the equilibrium condition of moment as;

$$f_i + \tau_{ij,j} = 0 \tag{5.1}$$

Where f_i is the body force per unit volume in ith direction and $\tau_{ij,j}$ is derivative of stress tensor with respect to jth component. According to Hook's law

$$\tau_{ij} = C_{ijkl}\varepsilon_{kl} \tag{5.2}$$

Where C_{ijkl} is elastic moduli and ε_{kl} is the strain tensor. For small deformations, the strain tensor ε_{kl} is given as;
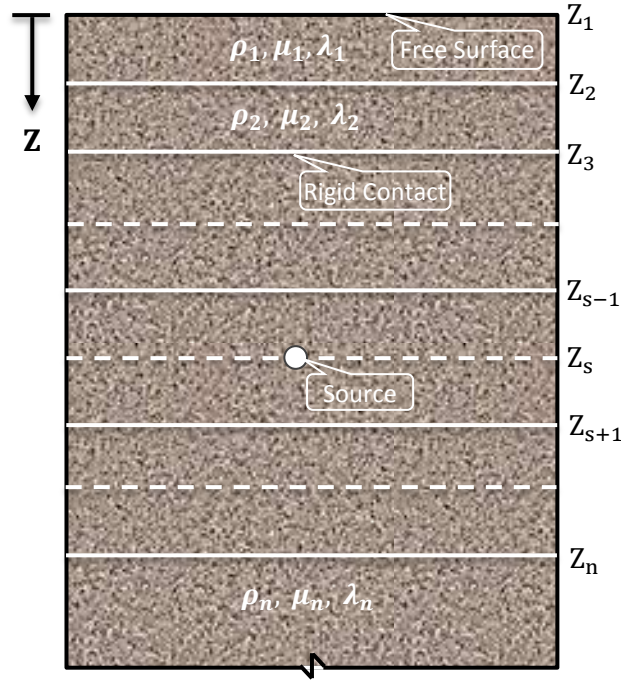
Figure 5.1: Schematic illustration of a two point boundary value problem model for seismic stresses and displacements in the interior of earth's crust.

$$\varepsilon_{kl} = \frac{1}{2}\left(u_{k,l} + u_{l,k}\right) \tag{5.3}$$

Where $u_{k,l}$ is derivative of kth component of u with respect to lth component. For homogeneous and isotropic elastic media, equation (5.2) reduces to

$$\tau_{ij} = \lambda\varepsilon_{kk}\delta_{ij} + 2\mu\varepsilon_{ij} \tag{5.4}$$

Where λ and μ are two Lame's constants, δ_{ij} is Kronecker delta and ε_{kk} is the Einstein's summation notation for strain terms with repeated indices.

Substituting equation (5.3) and (5.4) into equation (5.1), partial differential equation of static deformation in a homogeneous medium is given as

$$(\lambda + 2\mu)u_{j,ij} - \mu u_{i,jj} = f \tag{5.5}$$

By using a generalized differential operator for displacement function, equation (5.5) can be expressed as;

$$(\lambda + 2\mu)\nabla(\nabla \cdot \mathbf{u}) - \mu\nabla \times (\nabla \times \mathbf{u}) = \mathbf{f} \tag{5.6}$$

5.2.1.1 Hankel Transformation

Partial differential equation of static deformation (equation 5.6) is transferred to a set of ordinary differential equations by applying Hankel transformation (Aki and Richard, 1980).

$$u(z, r, \theta) = u_z + u_r + u_\theta$$

$$u(z, r, \theta) = \sum_m \int_0^\infty [U_m(z,k) Z_k^m(r,\theta) + V_m(z,k) R_k^m(r,\theta) + W_m(z,k) T_k^m(r,\theta)] \, k dk \qquad (5.7)$$

Similarly,

$$\tau(z, r, \theta) = \sum_m \int_0^\infty [E_m(z,k) Z_k^m(r,\theta) + F_m(z,k) R_k^m(r,\theta) + G_m(z,k) T_k^m(r,\theta)] \, k dk \qquad (5.8)$$

Where,

$$Z_k^m(r,\theta) = e_z Y_k^m(r,\theta) \qquad (5.9)$$

$$R_k^m(r,\theta) = \frac{e_r}{k} \frac{\partial}{\partial r} + \frac{e_\theta}{kr} \frac{\partial}{\partial \theta} Y_k^m(r,\theta) \qquad (5.10)$$

$$T_k^m(r,\theta) = \frac{e_r}{kr} \frac{\partial}{\partial \theta} - \frac{e_\theta}{k} \frac{\partial}{\partial r} Y_k^m(r,\theta) \qquad (5.11)$$

With

$$Y_k^m(r,\theta) = J_m(kr) \begin{pmatrix} \cos(m\theta) \\ \sin(m\theta) \end{pmatrix} \qquad (5.12)$$

$U_m, V_m, \dots$ are wave number spectra of the stress and displacement and Z_k^m, R_k^m, T_k^m are corresponding surface vector harmonics.

The resulting ordinary differential equations are decoupled into two sets based on the depth dependent coefficients of displacement vectors. These two systems of equations are called poloidal and toroidal modes and represent P-SV and SH wave field, respectively. The resulting set of ordinary equations for P-SV mode is given by:

$$\frac{d}{dz} y_m = A y_m \qquad (5.13)$$

where y_m and A are the generalized displacement vector and coefficient matrix, respectively, given by:

$$y_m = (U_m \quad E_m \quad V_m \quad F_m)^T \qquad (5.14)$$

$$A = \begin{bmatrix} 0 & 1/(\lambda + 2\mu) & \lambda k/(\lambda + 2\mu) & 0 \\ 0 & 0 & 0 & k \\ -k & 0 & 0 & 1/\mu \\ 0 & -\lambda k / (\lambda + 2\mu) & 4k^2\mu(\lambda + \mu)/(\lambda + 2\mu) & 0 \end{bmatrix} \qquad (5.15)$$

Similarly for the SH mode, the resulting equation are;

$$\frac{d}{dz}x_m = Bx_m \qquad (5.16)$$

with the generalized displacement vector, x_m, and the coefficient matrix, B, given as;

$$x_m = (W_m \quad G_m)^T \qquad (5.17)$$

$$B = \begin{bmatrix} 0 & 1/\mu \\ k^2\mu & 0 \end{bmatrix} \qquad (5.18)$$

Mathematical details and theory in this section are from (Aki and Richard, 1980; Kenett and Kerry, 1979; Wang et al., 2003 etc.)

5.2.1.2 Haskell Propagator Matrix Method

Analytical solution of ordinary differential equation for P-SV mode (equation 5.13) for homogeneous layer is given as;

$$y(z) = L(z)E(z)c \qquad (5.19)$$

Where L is a 4 x 4 layer matrix whose columns are eign vectors of the coefficient matrix A and gives by Aki and Richard (1980) and Kennet (1983) as

$$L(z) = \begin{bmatrix} 1 & 1 & 1 + \dfrac{\lambda + \mu}{\mu}(1 - kz) & 1 + \dfrac{\lambda + \mu}{\mu}(1 - kz) \\ 2\mu k & -2\mu k & 2(\lambda + \mu)(1 - kz)k & -2(\lambda + \mu)(1 - kz)k \\ 1 & -1 & -1 - \dfrac{\lambda + \mu}{\mu}kz & 1 - \dfrac{\lambda + \mu}{\mu}kz \\ 2\mu k & 2\mu k & -2(\lambda + \mu)k^2 z & 2(\lambda + \mu)k^2 z \end{bmatrix} \qquad (5.20)$$

c is a four dimensional constant vector to be determined and $E(z)$ is 4x4 diagonal matrix

$$c = [A_+, \quad B_+, \quad A_-, \quad B_-]^T \qquad (5.21)$$

$$E(z) = \begin{bmatrix} e^{\alpha z} & 0 & 0 & 0 \\ 0 & e^{\beta z} & 0 & 0 \\ 0 & 0 & e^{-\alpha z} & 0 \\ 0 & 0 & 0 & e^{-\beta z} \end{bmatrix} \qquad (5.22)$$

$\pm \alpha$ and $\pm \beta$ are the four eigen values of coefficient matrix A.

Following the same lines, solution for SH mode can also be obtained. Detailed entities of coefficient matrix etc. can be found in Aki and Richard (1980) and Wang et al. (2003).

5.2.1.3 Source and Boundary Conditions

Partially known boundary conditions at the free surface and at the lowest interface (above half-space) make it a two point boundary value problem. The ground surface is taken as traction free, reducing the displacement vectors of equations (5.14) and (5.17) to

$$y_1 = (U_m \quad E_m \quad 0 \quad 0)^T \tag{5.23}$$
$$x_1 = (W_m \quad 0)^T \tag{5.24}$$

There are no up-going waves at the lowest interface and, therefore, the displacement vector reduces to

$$y_n = L_n (0 \quad 0 \quad A_- \quad B_-)^T \tag{5.25}$$

At inner boundaries, laterally homogeneous layers are considered in a welded contact i.e. displacements and stresses are continuous across them.

Source is modeled by a jump/discontinuity of the generalized displacement vector. The fault planes are modeled by superimposing double couples, single forces, inflations, etc. Source functions for different source types are given in Appendix A. Solution vectors are propagated downward from the surface to just above the source and upward from the lowest interface to just below the source. The decomposition constants are then determined by satisfying the source condition. The displacement vectors are ortho-normalized after each layer for stability.

5.3   ESTIMATION OF INSITU ROCK STRESSES

Other than the earthquake-induced stress changes mentioned above, in-situ state of initial rock stress is necessary to be incorporated. However, incorporation of static stresses, particularly around a tunnel cavity, is not an easy task. Before tunnelling, rock pressure can be largely affected by the weight of its overburden. But the secondary rock pressure after tunnelling may be often the weight of a rock mass of a certain height above the tunnel, which, when left unsupported would gradually drop out of the roof. The amount of time

elapsing after the rock was formed may have determined initial rock stress conditions. Given less prospect for obtaining complicated stress conditions around a tunnel cavity, only initial stress conditions in rock masses with no inclusion of cavity is discussed herein.

5.3.1 Coefficient of Lateral Pressure

The New Austrian Tunneling Method (NATM), which relies on the inherent strength of the surrounding rock mass, requires installation of sophisticated measurement instrumentation. By virtue of this method, Matsumoto and Nishioka (1991) estimated coefficients of lateral rock pressure using the measured values of convergence of tunnel cross-sections in both the transverse and vertical directions (Figure 5.2). According to Matsumoto and Nishioka (1991), ground convergence around a circular tunnel opening is summation of the convergence of unsupported tunnel cavity, convergence due to shotcrete tunnel lining and convergence due to the rock bolts;

$$u_r(k,\theta) = u_r^{(2)}(k,\theta) + u_r^{(3)}(k,\theta) + u_r^{(4)}(k,\theta) \tag{5.26}$$

where $u_r^{(2)}(k,\theta)$, $u_r^{(3)}(k,\theta)$ and $u_r^{(4)}(k,\theta)$ are the ground displacements without support, due to shotcrete tunnel lining and rock bolting, respectively, given in terms of overburden stress (σ_v), coefficient of lateral pressure (k) and size of the tunnel opening.
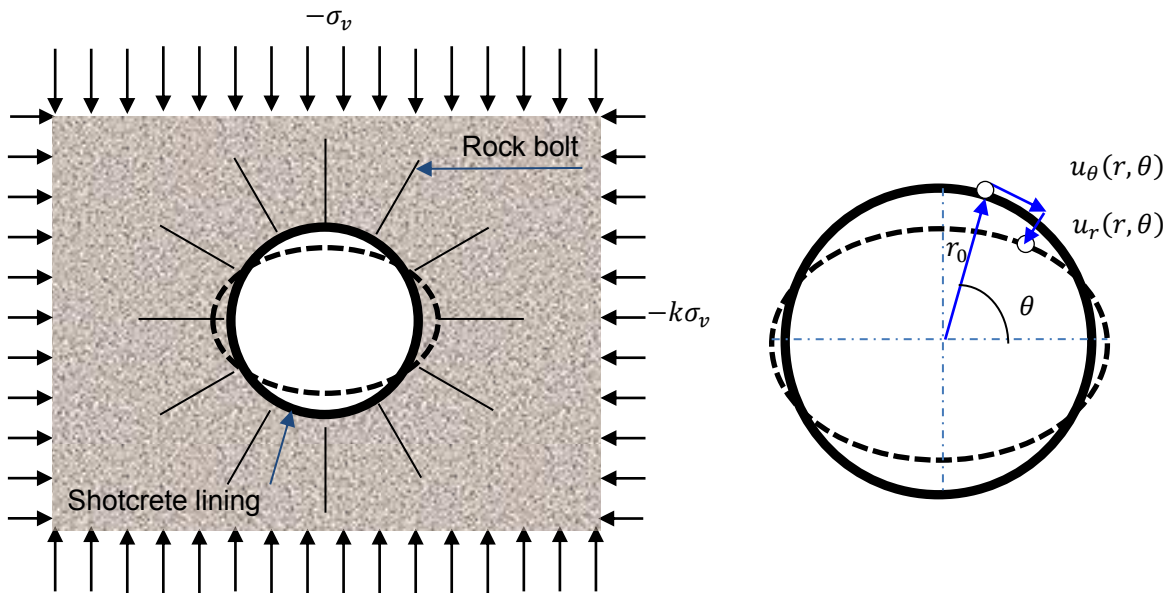
Figure 5.2: Schematic illustration of displacement around a circular tunnel to back calculate coefficient of lateral pressure from horizontal and vertical convergences (after Matsumoto and Nishioka, 1991)

$$u_r^{(2)}(r_0,\theta) = \frac{-\sigma_v r_0(1+v_R)}{2E_R}[(1+k)-(1-k)(3-4v_R)\cos 2\theta] \tag{5.27}$$

$$u_r^{(3)}(r_0,\theta) = \frac{\sigma_v r_0(1+v_R)}{E_R}\alpha_A\left\{(1+k)-(1-k)(3-4v_R).\left(\frac{1-3v_R}{1-v_R}\right)\cos 2\theta\right\} \tag{5.28}$$

$$u_r^{(4)}(r_0,\theta) = \frac{\sigma_v r_0(1+v_R)}{E_R}\alpha_B \tag{5.29}$$

With

$$\alpha_A = \frac{E_c(1+v_R)}{2E_R(1-v_c^2)}\frac{t}{r_0} \tag{5.30}$$

$$\alpha_B = \frac{nA_B\sigma_B}{2\pi r_0 Ls} \tag{5.31}$$

Here t is the thickness of shotcrete lining, E_c is Young's modulus of shotcrete lining and E_R is the coefficient of deformation for ground, v_c and v_R are Poisson's ratios for shotcrete lining and ground, respectively. A_B is cross sectional area of rock-bolt and n is number of rock bolts in axial length of tunnel L.

Figure 5.3 shows coefficient of lateral pressure calculated by Matsumoto and Nishioka for tunnels embedded in soft sedimentary rocks. With the available convergence data of two tunnels in the Niigata area, coefficients of lateral pressure is calculated by considering only the first term of Equation (5.26) (i.e. ground displacement with no support). The other two terms in Equation (5.26) are ignored due to unavailability of the data and their relatively smaller magnitudes. The ratio of transverse and vertical unsupported ground convergence can be simplified to;

$$\frac{u_h}{u_v} = \frac{u_r(r_0,0)}{u_r\left(r_0,\frac{\pi}{2}\right)} = \frac{4k+4v_R-4kv_R-2}{4kv_R-2k-4v_R+4} \tag{5.32}$$

Given with horizontal and vertical convergences, coefficient of lateral pressure, k, can be calculated for any value of Poisson's ratio.

Although the latter two terms of equation (5.26) were ignored, the obtained values of coefficient of lateral pressure joined the cluster of points obtained by Matsumoto and Nishioka for soft sedimentary rocks (Figure 5.3). The obtained coefficients are about equal to 0.9 to 1.0, showing sharp contrast with the large scatter of coefficients for stiff rocks (Matsumoto and Nishioka, 1991).
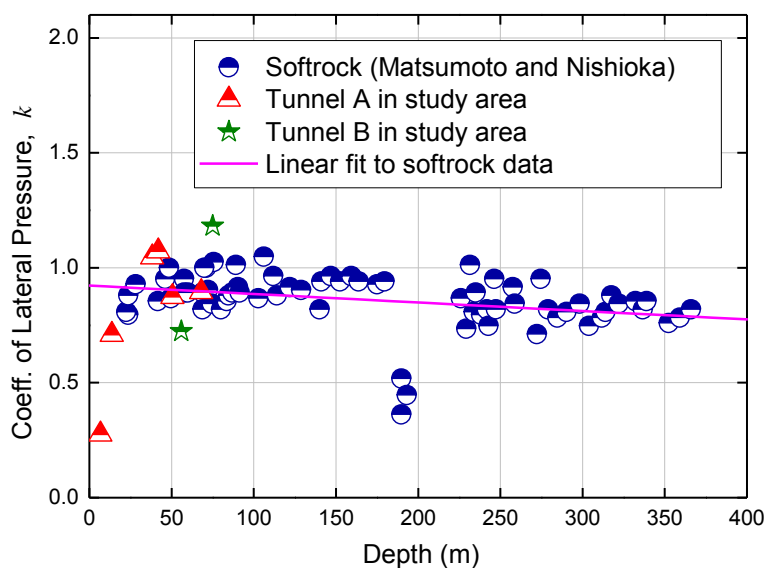
Figure 5.3: Coefficient of lateral pressure calculated from the ground displacement data. Tunnels A and B are two tunnels with available convergence data within the study area.

5.4   ROLE IN DAMAGING UNDERGROUND FACILITIES

It has been revealed from the history that mountain tunnels, which are usually considered significantly earthquake resistant because of the stable surrounding ground, have suffered significant damage during large near-field earthquakes accompanied by large soil deformations. Table 5.1 summarizes the extent of damage to mountain tunnels in Japan during large earthquakes in past one century.

One of the recent eye-openers was the damage to railway tunnels in the 2004 Mid-Niigata Prefecture Earthquake. This earthquake attracted attentions of civil engineers in the sense that a number of damages to both railway and road tunnels were reported (Konagai et al., 2009; Johansson et al., 2007; Jiang et al., 2010; and East Japan Railway Company, 2006). Damages to shallow tunnels and tunnel mouths made up the vast majority, but some damages were reported even to several-tens-to-over-hundred-meters-deep tunnels for the Joetsu line of the Japanese bullet train network called "Joetsu Shinkansen" (Johansson et al., 2007; Jiang et al., 2010; and East Japan Railway Company, 2006). Within the 8.6km Uonuma tunnel for example, a 5 m long section of the arch collapsed. There was also surface spalling of concrete from a side wall, and the concrete track-bed lifted off the invert over three separate sections totaling 250 m, located 195.08, 195.12 and 198.7 km from the Tokyo Station (East Japan Railway Company, 2006). It was fortunate that Toki No. 325, a passenger-carrying train bound for Niigata, which was derailed, had passed through the Uonuma Tunnel just three minutes before the earthquake hit (EERI Special Earthquake

Report, 2005).

Since tunnels closely follow the motions of their surrounding soils, strain buildups along damaged tunnels are to be discussed to take firm steps to clarify the causes of these tunnel damages.

Table 5.1: Extent of damage to mountain tunnels in Japan during large earthquakes in last one century (after Asakura et al., 2001)

Year, Name	Magnitude	Epicenter	Tunnel Performance
1923 Kanto	7.9	Sagami Bay (Depth: unknown)	Extensive, severest damage to more than 100 tunnels in southern Kanto area
1927 Kita-Tango	7.3	7km WNW of Miyazu, Kyoto (Depth: 0km)	Very slight damage to 2 railway tunnels in the epicentral region
1930 Kita-Izu	7.3	7km west of Atami, Shizuoka (Depth: 0km)	Very severe damage to one railway tunnel due to earthquake fault crossing
1948 Fukui	7.1	12km north of Fukui City (Depth: 0km)	Severe damage to 2 railway tunnels within 8km from the earthquake fault
1952 Tokachi-Oki	8.2	Pacific Ocean, 73km ESE off the Cape Erimo (Depth: 0km)	Slight damage to 10 railway tunnels in Hokkaido
1961 Kita-Mino	7.0	Near the border between Fukui and Gifu Prefectures (Depth: 0km)	Cracking damage to a couple of aqueduct tunnels
1964 Niigata	7.5	Japan Sea, 50km NNE of Niigata City (Depth: 40km)	Extensive damage to about 20 railway tunnels and one road tunnel
1968 Toikchi-Oki	7.9	Pacific Ocean, 140km SSE off the Cape Erimo (Depth: 0km)	Slight damage to 23 railway tunnels in Hokkaido
1978 Izu-Oshima-Ki nkai	7.0	In the sea between Oshima Isl. and Inatori, Shizuoka (depth: 0km)	Very severe damage to 9 railway and 4 road tunnels in a limited area
1978 Miyagiken-Oki	7.4	Pacific Ocean, 112km east of Sendai City, Miyagi (Depth: 40km)	Slight damage to 6 railway tunnels mainly existing in Miyagi Prefecture
1982 Urakawa-Oki	7.1	Pacific Ocean, 18km SW of Urakawa, Hokkaido (Depth: 40km)	Slight damage to 6 railway tunnels near Urakawa
1983 Nihonkai-Cyub u	7.7	Japan Sea, 90km west of Noshiro City, Akita (Depth: 14km)	Slight damage to 8 railway tunnels in Akita, etc.
1984 Naganoken-Sei bu	6.8	9km SE of Mt. Ontake, Nagano (Depth: 2km)	Cracking damage to one hydraulic power tunnel

1987 Chibaken-Toho -Oki	6.7	Pacific Ocean, 8km east off Ichinomiya Town, Chiba (Depth: 58km)	Damage to the wall of one railway tunnel at Kanagawa-Yamanashi border
1993 Notohanto-Oki	6.6	Japan Sea, 24km north of Suzu City, Ishikawa (Depth: 25km)	Severe damage to one road tunnel
1993 Hokkaido-Nansei-Oki	7.8	Japan Sea, 86km of west Suttsu Hokkaido (Depth: 35km)	Severe damage to one road tunnel due to a direct hit of falling rock
1995 Hyogoken-Nanbu	7.2	Akashi strait (Depth: 18km)	Damage to over 20 tunnels, about 10 tunnels required repair and reinforce
2004 Niigataken-Chuetsu	6.8	Kawaguchi-machi, Ojiya City (Depth: 13km)	Damage to about 50 tunnels, of which 25 or so needed reinforcement or repair.

5.4.1   Damage to Railway Tunnels in Mid-Niigata Prefecture Earthquake

Joetsu line of the Japanese bullet train network called "Joetsu Shinkansen" (Joetsu new-line in Figure 5.4) opened on Nov. 15, 1982, on a 303.6 kilometer stretch between Omiya and Niigata (Japan Railway general construction report, 1984). It was later extended 30.3 km south to Tokyo Terminal. The line is significantly shorter than the other Shinkansen lines, yet its construction was a big challenge because the line was planned to run through one of the most heavily snow-covered regions in the country. Eventually, the line goes through continuous series of tunnels in the area north of Takasaki Station to about 10km south of Nagaoka Station. Tunnels in this section between Takasaki and Nagaoka stations measure 103.2km as a whole, about 76% of the entire stretch of this 136.1 km-long snowy section.

The seismic center of the Mid-Niigata Prefecture Earthquake was a low-rise mountainous area to the northwest of the continuous tunnel section of this line (Figure 5.4). Ten tunnel sections of Joetsu new Line and two sections of the Joetsu old Line were found damaged at depths deeper than 40m (Figures 5.4 and 5.5). East Japan Railway Company (JR East) owning these lines have grouped these sections into the following four categories based on their damage extents.

(1) Category 1: Minor damage, which do not obstruct train passing.

(2) Category 2: Minor damage slightly in need of repair

(3) Category 3: Damage badly in need of restoration. They include buckling and spalling of tunnel linings.

(4) Category 4: Seriously damaged impassable sections badly in need of restoration. They include buckling of track-bed concrete slabs and large spalling of tunnel crowns and side

walls.

Damaged sections were clustered in Horinouchi, Uonuma, Myoken and Takiya Tunnels of the new line in order from south, and in Wanazu Tunnel of the old line. Among these tunnels, the damage to Uonuma Tunnel was the most serious. Some details of the damaged sections chosen for this study (extracted from Commission report, East Japan Railway Company, 2006) are summarized in the following sections.
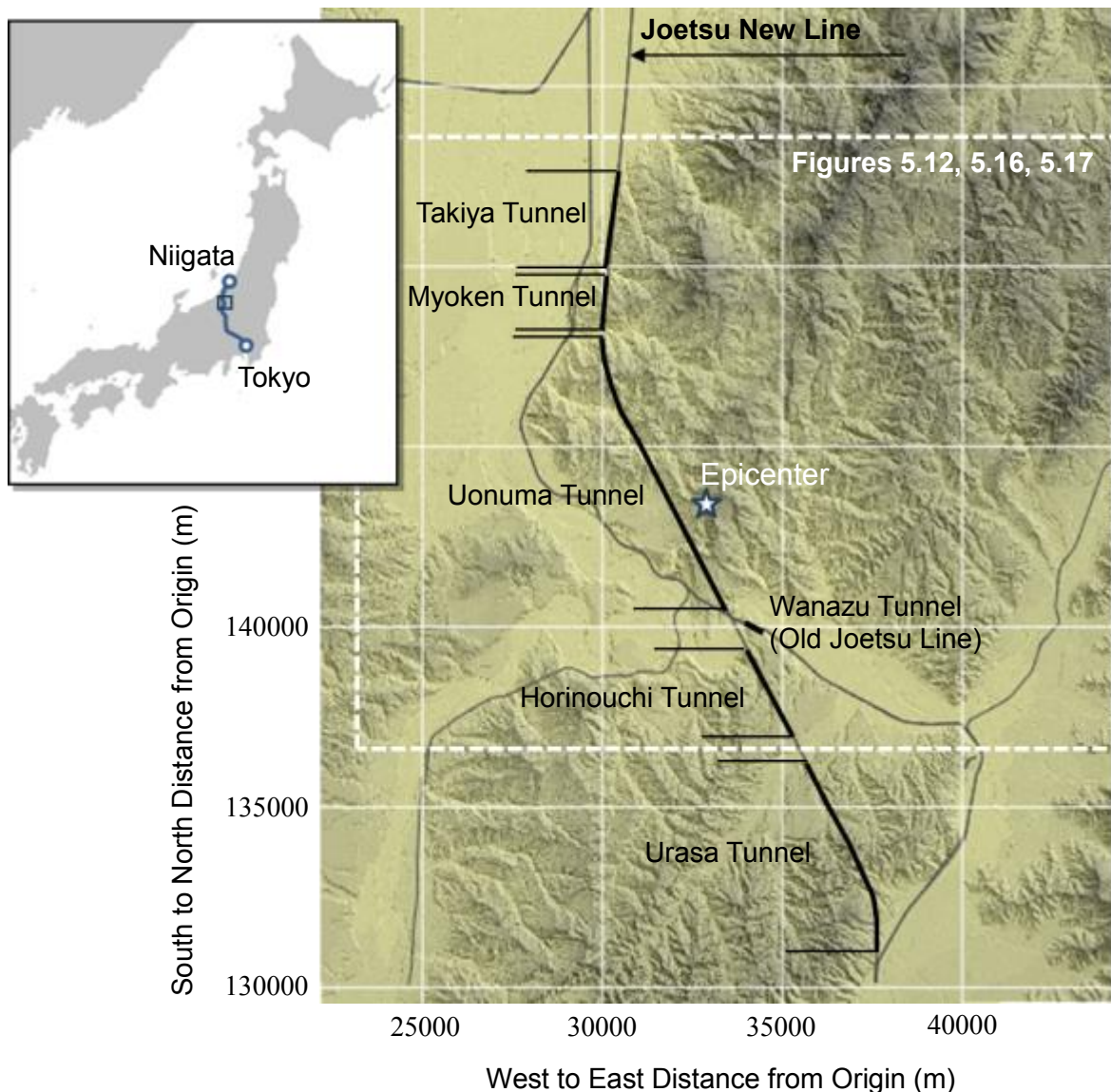
Figure 5.4: Tunnels of Joetsu New Line near the epicenter of the October 23rd 2004 Mid-Niigata-Prefecture Earthquake (37.2917°N, 138.8666°E): The terrain shown above is a digital representation of cartographic information (Digital Elevation Model) in a raster form with pixels arranged in $5\mathrm{m} \times 5\mathrm{m}$ square (Digital Basic Map of Japan, Geospatial Information Authority of Japan). Topographical mapping is on the JGD2000/ Japan Plane Rectangular Coordinate System VIII with its southwest corner located as the origin at $138°30'00"\mathrm{E}, 36°00'00"\mathrm{N}$.
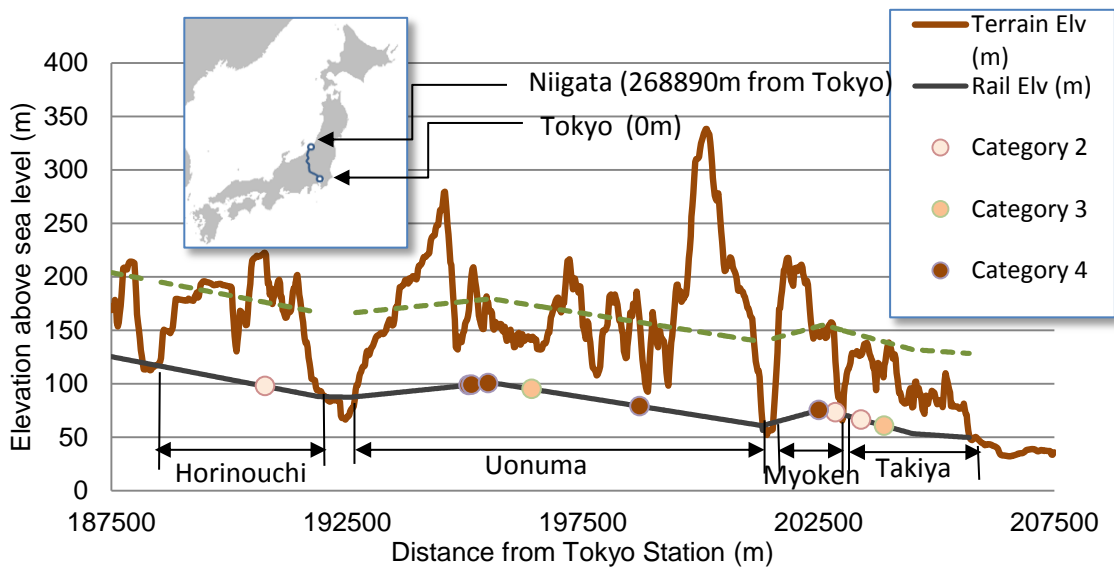
Figure 5.5: Tunnel sections damaged in the 2004 Mid-Niigata-Prefecture Earthquake: The average depth of tunnels over the illustrated 20km stretch is 75m (see green broken line). JR East grouped the damaged sections into four categories based on their damage extents with larger number showing more serious damage (Commission report, East Japan Railway Company, 2006). Refer to the body text for more details.

5.4.1.1 Horinouchi Tunnel

Horinouchi Tunnel is a 3,300 meter long concrete tunnel excavated across a large syncline of an active folding of Pliocene to Pleistocene time. The damaged section, located at around 1.1 km from its northwest mouth, and about 20m deep below the ground surface, passes through the northwestern side of a syncline exhibiting an inclined alternate stratification of unconsolidated sand and mud rock layers (Figure 5.6 and Table 5.2).
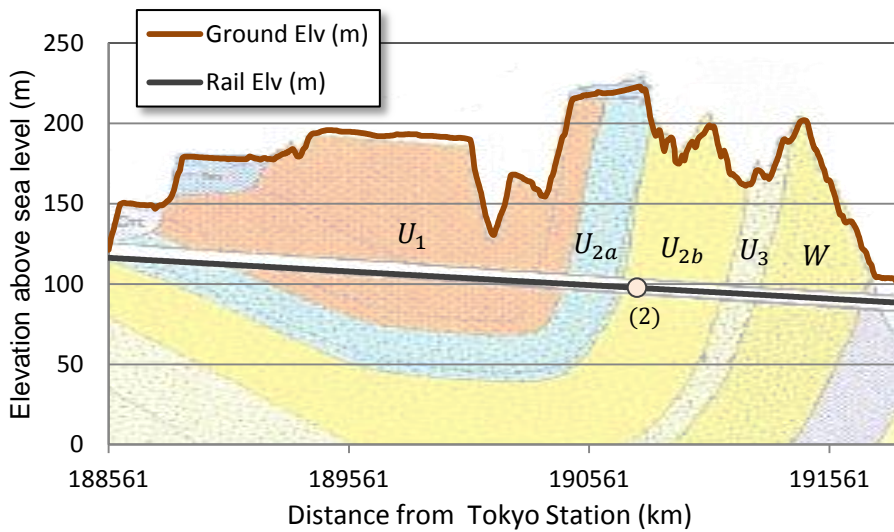
Figure 5.6: Stratigraphic profile (Commission report, East Japan Railway Company, 2006; Yanagisawa et al., 1986) along Horinouchi Tunnel: Geology legend is given in Table 5.2. Circle(s) show damaged section(s) with the damage extent categories parenthesized.

Table 5.2: Geology legend for Figures 5.6, 5.7 and 5.10: Contains the Japan Geological Survey (JGS) geological map symbology and stratigraphic nomenclature (Yanagisawa et al., 1986). Color identification is based on Reference (Commission report, East Japan Railway Company, 2006).

	U_3	Pleistocene	Marine silt, sand and gravel
	U_{2b}	Pleistocene	Mudstone inter-bedded with sand
	U_{2a}	Pleistocene	Silt, sand and gravel
	U_1	Pliocene	Gravel, silt and sand
	W	Pliocene	Sandstone
	S	Pliocene	Sandy mudstone, and thinly inter-bedded sandy mudstone
	U_s	Pliocene	Massive mudstone intercalating sandstone in part
	K_{u2}	Pliocene	Sandy mudstone inter-bedded with sandstone
	K_{u1}	Pliocene	Mudstone inter-bedded with sandstone
	K_l	Pliocene	Sandstone inter-bedded with mudstone
	A	Pliocene	Dark gray massive mudstone

When the tunnel was constructed, consideration was given to these unconsolidated sand layers, which are susceptible to a progressive failure. Therefore the tunnel was excavated with either double side drifts or a single bottom drift excavated in advance.

The earthquake has done a rather minimal damage to this section. Tunnel side walls were slightly pushed inward causing relatively small surface spalling and an about 23mm dislocation of a transverse lining joint. Three shear keys for track-bed slabs were also found detached from the invert.

5.4.1.2 Uonuma Tunnel

This 8,625 meter long concrete tunnel was excavated with the drift method. On the whole, the stratigraphic profile along the tunnel exhibits a large up-fold structure. However to close examination, the stratified sequence is often disturbed by shallow landslides and a deeply bedding fault rupture plane (Figure 5.7). This tunnel experienced a significant damage to its lining and track-bed, which was mainly concentrated at five different locations (marked as a_1, a_2, a_3, a_4 and a_5 in Figure 5.7). Among these five locations, Sections a_1 and a_2 were the most seriously damaged (Figures 5.8 and 5.9). The rail buckled together with the track-bed concrete slab, which was uplifted by about 250 mm over a 100 meters long stretch indicating an axial compression of the tunnel most likely due to tectonic compression of the surrounding soil as will be discussed later. Along a band of large cracks diagonally traversing the lining (yellow lines in Figure 5.9), the tunnel arch was crushed and large concrete chunks fell down off the 5 m long section of the tunnel crown. After the earthquake, 53 rock cores were drilled at this section along two horizontal lines on both tunnel side walls over about 100m distance. Not a small number of rock cores were found

cracked. Cracks were denser near the tunnel wall over an about 1 to 2m length of each rock core. These seriously cracked cores made up a wide brush, which conform to the crack band that appeared diagonally across the tunnel lining. Other than this, it was found that there is a tuff layer bedding within this brush of cracks. The most-likely strike and dip of this tuff layer were estimated to be N18^{o}E and 42° to 43°, respectively. Uniaxial compressive strengths of mud rock, turbidite (sedimentary deposit formed by a turbidity current) and sand stone cores ranged 3000 to 8000 kN/m^2, 300 to 2000 kN/m^2 and 400 to 800 kN/m^2, respectively.
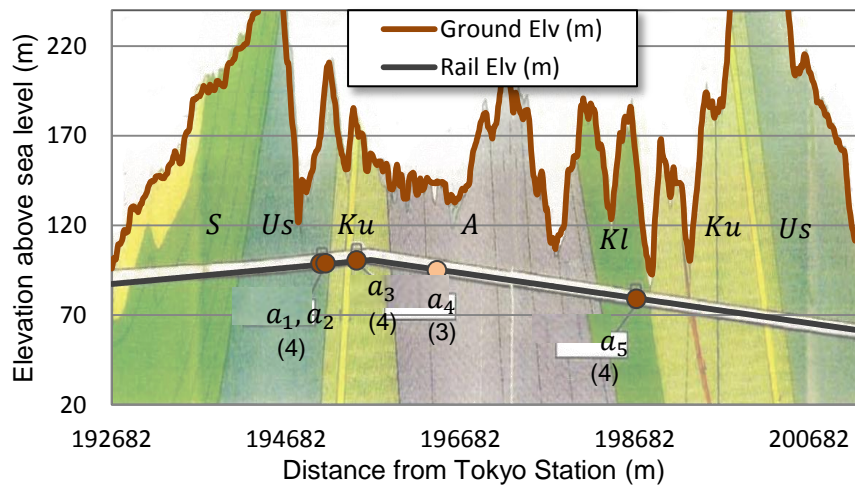
Figure 5.7: Stratigraphic profile (Commission report, East Japan Railway Company, 2006; Yanagisawa et al., 1986) along Uonuma Tunnel: Geology legend is given in Table 5.2. Circle(s) show damaged section(s) with the damage extent categories parenthesized.
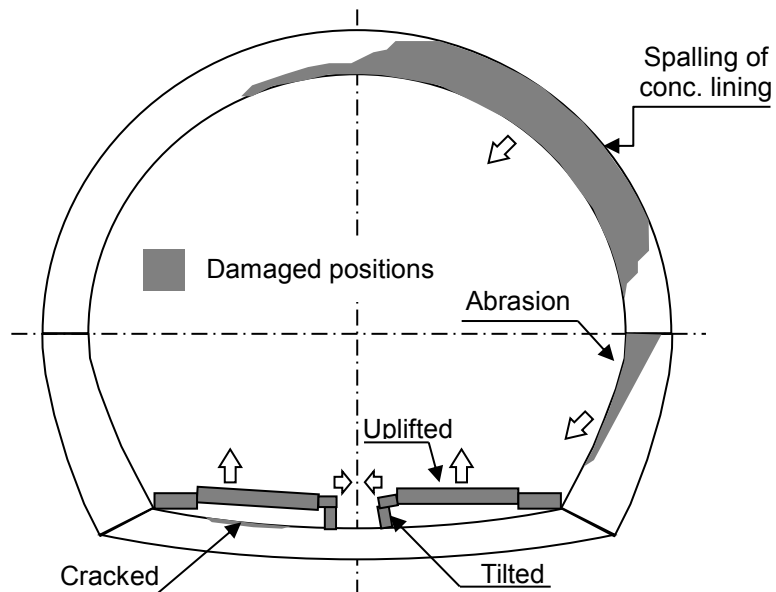
Figure 5.8: Schematic illustration of failure pattern at most seriously damaged section (a_1) of Uonuma Tunnel

Figure 5.9: Most seriously damaged section of Uonuma Tunnel: The rail buckled together with the track-bed concrete slab, which was uplifted by about 250 mm over a 100 meters long stretch (see white arrows). A band of large cracks diagonally traversed the lining (yellow lines). Large concrete chunks fell down off the 5 m long section of the tunnel crown. Photo was taken at Point a_1 (37.2833°N, 138.86579°E), 195,050m from Tokyo Station by Konagai, K. (Johansson et al., 2007)

5.4.1.3 Myoken Tunnel

The 1,459 meter long concrete tunnel was excavated with the top heading method. Figure 5.10 shows stratigraphic profile along the tunnel. The tunnel passes through a stratified sedimentary rock mass with its beds dipping 20° to 22° to northwest and striking 14° to 18° to northeast. The damaged locations (marked as a_1 and a_2 in Figure 5.10) are about 75 meters deep below the ground surface. Though less serious than Uonuma tunnel, Section a_1 experienced most serious damage. Figure 5.11 shows schematic illustration of the extent and pattern of failure at most seriously damaged sections (a_1). Tunnel's cross-section was laterally squeezed inward over an about 50m stretch causing crushing of the arch crown, cracking of concrete lining of the side walls and buckling of the track-bed. Crushing of the arch crown and concrete lining was also observed at section a_2.
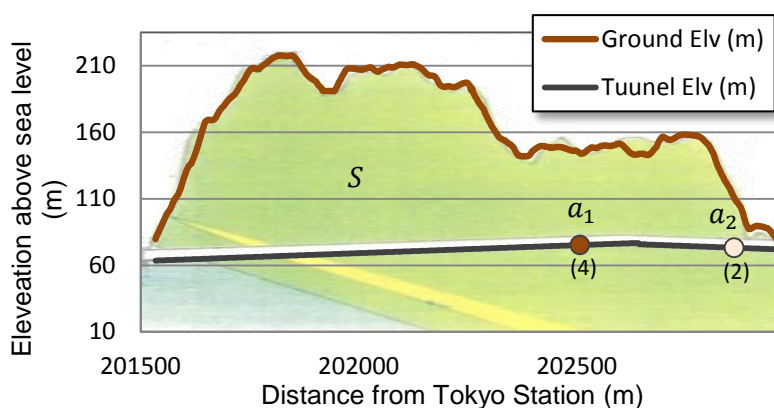
Figure 5.10: Stratigraphic profile (Commission report, East Japan Railway Company, 2006; Yanagisawa et al., 1986) along Myoken Tunnel: Geology legend is given in Table 5.2. Circle(s) show damaged section(s) with the damage extent categories parenthesized.
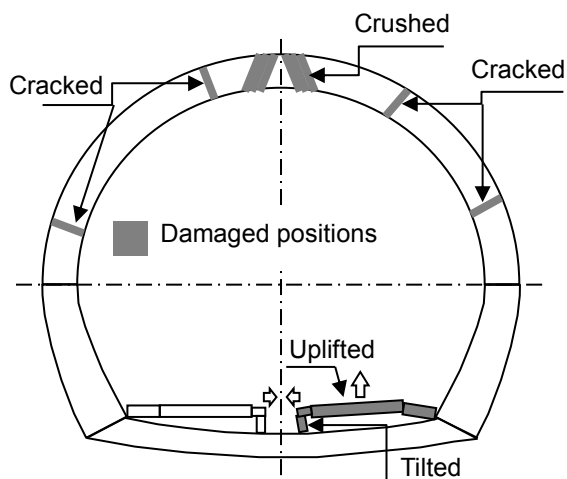
Figure 5.11: Schematic illustration of failure pattern at most seriously damaged section (a_1) of Myoken Tunnel

5.4.2   Seismic Stresses for Mid-Niigata Prefecture Earthquake

As illustrated in Figure 5.4, the average tunnel depth along the low-raised mountain route is 75m with the standard deviation of 45m. The spatial variation of square root of the second principal invariant of the stress deviator tensor, $\sqrt{J_2}$, at the 75m depth was obtained for the entire target area (Figure 5.12). $\sqrt{J_2}$ was considered to serve as a work-a-round indicator of the rock's vulnerability to failure in the absence of reliable information of rock failure criteria. It is remarkable that several stripes of large $\sqrt{J_2}$ values appear in parallel at a regular interval of about 4 km, with each stripe trending in NE-SW direction. Almost all damaged tunnel sections deeper than 40m (colored circles in Figure 5.12) are found within these parallel brushes.
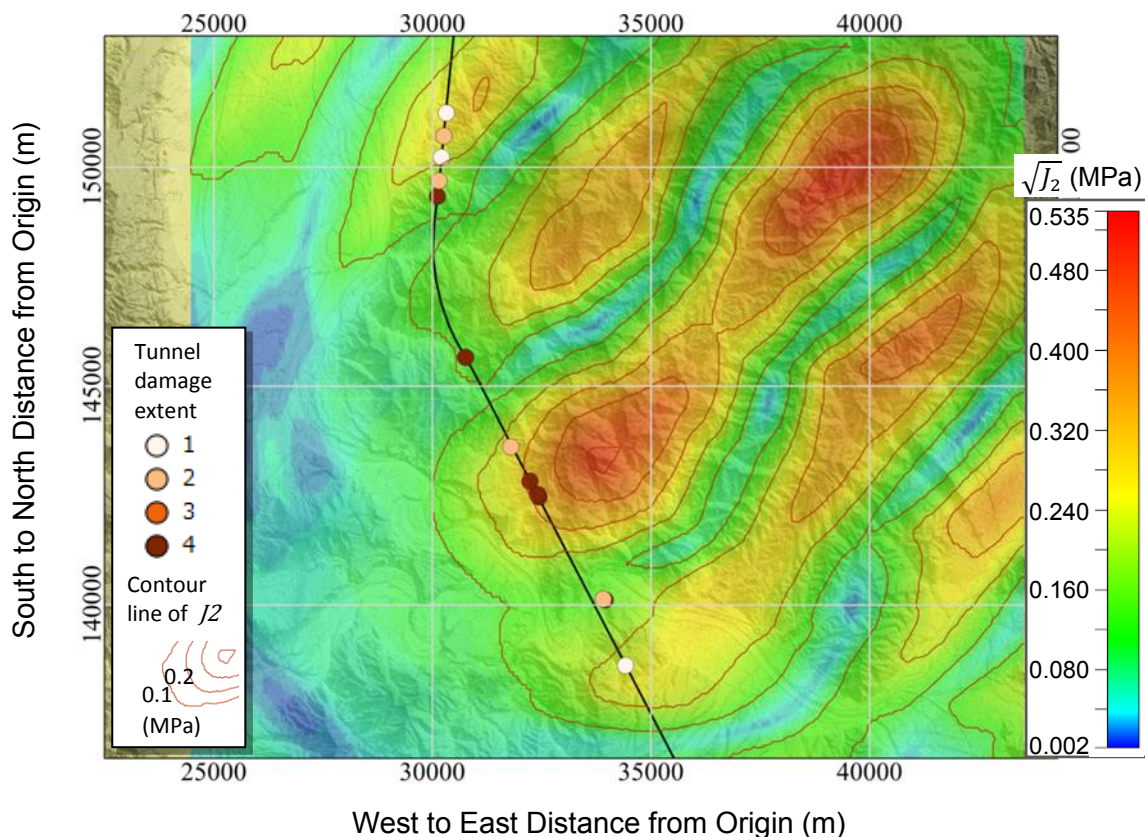
Figure 5.12: Distribution of second principal invariant of the stress deviator tensor $\sqrt{J_2}$ over the entire target zone at the depth of 75 meters below ground surface, with locations of damaged tunnel sections. Topographical mapping is on the JGD2000/ Japan Plane Rectangular Coordinate System VIII with its southwest corner located as the origin at 138°30'00"E, 36°00'00"N.

Actual thickness of overburden at each section is considerably different from average thickness. Therefore, both the first invariant of Cauchy stress tensor, I_1, and the second principal invariant of the stress deviator tensor, J_2, were calculated at a regular interval for each tunnel at actual depth below ground surface. The examined points included bot damaged and undamaged sections. Assuming that the coefficient of lateral pressure before the earthquake was unity as was suggested in Figure 5.3, the initial confining pressure at each point was set at its overburden pressure. Figure 5.13 shows distribution of $\sqrt{J_2}/I_1$ along the longitudinal axes of the selected tunnels and all the damaged sections are found against the highest values of $\sqrt{J_2}/I_1$. When the values of I_1 and $\sqrt{J_2}$ are plotted on a scatter diagram (Figure 5.14), it is noted that points for the damaged sections (solid circles in Figure 5.14) are clustered along the upper bound of the entire cluster of points. If the optimum boundary between the clusters of damaged and undamaged points is approximated by a straight line, the line would be considered as a failure criterion, which has the following expression:
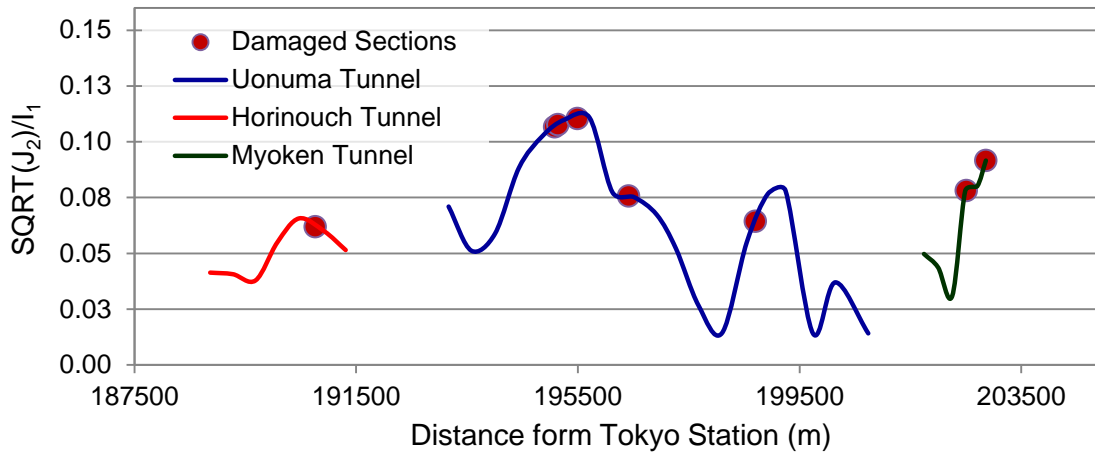
Figure 5.13: Distribution of the ratio of square root of second principal invariant of deviatoric stress tensor to first invariant of Cauchy stress tensor along the longitudinal axes of selected tunnels.
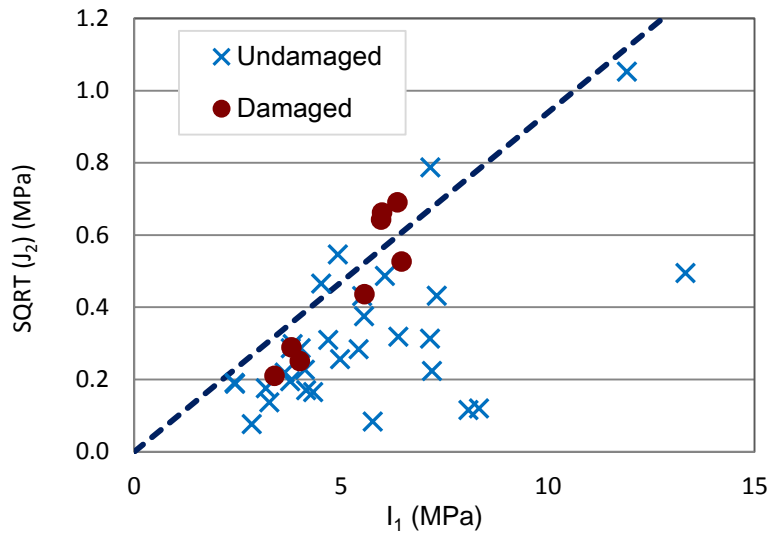
Figure 5.14: Scatter diagram of I_1 and $\sqrt{J_2}$ along selected tunnels to define failure criterion

$$\sqrt{J_2} = b \cdot I_1 + c \tag{5.33}$$

This truly resembles Drucker–Prager yield criterion. Now that we need to determine the optimum values of *b* and *c* in Equation (5.33), the following objective function is to be minimized in the least-squares sense.

$$f_{opt} = \left(\sum_{i_d=1}^{n_d} d_{i_d}^{\,2} + \sum_{i_u=1}^{n_u} d_{i_u}^{\,2} \right) \Big/ (n_d + n_u) \tag{5.34}$$

where, n_d and n_u are numbers of anomalistic points for damaged and undamaged sections below and above the criterion line (Equation (5.33)), respectively. d_i is the distance from each anomalistic point $i = \begin{pmatrix} I_{1_i} & \sqrt{J_{2_i}} \end{pmatrix}$ to the criterion line, which is given by:

$$d_i = \left| \sqrt{J_{2_i}} - bI_{1_i} - c \right| / \sqrt{1 + b^2} \tag{5.35}$$

It is less likely from Figure 5.14 that the criterion line for the sedimentary rocks over the examined stretch of tunnels would intercept $\sqrt{J_2}$ axis above $\sqrt{J_2} = 0$. Therefore, the optimum *b* value was obtained to be 0.0939 with *c* set at zero (broken line in Figure 5.14). The stress pattern shown in Figures 5.12 and 5.13 may have a way of repeating itself, and Equation (5.33) with *b* and *c* set at reasonable values may be used to examine the margin of safety of both existing and new tunnels for a given scenario earthquake in the target region. However, the small number of these samples may not guarantee the substantial accuracy of the obtained Drucker–Prager yield surface in the general statistical sense. The coefficient *b*, which physically describes the effect of internal friction angle, is very small perhaps reflecting the presences of weak and clay-rich discontinuities such as bedding planes, joints, shear zones and faults. These unexplained questions should be discussed as we gather much more reliable pieces of information.

5.4.2.1 Directions of Principal Stresses

From the state of stress at regular intervals along longitudinal axes of selected tunnels (Figure 5.13), directions of principal stresses are determined from direction cosines of eigen vectors of stress matrices. Figure 5.15 shows directions of major and minor principal stresses along selected tunnels. At most of the points, especially for seriously damaged part of Uonuma tunnel, the major principal stresses are compression and directed along longitudinal axes of the tunnels. The fault rupture planes for main shock and largest aftershock are oriented almost perpendicular to heavily damaged Uonuma tunnel. Slips along these rupture planes, having a pure dip slip pattern; have not reached the ground surface. Therefore, the top layer of earth's crust, in which tunnels are embedded, is compressed along longitudinal axis of Uonuma tunnel. As was observed from buckling and uplifting of roadbed for Uonuma tunnel (Figure 5.9), major failure mechanism was compressional stresses along longitudinal axis. Directions of major principal compressional stresses are consistent with the damage pattern.
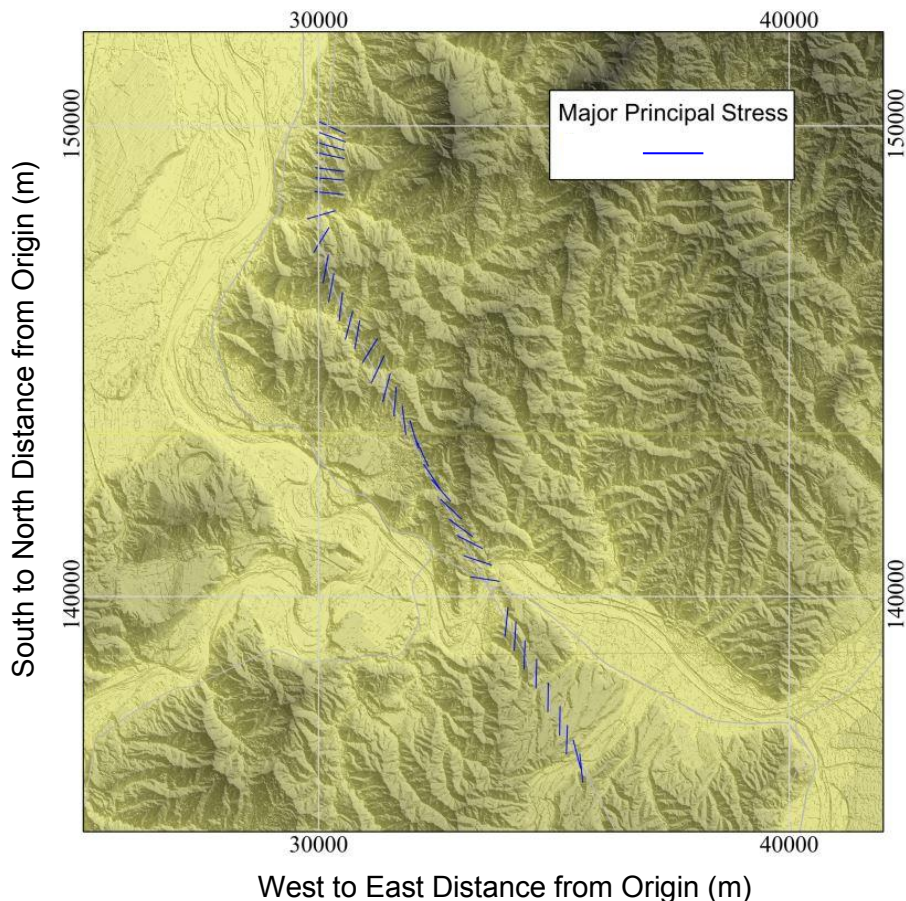
Figure 5.15 Directions of major principal stresses along the selected tunnels. The directions of principal stresses are consistent with the observed failure patterns. Topographical mapping is on the JGD2000/ Japan Plane Rectangular Coordinate System VIII with its southwest corner located as the origin at 138°30'00"E, 36°00'00"N.

5.5   ROLE IN TRIGGERING LANDSLIDE DISASTERS

Most of the moderate to large historical earthquakes triggered numerous landslides and slope failures which caused significant damages to seismically active areas. In addition to their direct impacts, landslides and slope failures cause long lasting geotechnical problems in the form of destabilized mountainous slopes due to rock weathering such as debris flows, temporal mass movements, etc. Some of the most catastrophic earthquakes in terms of landslide disasters in the last decades include the 1999 Chi-Chi Earthquake of Taiwan (10,000 landslides; Wang et al. 2003), the 1995 Hyogoken-nanbu Earthquake of Japan, the 1994 Northridge Earthquake in the USA (11,000 landslides; Harp and Jibson 1996), the 1989 Loma Prieta Earthquake in the USA (1,280 landslides; Keefer 2000), the 2004 Mid-Niigata Prefecture Earthquake in Japan (1,353; Sato et al. 2005a) and 2005 Kashmir

Earthquake of Pakistan (2,424 landslides; Sato et al., 2006). Quantitative and geospatial study of global losses caused by the most deadly earthquakes in last 40 years (Marano et al., 2010) has shown that deaths from landslides have been the largest among those from other causes than shakes. We, therefore, need to rationally understand the triggering mechanism and thorough cause investigation for such landslide disasters.

The second principal invariant of deviatoric stress tensor, J_2, can be considered as an index for rocks and soils deformability in the absence of reliable rock failure criterion and spatial coverage of soil/rock properties. Although the slip surfaces for different landslides will have large variability, seismic stresses are calculated at a representative depth of 5 meters below the ground surface to discuss the landslide triggering mechanism and its relation with the seismic stresses.

5.5.1   Application to Mid-Niigata Prefecture Earthquake

Figure 5.16(a) shows spatial distribution of the square root of the second principal invariant of deviatoric stress, $\sqrt{J_2}$, for the epicentral area of Mid-Niigata Prefecture Earthquake at 5 meters below the ground surface. Parallel belts of large $\sqrt{J_2}$ values are observed at an about 4km regular interval. All the landslides triggered by this earthquake are found concentrated along the stripes of large $\sqrt{J_2}$ values (white polygons in Figure 5.16(a)). This highlights the importance of the seismic stresses in triggering and/or reactivation of landslides. It is also noted that all the existing landslides that had been identified as of 2000 (National Research Institute for Earth Science and Disaster Prevention, 2000) are even more precisely clustered along the higher values of $\sqrt{J_2}$ (white polygons in Figure 5.16(b)). It can be deduced from the concordant behavior of higher $\sqrt{J_2}$ values and landslides existing before that earthquake that a similar pattern of stress distribution might have repeated in the past.

5.5.1.1 Concordance with Surface Geological Features

It is perhaps premature to discuss a universal model for explaining the 4km-long periodic structure. However when the contour lines of $\sqrt{J_2}$ are laid out on the subsurface geological map of the area (Seamless Digital Geological Map of Japan, Geological Survey of Japan), one can see that some major geological boundaries extend along the contour lines of $\sqrt{J_2}$ as shown in Figure 5.17.
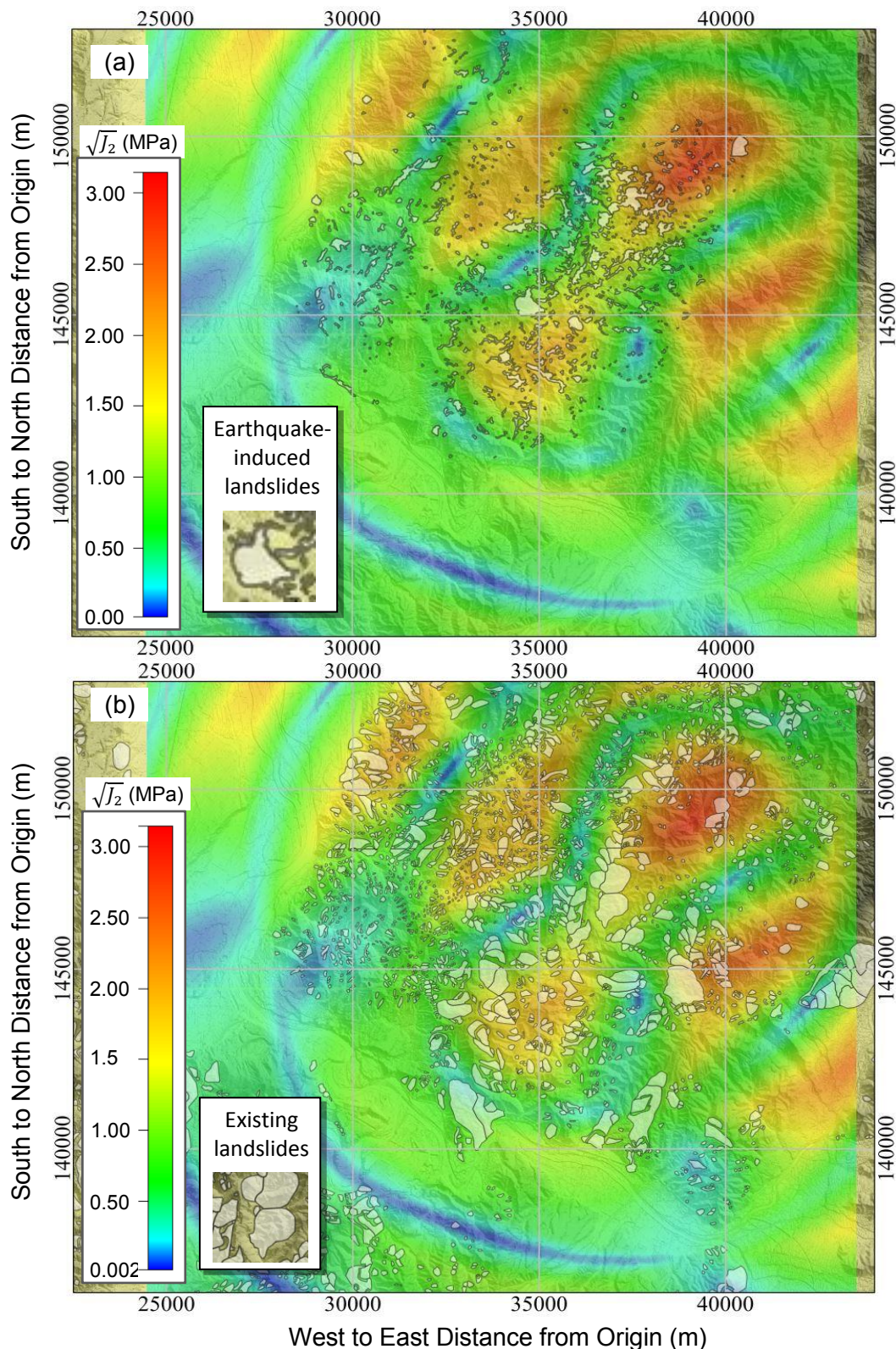
Figure 5.16 Distribution of second principal invariant of the stress deviator tensor $\sqrt{J_2}$ over the entire target zone at the depth of 5 meters from ground surface, with locations of (a) earthquake induced landslides (Oyagi et al., 2008) and (b) existing landslides (National Research Institute for Earth Science and Disaster Prevention, 2000,). Topographical mapping is on the JGD2000/ Japan Plane Rectangular Coordinate System VIII with its southwest corner located as the origin at 138°30'00"E, 36°00'00"N.

Considering that the area shows a geologically young folding structure, and anticlines tend to have their tops (hinges) removed by erosion, geological layer boundaries can be exposed as stripes. Therefore the 4km-long periodic pattern of the spatial $\sqrt{J_2}$ distribution overlapping in places with geological layer boundaries may be a reflection of the existing subsurface geological structure.
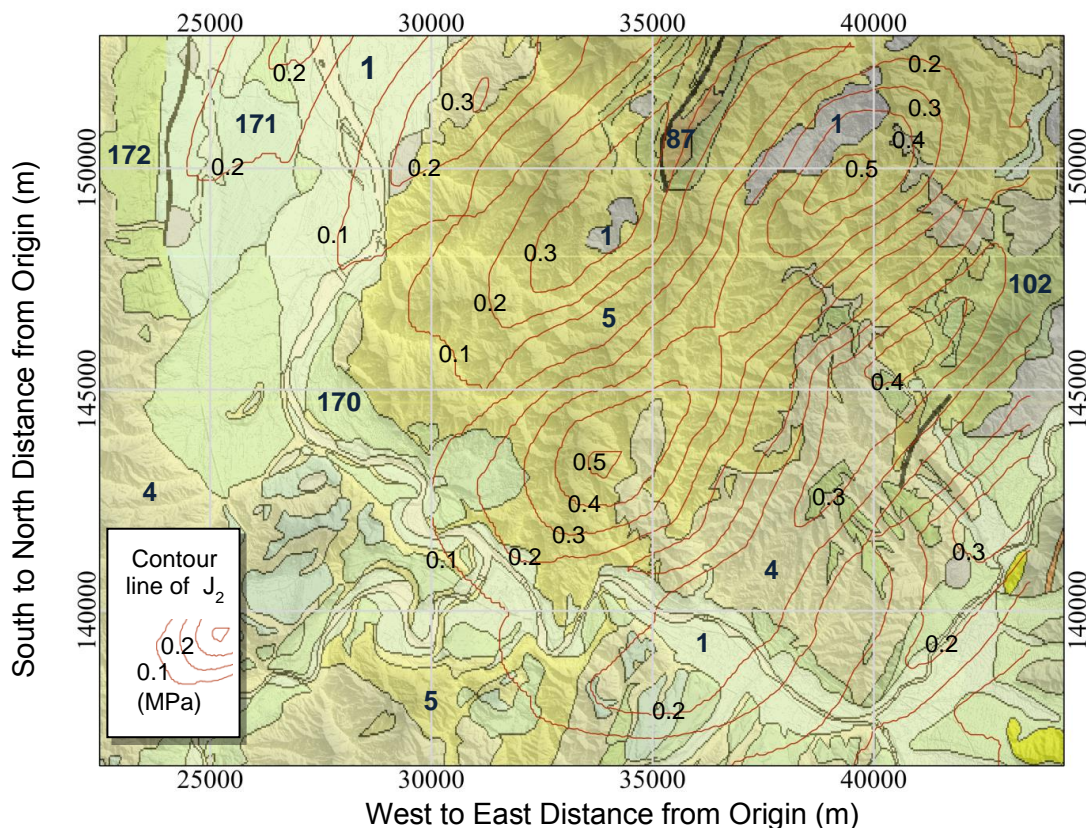
		1	Late Pleistocene to present, newest formation
		4	Early Pleistocene, sedimentary rocks
		5	Mid Miocene to Pleistocene, sedimentary rocks
		87	Mid Miocene to Pleistocene, volcanic products
		102	Late Miocene to Pleistocene, volcanic products
		170	Late Pleistocene, lower terrace deposit
		171	Late Pleistocene, middle terrace deposit
		172	Middle Pleistocene, upper terrace deposit

Figure 5.17: Distribution of second principal invariant of the stress deviator tensor $\sqrt{J_2}$ (-75 m) over the geological map (Seamless Digital Geological Map of Japan (1:200,000), Geological Survey of Japan) for the entire target zone. Topographical mapping is on the JGD2000/ Japan Plane Rectangular Coordinate System VIII with its southwest corner located as the origin at 138°30'00"E, 36°00'00"N.

5.5.2   Application to 2005 Kashmir Earthquake

2005 Kashmir Earthquake also triggered thousands of landslides and slope failures. Blind reverse separation of the causative Balakot-Bagh fault has crushed the mountain and a huge area of dolomite slopes is exposed to the extreme weather of the locality.

As like Mid-Niigata Prefecture Earthquake, Figure 5.18 shows the spatial distribution of $\sqrt{J_2}$ values for the whole epicentral area of 2005 Kashmir Earthquake at 5m depth below the ground surface. Higher values of $\sqrt{J_2}$ are aligned along the causative Balakot-Bagh fault and extend in a wider brush towards the hanging wall. It is also worth mentioning that almost all landslides triggered by the Kashmir earthquake (extracted by Sato et al. 2005 from the satellite data) are concordant with the higher values of $\sqrt{J_2}$ (black dots in Figure 5.18).
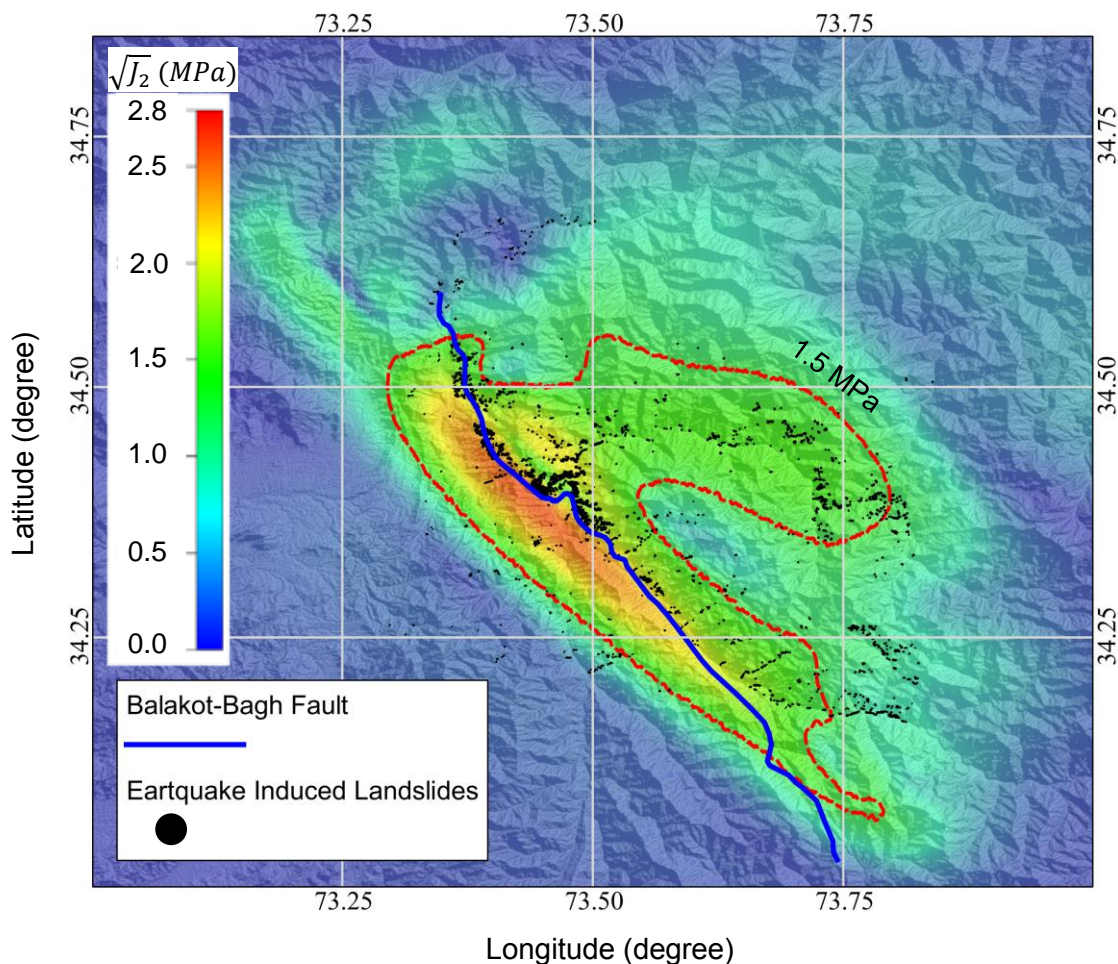
Figure 5.18: Distribution of the square root of the second invariant of deviatoric stress tensor at 5 meters depth below the ground surface along with the distribution of landslides triggered by the Kashmir Earthquake (black dots, mapped by Sato et al., 2007). All the landslides are found remarkably consistent with the large $\sqrt{J_2}$ values.

5.6   SUMMARY

This chapter presents the extension of source inversion results to obtain seismic stresses/strains in the interior of the layered half-space, representing this region in an ideal form, though forward modeling to rationally discuss effect of seismic stress changes in damaging underground structural facilities and triggering landslide disasters for the study areas of both Mid-Niigata Prefecture Earthquake and 2005 Kashmir Earthquake.

Mountain tunnels have been believed as one of the safest places during an earthquake because a mountain tunnel moves as one unit with its surrounding massive ground. However, recent near-field earthquakes accompanied by large soil deformations have been clouding this notion. One of the recent eye-openers was the damage, in the 2004 Mid-Niigata Prefecture Earthquake, to relatively deep railway tunnels of Juetsu new line of the Japanese bullet train network, skimming Higashiyama Mountains of Niigata Prefecture. Damage mechanism of these underground facilities needs to be investigated and dealt rationally for effective rehabilitation strategies and for examining the margin of safety of both existing and new tunnels in a given scenario earthquake.

Considering the average tunnel depth of about 75m for the target region, the spatial variation of square root of the second principal invariant of the stress deviator tensor, $\sqrt{J_2}$, was obtained for this depth as an indicator of the rock's vulnerability to failure, and several stripes of large $\sqrt{J_2}$ values, trending in NE-SW direction, appeared in parallel at a regular spatial interval of about 4 km. It is noted that not only damaged tunnel sections but also clusters of existing landslides were within these stripes.

Values of $\sqrt{J_2}$ as well as the first invariant of Cauchy stress tensor, I_1, were also determined at a regular interval along the entire stretch of the selected tunnels, taking into account actual depths of the chosen points. In this calculation, initial static stress conditions were assumed to be completely isotropic reflecting the data from a number of tunnel convergence monitoring records in sedimentary rocks. The scatter diagram of the obtained I_1 and $\sqrt{J_2}$ values showed that points for the damaged sections lined up along the upper bound of the entire cluster of points, suggesting the presence of a yield surface that follows the Drucker–Prager yield criterion.

Although the slip surfaces for different landslides will have large variability, seismic stresses are calculated at a representative depth of 5 meters below the ground surface to discuss the landslide triggering mechanism and its relation with the seismic stresses. Distribution of $\sqrt{J_2}$ values have shown a similar pattern of large NE-SW trending parallel stripes for Mid-Niigata Prefecture Earthquake while for the 2005 Kashmir Earthquake, the large $\sqrt{J_2}$

values are distributed in a wider brush along the causative Balakot-Bagh fault and to its Northeast. All the landslides triggered by both of the subject earthquakes were found along the large $\sqrt{J_2}$ values. It was also noted that all the landslides that existed before Mid-Niigata prefecture Earthquake are even more precisely clustered along the higher values of $\sqrt{J_2}$. It can be deduced from the concordant behavior of higher $\sqrt{J_2}$ values and landslides existing before that earthquake that a similar pattern of stress distribution might have repeated in the past.

If the spatial pattern of large $\sqrt{J_2}$ stripes trending diagonally in NE-SW direction has a way of repeating itself, the yield surface that emerged in the scatter diagram of I_1 and $\sqrt{J_2}$ values may be used to examine the margin of safety of both existing and new tunnels in a given scenario earthquake in the target region. However, exploring this possibility is to be made as we gather much more reliable pieces of information.

REFERENCES

1. Y. Okada (1985). Surface deformation due to shear and tensile faults in a half-space, Bulletin of the Seismological Society of America; 75: 1135–1154.
2. Y. Okada (1992). Internal deformation due to shear and tensile faults in a half-space, Bulletin of the Seismological Society of America; 82: 1018–1040.
3. R. Sato (1971). Crustal deformation due to a dislocation in a multi-layered medium, Journal of Physics of the Earth; 19: 31–46.
4. R. Sato and R. Matsuura (1973). Static deformation due to the fault spreading over several layers in a multi-layered medium. Part I: displacement. Journal of Physics of the Earth; 21: 227–249.
5. S. J. Singh (1971). Deformation of a multilayered half-space by stress dislocations and concentrated forces, Bulletin of the Seismological Society of America; 61: 1625–1637.
6. W. T. Thomson (1950). Transmission of elastic waves through a stratified solid medium, Journal of Appl. Phys. 21, 89-93.
7. N. A. Haskell (1953). The dispersion of surface waves on multilayered media, Bull. Seism. Soc. Am. 43, 17-34.
8. L. Knopoff (1964). A matrix method for elastic wave problems, Bull. Seism. Soc. Am. 54, 431--438.
9. J. W. Dunkin (1965). Computation of modal solutions in layered, elastic media at high frequencies, Bull Seism. Soc. Am. 55, 335-358.
10. R. Kind (1983). Improvements to layer matrix method, J. Geophys. 53,127-130.

11. F. Schwab, K. Nakanishi, M. Cuscito, G. F. Panza, G. Liang, and J. Frez (1984). Surface-wave computations and the synthesis of theoretical seismograms at high frequencies, Bull Seism. Soc. Am. 74, 1555-1578.

12. R. Wang (1999). A simple orthonormalization method for the stable and efficient computation of Green's functions, Bulletin of the Seismological Society of America; 89: 733–741.

13. R. Wang, F. L. Martin and F. Roth (2003). Computation of deformation induced by earthquakes in a multi-layered elastic crust, Computers and Geosciences; 29: 195-207

14. K. Aki and P. G. Richards (1980). Quantitative Seismology, W. H. Freeman, San Francisco; 932 pp.

15. B. L. N. Kennett and N. J. Kerry (1979). Seismic waves in a stratified half space, Geophys. J. R. Astr. Soc. 57, 557-583.

16. Y. Matsumoto and T. Nishioka (1991). Theoretical Tunnel Mechanics, University of Tokyo Press, Japan; 223 p.

17. K. Konagai, S. Takatsu, T. Kanai, T. Fujita, T. Ikeda, and J. Johansson (2009). Kizawa tunnel cracked on 23 October 2004 Mid-Niigata earthquake: An example of earthquake-induced damage to tunnels in active-folding zones, Soil Dynamics and Earthquake Engineering; 29(2): 394-403.

18. J. Johansson, and K. Konagai (2007). Fault induced permanent ground deformations: Experimental verification of wet and dry soil, numerical findings' relation to field observations of tunnel damage and implications for design, Soil Dynamics and Earthquake Engineering; 27: 938–956.

19. Y. Jiang, C. Wang, and X. Zhao (2010). Damage assessment of tunnels caused by the 2004 Mid Niigata Prefecture Earthquake using Hayashi's quantification theory type II, Nat Hazards; 53:425-441, DOI 10.1007/s11069-009-9441-9.

20. Commission report on the damaged railway tunnels in the 2004 Mid-Niigata-Prefecture Earthquake, East Japan Railway Company 2006; 279 pages.

21. Earthquakes Preliminary Observations on the Niigata Ken Chuetsu, Japan, Earthquake of October 23, 2004, Learning from Earthquakes, EERI Special Earthquake Report — January 2005.

22. T. Asakura (2001). Damage to mountain tunnels by earthquake and its mechanism, Modern tunneling science and technology; Proc. IS-Kyoto 2001.

23. General Construction Report of the Joetsu Shinkansen (from Omiya to Niigata), Japan Railway Construction Public Corporation 1984;3.

24. Digital Basic Map of Japan (Download site), Geospatial Information Authority of Japan (GSI), http://www.gsi.go.jp/kiban/index.html

25. Y. Yanagisawa, I. Kobayashi, K. Takeuchi, M. Takeishi, K. Chihara, H. Kato (1986). Geology of the Ojiya District, Quadrangle Series Scale 1:50,000, Niigata(7), No.50, Geological Survey of Japan.

26. N. Oyagi, S. Uchiyama, and T. Inokuchi (2008). Map of landslides caused by the 2004 Niigata-ken Chuetsu (Mid-Niigata) Earthquake (MJMA = 6.8), Technical Note No. 317, National Research Institute for Earth Science and Disaster Prevention.

27. Landslide distribution maps (shape files), National Research Institute for Earth Science and Disaster Prevention, October 2000, http://lsweb1.ess.bosai.go.jp/gis-data/index.html

28. W. N. Wang, H. L. Wu, H. Nakamura, S. C. Wu, S. Ouyang, and M. F. Yu (2003). "Mass movements caused by recent tectonic activity: the 1999 Chi-Chi earthquake in central Taiwan." *Island Arc*, 12(4), 325–334

29. E. L. Harp, R. W. Jibson (1996). "Landslides triggered by the 1994 Northridge, California earthquake." *Bull Seismol Soc Am* 86, 319–332.

30. D. V. Keefer (2000). "Statistical analysis of an earthquake-induced landslide distribution— the 1989 Loma Prieta, California event." *Eng Geol,* 58, 231–249.

31. H. P. Sato, T. Sekiguchi, R. Kojiroi, Y. Suzuki, M. Iida (2005a). "Overlaying landslides distribution on the earthquake source, geological and topographical data: the mid Niigata prefecture earthquake in 2004, Japan." *Landslides*, 2, 143–152.

32. H. P. Sato, H. Hasegawa, S. Fujiwara, M. Tobita, M. Koarai, H. Une,, and J. Iwahashi (2007). "Interpretation of landslide distribution triggered by the 2005 Northern Pakistan earthquake using SPOT 5 imagery", *Landslides,* 4, 113–122.

33. K. D. Marano, D. J. Wald, and T. I. Allen (2001). "Global earthquake casualties due to secondary effects: a quantitative analysis for improving rapid loss analyses." *Natural Hazards*, 52, 319-328.

34. Seamless Digital Geological Map of Japan (1:200,000), Geological Survey of Japan/ AIST, http://riodb02.ibase.aist.go.jp/db084/index_en.html

Chapter 6

6 Conclusions and Discussions

6.1 GENERAL DISCUSSION

The damages during an earthquake are caused by strong ground shaking as well as ground deformation. Strong ground shaking has long been considered the only cause of devastation, and this interpretation changed when deformability of the earth's crust and displacements around the fault surface were first examined. During an earthquake, stresses in the interior of the earth adjacent to the activated fault are redistributed leading to permanent deformations. Large deformations of soils and rocks often cause serious devastations to underground structures and trigger post-earthquake disasters in the form of landslides and debris flows, which can last long causing serious problems for rehabilitations and land conservations.

In this study, an improved model was proposed to extract precise Lagrangian ground displacements with shallow and deep parts of displacements distinguished more realistically. Precise ground displacement data was applied for earthquake source mechanism and seismic stresses/strains in the interior of earth's crust to develop scientific basis of failure mechanisms for effective rehabilitation works, disaster mitigation, land conservation and specifications/guidelines for new construction. Two most catastrophic earthquakes of the last decade, Mid-Niigata Prefecture Earthquake of 2004 and Kashmir Earthquake of 2005, were selected for verification and implication of the proposed study. Concluded discussion about typical damages during the aforementioned earthquakes, Lagrangian ground displacements and their implication for earthquake source mechanism and internal deformation of earth's crust, and their relation with devastations are presented in the following sections.

6.1.1 Damages during Study Earthquakes

The 2004 Mid-Niigata Prefecture Earthquake and 2005 Kashmir Earthquake are the two most catastrophic events of the last decade during which a variety of ground deformation induced deformations were observed. Both of them triggered thousands of the landslides

within their epicentral areas. In addition to their direct impacts, some very large sized soil masses blocked natural streams and posed secondary threats to their downstream reaches. In addition to the landslides, Mid-Niigata Prefecture Earthquake instigated very serious devastation to underground facilities. Damage to railway and road tunnels of many trunk lines skimming rugged mountainous terrain, damage to life lines and dislocation of the drainage wells are worth mentioning examples. Damage mechanisms of all these devastations needed to be thoroughly investigated for rational rehabilitation works and disaster mitigation.

6.1.2   Lagrangian Ground Displacements

Despite of the momentous development, remote sensing technology is still scarce to obtain history dependent Lagrangian ground displacements and in distinguishing deeper and shallower parts of crustal deformations. An improvement to a method was proposed to extract three dimensional Lagrangian ground displacements from available set of pre- and post-seismic digital elevation models (DEMs) with the underlying assumption that tectonic displacements vary smoothly in space. The method was also capable of filtering and tracing out shallow soil displacements (landslides, manmade changes etc.) from the total tectonic displacements.

Application of the proposed model to the actively folded epicentral area of Mid-Niigata Prefecture Earthquake yielded quite promising results. Although there was a long time interval between the pre- and post-seismic DEMs, filtered shallow ground displacements showed very good correlation with the landslides triggered by the earthquake. Lateral and vertical components of Lagrangian ground displacements have shown a strong cause and effect relation with earthquake induced devastation. Earthquake induced landslides were found concentrated in the area of large lateral displacements while crustal uplifting of the lower reaches of the natural rivers are considered responsible for flooding along their upper stream reaches. Lagrangian ground displacements have also shown a promising accuracy with the triangulation data and bench mark measurements within the study area.

In the recent times, InSAR interferograms are most commonly used to reveal earthquake induced ground deformations. Few advantages of obtained Lagrangian ground displacements over InSAR interferograms are summarized as;

✍ InSAR interferograms have relatively low spatial resolution. Fine resolution DEM gives more refined displacement pattern

✍ Although, when InSAR images are taken from different satellite flight directions, 3-D

displacement field of the terrain can be determined but it is still scarce in distinguishing the shallower ground displacements (landslides, manmade changes etc.) from the deeper crustal deformations.

✧ Noise due to the presence of non-surface objects (vegetation etc.) is another concern. For example for the Mid-Niigata Prefecture Earthquake, thick vegetation and thousands of landslides have made fringe patterns too complicated for extracting pure elevation changes from the available C-band (5.405 GHz) InSAR interferogram from RADSAT, a Canada's commercial SAR satellite. An attempt to remove non surface objects and filtering out shallow ground displacements could have minimized their effect on obtained Lagrangian displacements from DEM.

✧ However we cannot deny the power of InSAR. InSAR interferograms are quickly available for a wider area (usually the whole devastated area), often for larger part of the world. However, to obtain a required DEM we need special scanning and longer processing.

6.1.3   Source Mechanism and Internal Deformation of Earth's Crust

6.1.3.1 Source Mechanisms

With the available fine resolution ground displacement data, source mechanisms for the 2004 Mid-Niigata Prefecture Earthquake and 2005 Kashmir Earthquake were obtained by linear geodetic source inversion analysis in a laterally homogeneous stratified half-space. Inversion of Lagrangian ground displacements along with GPS and benchmark observations has successfully simulated the static image of fault slip distribution for a complex multi-segment fault model of the Mid-Niigata Prefecture Earthquake, where independent rupture planes were considered for the main shock and three largest aftershocks of magnitude larger than 6. Almost a pure dip slip pattern was revealed for all four rupture planes. The slip distribution pattern and magnitude with the maximum slip of 1.75m for the main shock was found close to the solutions obtained by the inversion of seismogram records, thus ensuring the acceptability of the method to estimate spatial rupture patterns of seismic faults for better rehabilitation tactics. Interference in distinguishing slips on different fault planes of a complex multi-segment fault would definitely exist, especially when the fault planes are close enough and overlapping. However, it is proven that the extent of interference was of practically acceptable level. Furthermore, a detailed and refined slip pattern cannot be obtained without availability of high resolution ground deformation data.

Static image of total fault slip distribution was also obtained for a 90km x 30km rupture

plane, in strike and dip directions respectively, for the 2005 Kashmir Earthquake. The earth structure was obtained by combining the sediment accumulation information to the borehole data. A reverse fault type has been revealed through the analysis which is in accordance with the pre-existing active faults. The largest asperity of fault slip has been observed at shallower depth around the extension of hypocenter and to its north, which could be a possible cause of very serious devastation in the near source region. At the same location, large crustal deformations have been detected by different authors. The maximum simulated value of fault slip was about 7.6 meters. The magnitude and pattern of fault slip at the surface extension of the fault plane was well consistent with three dimensional crustal deformations pattern both by magnitude and direction.

6.1.3.2 *Internal Deformation of Earth Crust and Earthquake Induced Damages*

Known fault slip distribution, as a discontinuity of seismic moment in a laterally homogeneous stratified half-space, was extend to solve two point boundary value problem for stresses and deformations at any desired point in the interior of earth's crust through forward modeling. The obtained stresses and deformations are evaluated at the locations of serious devastations to understand the role of seismic stresses in triggering earthquake induced disasters.

During the recent near-field earthquakes, serious damage to mountain tunnels is observed due to large soil deformations. One of the recent cases was the damages, in the 2004 Mid-Niigata Prefecture Earthquake, to relatively deep railway tunnels of Joetsu new line of the Japanese bullet train network, skimming Higashiyama Mountains of Niigata Prefecture. The second principal invariant of deviatoric stress tensor, J_2, was considered as work-a-round indicator of the rock's vulnerability to failure in the absence of reliable rock failure criterion and spatial coverage of soil/rock properties. Spatial variation of square root of the second principal invariant of the stress deviator tensor, $\sqrt{J_2}$, was obtained at an average as well as actual depth of selected tunnels below the ground surface. All the damaged tunnel sections were found against the highest values of square root of $\sqrt{J_2}$.

Values of $\sqrt{J_2}$ as well as the first invariant of Cauchy stress tensor, I_1, were also determined at a regular interval along the entire stretch of the selected tunnels, taking into account actual depths of the chosen points. In this calculation, initial static stress conditions were assumed to be completely isotropic reflecting the data from a number of tunnel convergence monitoring records in sedimentary rocks. The scatter diagram of the obtained I_1 and $\sqrt{J_2}$ values showed that points for the damaged sections lined up along the upper bound of the entire cluster of points, suggesting the presence of a yield surface that purely

resembles the Drucker–Prager yield criterion. For given limited number of observed points along selected tunnels, the material constants a and b of the yield line equation, $\sqrt{J_2} = aI_1 + b$, were determined as 0 and 0.0939, respectively.

Although the slip surfaces for different landslides will have large variability, seismic stresses were calculated at a representative depth of 5 meters below the ground surface to discuss the landslide triggering mechanism and its relation with the seismic stresses. Distribution of $\sqrt{J_2}$ values have shown a pattern of large NE-SW trending parallel stripes for Mid-Niigata Prefecture Earthquake while for the 2005 Kashmir Earthquake, the large $\sqrt{J_2}$ values were distributed in a wider brush along the causative Balakot-Bagh fault and to its Northeast. All the landslides triggered by both of the subject earthquakes were found concentrated within the areas of large $\sqrt{J_2}$ values.

It was also noted that all the landslides that existed before Mid-Niigata Prefecture Earthquake were even more precisely clustered along the higher values of $\sqrt{J_2}$. It can be deduced from the concordant behavior of large $\sqrt{J_2}$ values and landslides existing before the earthquake that a similar pattern of stress distribution might have repeated in the past. If the spatial pattern of large $\sqrt{J_2}$ stripes trending diagonally in NE-SW direction has a way of repeating itself, the yield surface that emerged in the scatter diagram of I_1 and $\sqrt{J_2}$ values may be used to examine the margin of safety of both existing and new tunnels in a given scenario earthquake in the target region.

6.2   PRACTICAL IMPLICATION OF THE STUDY FOR DISASTER MANAGEMENT

This study has more practical importance than educational. Large earthquakes are always catastrophic which directly and indirectly victimize the society in the form of loss of lives, properties, damage to infrastructures etc. An effort is made in this study to rationally understand earthquake induced damages, their scientific basis and to establish a cause and effect relation between the seismic activity and damaged pattern which can be helpful for rehabilitation, disaster management and preparedness for future seismic disasters.

This is a sequential study of computing earthquake induced Lagrangian ground displacements and their implications for earthquake source mechanism and subsurface seismic stress changes. Some of the key implications of the study for disaster management are presented in the following sections and Figure 6.1.
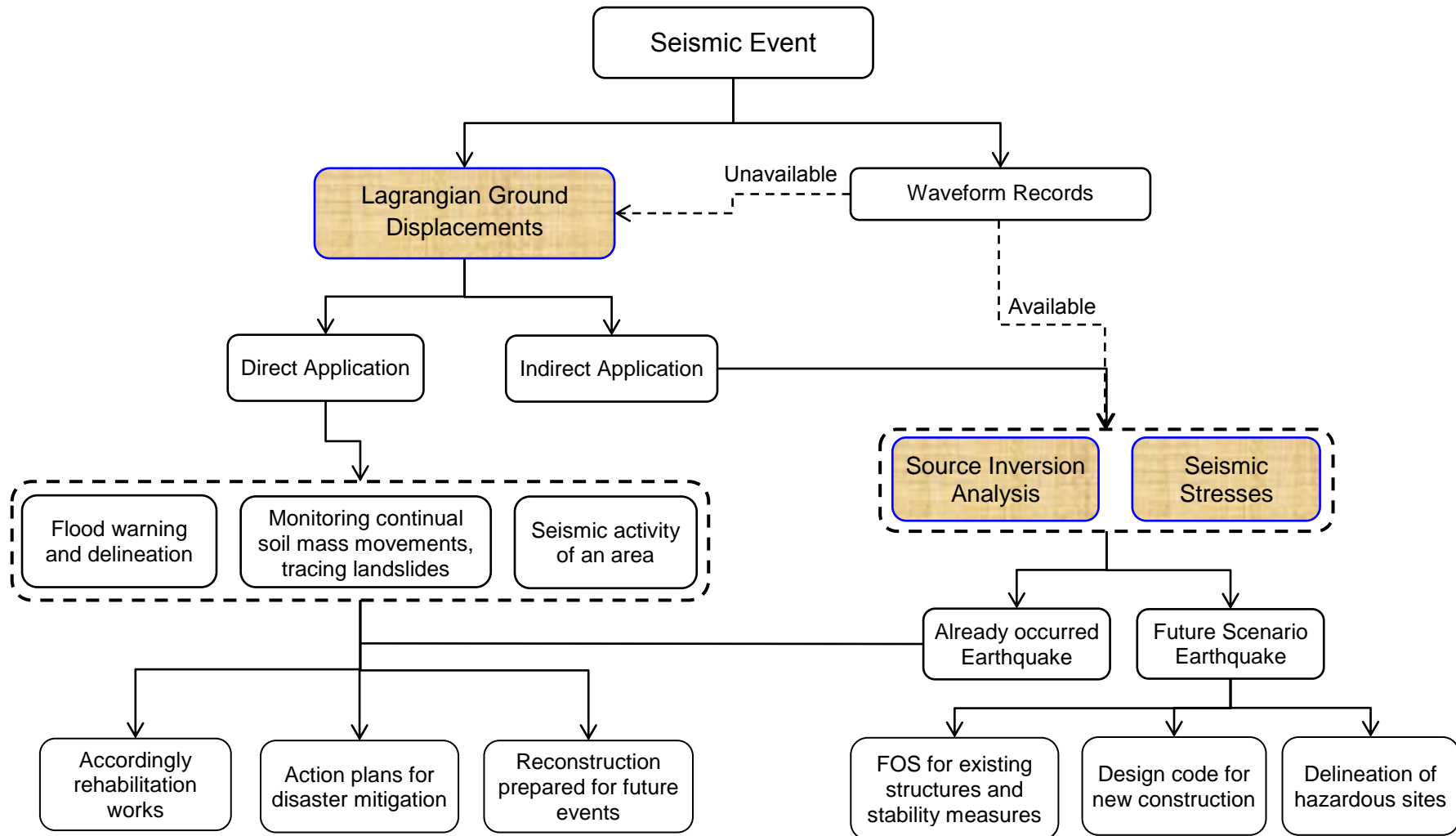
Figure 6.1: Flowchart showing implication of the study for effective disaster mitigation. Linkage, importance and implication of all three parts of the study (computation of Lagrangian ground displacements, source mechanism and seismic stresses) can also be seen by this chart.

6.2.1   Monitoring Continual Movement of Soil Masses

Stress accumulation and intense shaking during big earthquakes disturb soil/rock masses in the vicinity of activated seismic faults, where large scale mass movements such as landslides, rock falls and debris flows would occur.

The disturbed soil masses continue their movements due to water infiltration during rainy seasons and/or in the following seismic activities. By repeated laser scanning of such disturbed soil masses, unstable slopes, river dikes etc., their detailed and precise digital elevation models can be temporally saved. By computing Lagrangian displacements of such soil masses from digital elevation models would allow us to detect displacement rates and patterns, which can be used for warning to downstream facilities, delineation of areas to be affected and stabilization of disturbed masses.

Some massive landslides often block natural streams and rivers and create huge landslide dams, posing serious flooding threats to downstream areas in case of breaching. Water stored behind the landslide mass forces it way down by overflowing and/or seepage through the soil mass. The landslide mass changes its shape and deforms gradually by down cutting of overflowed water and washing out the fines by seepage water, which ultimately leads to the failure of soil mass. By knowing Lagrangian displacements of whole landslide dam body regularly, it is possible to predict/access failure of landslide dam and its pattern.

The author's research group has been evaluating stability of huge Hattain Bala landslide dam, created in 2005 Kashmir Earthquake, by monitoring GPS points marked on the dam body. However, discrete GPS points were not enough to understand behavior of whole landslide body. Knowing displacements of whole dam body can, therefore, more effectively and smartly help in evaluating its stability.

6.2.2   Flood Warnings and Delineation

By knowing the Lagrangian ground displacements, especially vertical component, along the lower reaches of natural channels, the conditions for their upstream reaches can be determined. For example for the study area of Chapter 3, vertical components of Lagrangian ground displacements have shown that the lower reach of Uono River was uplifted. Due to this crustal uplifting, the upstream reach was flooded during post-earthquake heavy rains. If we could have known these crustal deformations before heavy rains, the extent of flooded reach could have easily been determined. Necessary actions can be taken for mitigation strategies and delineation of potential hazardous areas

by knowing detailed ground displacements.

6.2.3   Seismic Stresses for Already Occurred Earthquakes and Rehabilitation

In chapter 5, changes in seismic stresses have been calculated in the interior of earth's crust, especially at the locations of damages to underground facilities. It has been observed that all the damages to underground railway tunnels were found at most heavily stressed locations. An attempt has also been made to obtain failure criteria for rocks and soils.

Knowing the threshold value of seismic stresses responsible for the damages, accordingly rehabilitation and reconstruction works can be carried out. Stabilization works for the surrounding ground and reconstruction capable of sustaining stresses/strains of the level induced by fault dislocations are important mitigation and preparedness steps for future seismic events of similar level.

It has also been found that all the landslides triggered by Mid-Niigata Prefecture Earthquake and 2005 Kashmir Earthquake were concentrated within heavily stressed zones. The landslides existing before Mid-Niigata Prefecture Earthquake were also concordant with the stress distribution pattern, proposing repetition of similar stress pattern in the past. Knowing potential landslide prone areas, necessary actions can be taken. For example delineation of hazardous areas, stabilization of landforms and protection works for important facilities and communication structures etc.

6.2.4   Seismic Stresses for Future Scenario Earthquakes

Although a precise definition of future scenario earthquake is not an easy job, it is no more impossible. Movement pattern for inter plate boundaries is definitely known and for intra-plate cases, mostly ruptures take place along previously mapped fault lines, consistent with existing folds and fault mechanisms. Although there are some developments in predicting earthquakes, fixing the magnitude of movement is still a challenge.

6.2.4.1 Guidelines for New Construction and FOS for Existing Structures

Knowing the level of seismic stress distribution in the interior of earth's crust for a given scenario earthquake, factor of safety for existing structures and there performance during the earthquake can be determined. Similarly, the design and construction codes can be revised so that all the new constructions should be capable of sustaining seismic stresses

induced by given scenario earthquake.

6.2.4.2 Landslide Hazard Delineation and Protection Measures

Seismic stress distribution near the ground surface for the given scenario earthquake will represents potential areas for landslide disasters (as proved in chapter 5). Necessary actions of landform stabilization, delineation of hazardous areas, protection of important facilities and communication structures can be taken as preparedness for the given scenario earthquake.

6.3   RECOMMENDATIONS FOR FUTURE EXTENSION OF THE WORK

Although a thorough objective based analysis rooted in updated scientific basis was carried out during this study, no study can be considered as absolutely perfect. Improvement of discrepancies and recommendation for future extensions of the work presented in this dissertation are summarized in the following sections.

6.3.1   Improvement and Refinement of DEMs

The DEM after earthquake used in the analysis for Lagrangian ground displacements (Chapter 3) was obtained by LiDAR scanning which cannot ensure elimination of non-surface objects. Although non-surface objects were tried to be filtered out in this study, the presence of filtered points other than shallow ground displacements suggests that non-surface objects might have not been completely eliminated. Further improvement and refinement can be made for the DEMs to obtain more precise picture of Lagrangian ground displacements.

6.3.2   Incorporation of Complex Terrain and Subsurface Profiles

Both for inverse and forward modeling to obtain source mechanism and seismic stresses in the interior of earth's crust (Chapter4 and 5), a laterally homogeneous stratified half-space with flat ground surface was considered, which is a simplification and idealization of the actual earth structure.

This work can be extended to incorporate undulation of surface terrain and variation of the earth structure to incorporate effect of topography and geological structure. Although it is possible theoretically, its practical application will be challenged by unavailability of spatial

coverage of subsurface information. However, with further development in the field of science and technology, presently missing and impossible things would become possible in future.

6.3.3   Effect of Tunnel Cavity in Seismic Stress Changes

Seismic stresses are calculated in Chapter 5 for laterally homogeneous stratified half-space without inclusion of cavities for tunnels. Considering overall dimensions of models (several tens of kilometers both in space and depth) and to discuss generalized stress pattern, cavities for tunnels are like a thread and can be ignored. However, with the objective of developing a relation between seismic stresses and damages to tunnels, inclusion of cavity can play a vital role for stress redistribution and concentration around the cavity. Many authors have developed theoretical solutions for redistribution of static stress around tunnel openings. Referring to Figure 6.2, Kirsch (1998) derived theoretical solution for radial, tangential and shear stress around the openings, located in uniformly stressed infinitely large medium as;
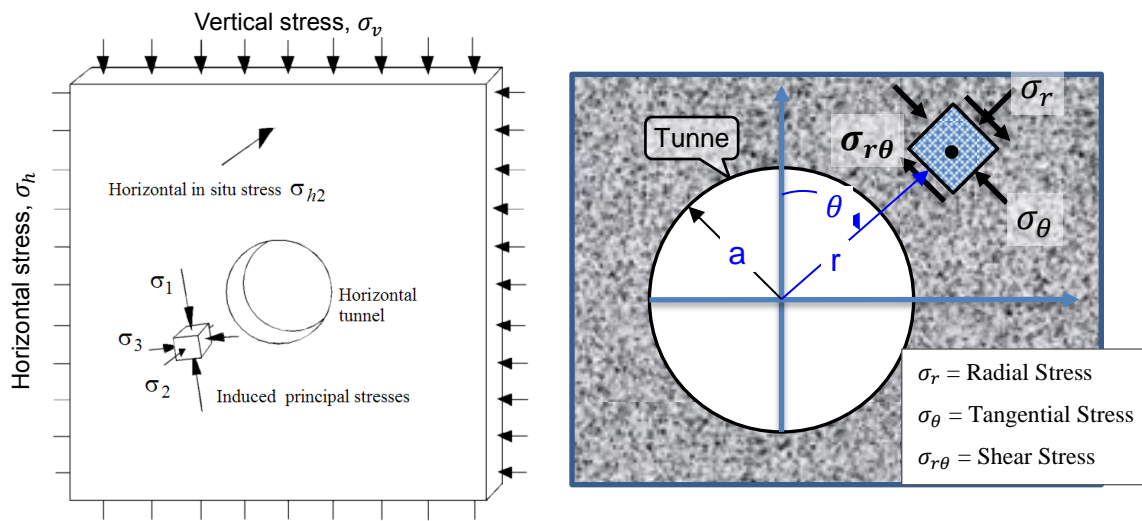
Figure 6.2: Schematic illustration of stress redistribution around a cavity after tunnel excavation

$$\sigma_r = \frac{\sigma}{2}\left[(1+k)\left(1 - \frac{a^2}{r^2}\right) + (1-k)\left(1 - 4\frac{a^2}{r^2} + 3\frac{a^4}{r^4}\right)\cos2\theta\right] \tag{6.1}$$

$$\sigma_\theta = \frac{\sigma}{2}\left[(1+k)\left(1 + \frac{a^2}{r^2}\right) - (1-k)\left(1 + 3\frac{a^4}{r^4}\right)\cos2\theta\right] \tag{6.2}$$

$$\sigma_{r\theta} = \frac{\sigma}{2}\left[-(1-k)\left(1 + 2\frac{a^2}{r^2} - 3\frac{a^4}{r^4}\right)\sin2\theta\right] \tag{6.3}$$

Where σ is the overburden pressure, k is coefficient of lateral pressure, a is radius of tunnel and r and θ are the radial and angular distances of target point, defined in Figure 6.2. An extension to this work is recommended to incorporate the effect of cavities for seismic stress changes, especially around the openings.

REFERENCES

1. G. Kirsch (1998). Die theorie der elastizitaet und die bedeurfnisse der festigkeitslehre, VDI Zeitschrift, 42, 797–807.

Appendix A

A.1   SOURCE FUNCTIONS FOR STRESS AND DISPLACEMENT

For a single point force (f_x, f_y, f_z) and point dislocation with moment tensor components (M_{xx}, $M_{xy} = M_{yx}$, $M_{xz} = M_{zx}$, M_{yy}, $M_{yz} = M_{zy}$, M_{zz}), Hankel transformed source functions for stress and displacement are given as,

Y_k^m	$J_m(kr)cos(m\theta)$			$J_m(kr)sin(m\theta)$	
m	0	1	2	1	2
ΔU_m	$-\dfrac{M_{zz}}{2\pi(\lambda+2\mu)}$	0	0	0	0
ΔV_m	0	$-\dfrac{M_{xz}}{2\pi\mu}$	0	$-\dfrac{M_{yz}}{2\pi\mu}$	0
ΔE_m	$\dfrac{f_z}{2\pi}$	0	0	0	0
ΔF_m	$\dfrac{(3\lambda+2\mu)M_{zz}}{2\pi(\lambda+2\mu)}k$	$\dfrac{f_x}{2\pi}$	$\dfrac{(M_{xx}-M_{yy})}{4\pi}k$	$\dfrac{f_y}{2\pi}$	$\dfrac{M_{xy}}{2\pi}k$
ΔW_m	0	$\dfrac{M_{yz}}{2\pi\mu}$	0	$-\dfrac{M_{xz}}{2\pi\mu}$	0
ΔG_m	0	$-\dfrac{f_y}{2\pi}$	$-\dfrac{M_{xy}}{2\pi}k$	$\dfrac{f_x}{2\pi}$	$\dfrac{(M_{xx}-M_{yy})}{4\pi}k$

For single point inflation, m = 0; for single force, m = 0,1; and for a double couple, m = 0,1,2 are considered. Where m is the degree of harmonics.

List of Figures

List of Tables